UNIVERSITY OF CALIFORNIA
RIVERSIDE

Topological Phases and Phenomena: A Case Study of Nodal Semimetals and 2D Materials

A Dissertation submitted in partial satisfaction
of the requirements for the degree of

Doctor of Philosophy

in

Physics

by

Michael Robert Phillips

December 2016

Dissertation Committee:

Dr. Vivek Aji, Chairperson
Dr. Shan-Wen Tsai
Dr. Roya Zandi

Copyright by
Michael Robert Phillips
2016

The Dissertation of Michael Robert Phillips is approved:

Committee Chairperson

University of California, Riverside

Acknowledgments

I am thoroughly grateful to my advisor, Dr. Vivek Aji, who has provided direction and an honest voice since day one. His questions and persistent encouragement helped me to grow as a student, teacher, and researcher. I am very fortunate to have worked alongside such a dedicated individual.

I am further grateful to my dissertation committee members, Dr. Shan-Wen Tsai and Dr. Roya Zandi, who pushed my knowledge as a student, fostered my growth as a teacher, and were always willing to write letters of reference. I also thank the additional members of my qualifying committee, Dr. Jing Shi and Dr. Gregory Beran, for giving context to my work and providing another lens through which to view it.

I will forever be indebted to my undergraduate education at the University of New Mexico which has proven rigorous and balanced, and has opened a long line of doors for me. In particular, I would like to mention my undergraduate advisor Dr. David Dunlap who offered cautious advice from the eyes of a theorist, and Dr. Douglas Fields who gave me experience in the laboratory and countless lessons in physics and in general. Also, I thank the University of California, Riverside for offering me a chance at graduate study with the Chancellor's Distinguished Fellowship, without which I would not have been able to pursue my degree.

Additionally, I would like to thank my fellow students who have supported my development in physics over the years. In undergraduate education at the University of New Mexico, the support and contrast offered by Bobby Sena, Anastasia Ierides, and Alexander Barron helped drive me to pursue and finish a double-major. My graduate studies, including

this work, have been influenced by discussions with many fellow students including Evan Sosenko, Jon Spalding, and Shima Imani.

The text of this dissertation is, in part, a reprint of an article from Physical Review B [1]. The co-author of the article, my advisor Dr. Vivek Aji, supported and directed the research which is represented there and in the rest of this dissertation. We acknowledge support from two travel grants from the Graduate Student Association which allowed for participation in March Meetings of the American Physical Society, as well as support from the National Science Foundation via grant NSF DMR-1506707.

To my family and friends for the endless support.

Abstract of the Dissertation

Topological Phases and Phenomena:
A Case Study of Nodal Semimetals and 2D Materials

by

Michael Robert Phillips

Doctor of Philosophy, Graduate Program in Physics
University of California, Riverside, December 2016
Dr. Vivek Aji, Chairperson

The explosion of recent work suggests that the next generation of solid state devices will be built upon an understanding of topological phases and phenomena. Key to the development and application of such devices are the notions of *tunability*, the manipulation of device properties with some external stimulus, and *interactions*, the additional influences on electrons.

Tunable devices form the basis for transistors and computer technology, but tunable topological devices have not been greatly explored. Thus, here we extend a previous proposal[2], which realized a two-node Weyl semimetal with a heterostructure of alternating topological/normal insulator layers and magnetic coupling in the direction perpendicular to the layers, with the coupling placed parallel to the layers. The magnetic coupling, arising, for example, from ferromagnetic insulators, here creates a line-node semimetal and it turns out to allow for tunable features in the device which can, in principle, be measured in future experimental studies. Interestingly, the Fermi surface can be tuned to have the topology of either a sphere or a torus, a unique aspect of line nodes.

Interactions in topological devices provide additional routes for further development. A good example is the problem of dilute magnetic impurities, providing a window into the structure of topological states. Here we use monolayer transition metal group-VI dichalcogenides for a simple model of topological bands in a semiconductor. The system is hexagonal but lacks an inversion center and includes strong spin-orbit coupling from the heavy transition metal, resulting in spin-split bands in separate valleys around the **K** points, with finite Berry curvature, and consequently a contrasted optical circular dichroism. The hole-doped regime possesses separate Fermi surfaces, with opposite spins on opposite sides of the Brillouin zone, producing an interesting spin structure in the Kondo ground state. Furthermore, the selective absorption of circularly polarized light according to valley/spin leads to the manipulation of the spin structure directly. We extensively study the Kondo ground state resulting from the quasi-equilibrium configuration inferred from the application of circularly polarized light, a situation which involves topology, spin-orbit interactions, hybridization with a magnetic impurity, and tunability of the spin state with light.

Contents

List of Figures **xi**

1 Introduction **1**
1.1 Topology in Condensed Matter . . . 2
1.2 Nodal Semimetals: Dirac, Weyl, and more . . . 3
1.2.1 Multilayer Construction of Nodal Semimetals . . . 4
1.3 Band Topology and Transition Metal Dichalcogenides . . . 6
1.4 The Kondo Effect . . . 9
1.4.1 History and Methodology . . . 10
1.4.2 Application to Monolayer Transition Metal Dichalcogenides . . . 12
1.5 Summary of Key Results . . . 13

2 Tunable Line Node Semimetals **15**
2.1 Introduction . . . 15
2.2 Model . . . 17
2.3 Closed Line-Node . . . 19
2.4 Open Line-Node . . . 27
2.5 Quantum Oscillations . . . 30
2.6 Experimental Outlook . . . 32
2.7 Conclusions . . . 34

3 Kondo Screening in p-Type Monolayer Transition Metal Dichalcogenides **36**
3.1 Introduction . . . 36
3.2 Model . . . 40
3.2.1 Low Energy Bands and Topology . . . 40
3.2.2 Hybridization . . . 41
3.2.3 Impurity at M Site . . . 44
3.3 Variational Wave Function . . . 45
3.3.1 Variational Parameters . . . 46
3.3.2 Spin and Susceptibiltiy . . . 47
3.3.3 Optically Excited Kondo State . . . 50
3.4 Numerical Renormalization Group . . . 53

3.4.1 Generic Setup . . . 54
3.4.2 Iterative Diagonalization . . . 58
3.4.3 Thermodynamics . . . 60
3.4.4 Spectral Function . . . 66
3.4.5 Numerical Results . . . 69
3.5 Comparison of Methods . . . 76
3.6 Conclusions . . . 78

4 Conclusions **80**
4.1 Diagnostics of Nodal Semimetals . . . 80
4.2 Kondo Effect in Exceptional Circumstances . . . 82
4.3 Future Directions . . . 83

A Berry Phase and Adiabatic Changes **85**
A.1 Adiabatic Changes in Quantum Mechanics . . . 86
A.1.1 Rigorous Setup . . . 86
A.1.2 Berry Phase . . . 88
A.2 Berry Connection and Curvature . . . 89
A.2.1 Definitions . . . 89
A.2.2 Alternate Forms . . . 90
A.2.3 Relation to Magnetism . . . 90
A.3 An Example: Particle in Slow-Varying B Field . . . 92

B Self-Consistent Born Approximation **94**
B.1 Potential Scattering . . . 95
B.2 Born and SCBA . . . 97

C Variational State and Spin **101**
C.1 State and Parameters . . . 101
C.2 Spin and Susceptibility . . . 104

D Details of NRG Projections & Convergence **108**
D.1 Logarithmic Discretization . . . 109
D.2 Tridiagonalization . . . 110
D.3 Convergence . . . 113

Bibliography **116**

List of Figures

1.1 A schematic diagram of the layered topological/normal insulator (TI/NI) heterostructure. The direction of magnetic coupling, here depicted in the normal insulating layers, leads to either a Weyl or line-node phase. 5
1.2 Top and side views of a monolayer TMD, MX_2. It appears like graphene viewed from above but it has some thickness, with each metal atom in a chalcogenide cage. 8

2.1 An example of the nodal curve for the closed region of parameters. The parameters chosen are $m = 0.9, \Delta_S = 0.6, \Delta_D = 0.4$ (with $d = v_F = 1$). . . 20
2.2 The dispersion surfaces $\pm\varepsilon_-(k_z, k_y)$, showing the nodal curve where the top and bottom surfaces touch along $\varepsilon_- = 0$. The parameter values are the same as for Fig. 2.1. 21
2.3 The variation of energy as a function of momentum perpendicular to the nodal line at four representative points is shown. Parameters remain as in Fig. 2.1. 22
2.4 The shape of the closed line-node in Fig. 2.1 is plotted as the field parameter m is changed, while keeping Δ_S and Δ_D fixed. The arrow shows the direction of increasing m. The closed curves have $m < \Delta_S + \Delta_D$ while the open curve violates this condition. 23
2.5 The volume enclosed by a surface of energy ε in momentum space, $N(\varepsilon)$, is plotted while varying the field parameter m. A perfect torus is obtained for a particular value of m. For smaller m, the torus gets squeezed, while for larger values the torus gets stretched (along the k_z-axis). 24
2.6 The slope of the linear (low-energy) density of states is plotted as a function of m. The points are obtained from numerical evaluation of the integral in Eq. (2.12). The black line is the analytical result from [25], while the dashed line shows the asymptotic value. 25
2.7 For large values of m, where the nodal line is open, the conductivity is roughly constant. Here we plot the conductivity divided by the asymptotic value as a function of m. These normalized curves are isotropic but the asymptotic values themselves are different for parallel and perpendicular directions with respect to the growth axis of the multilayer. 26

2.8 We plot $N(\varepsilon)$ for two different values of m. The left figure is for the case where we have a closed nodal line where the quadratic dependence is evident reflecting a linear density of states. For large m, for open line nodes, the quadratic dependence crosses over to a linear behavior very quickly as one departs from the node. This means that a linear DoS is trustworthy only for very low energies when $m \gg \Delta_S + \Delta_D$ (see Fig. 2.9). 27
2.9 Constant energy surfaces for the same parameters as in Fig. 2.6, but with $m = 1.15\text{eV} > \Delta_S + \Delta_D$, and a larger $m = 1.28\text{eV} \gg \Delta_S + \Delta_D$. As m increases the topology changes to disconnected surfaces. 29
2.10 Frequency for quantum oscillations for magnetic fields applied along the x-direction is plotted as a function of energy. The top curve shows the result corresponding to the maximal area, while the bottom corresponds to the minimal area. Dashed curves are obtained in the approximation of treating the surfaces as a circular torus. The parameters are the same as above with $m = 0.5\text{eV}$, taking $v_F = 10^4\text{m/s}$ and $d = 100\text{nm}$. 31
2.11 Fequency for magnetic fields applied along the z-direction as a function of the energy is plotted here. The solid curve shows the result corresponding to the only extremal orbit in this case. Note the orders of magnitude difference compared to Fig. 2.10 arising from the shape of the torus. 32
2.12 As m is varied, the density at which the jump in frequency occurs is modified. Here we plot the variation and note that it occurs for small densities when m is not too much larger than the difference $|\Delta_S - \Delta_D|$. 33

3.1 Low energy band structure of hole doped TMD. The unique aspect of the system is the spin split band allowing for spin nondegenrate Fermi surfaces around the K points. 38
3.2 Kondo energy scale for TMDs as a function of the inverse of the hybridization normalized to the spin splitting and density of states respectively, for the case where the chemical potential is halfway between the spin split valence bands. 48
3.3 The expectation value of J^2 is plotted as a function of the effective coupling that controls the Kondo scale (see Eq. (3.22)). 49
3.4 The difference in expectation values of J^2 from normal Fermi sea compared to excited case, plotted against the chemical potential shift in the selected valley, $\delta \equiv \delta_\nu$, compared to the spin splitting λ. The unexcited case is always greater so the difference shown is always positive. 52
3.5 Impurity occupation in the unexcited case, $\delta = 0$, for several choices of U at fixed Γ (see Sec. 3.4.5 for parameter details). The occupation is diminished or enhanced from 1 due to the asymmetry of the impurity level about the chemical potential. 61
3.6 Impurity entropy (top) measured in units of $k_B \ln 2$ and susceptibility (bottom) in units of $(g\mu_B)^2/k_B T$, in the unexcited case. The trends are typical (as in fig. 6 of Ref. [41]), except for the asymptotic value of susceptibility. 63
3.7 The Kondo temperature as given by Wilson's relation for the unexcited case of WSe_2 at a few U/Γ. The trend of increasing T_K at decreasing U/Γ is due to the proximity to the strong-coupling fixed point in parameter space. . . . 64

3.8 Impurity entropy (top) measured and susceptibility (bottom) for three monolayer TMD materials. They are all in the unexcited case, and with fixed $U/\Gamma = 9$. The trends are explained in the same way as for Fig. 3.6. 65
3.9 Impurity spectral functions for the unexcited case, with fixed $U/\Gamma \approx 4.9$. The spin up/down results overlap due to preserved time-reversal. They are consistent with conventional models[34], as expected from the metal-like structure of our model and choice of parameters. 68
3.10 Impurity entropy and susceptibility in the excited system for various offset δ. The numerical values are as described at the beginning of this section. The rightward evolution reveals increasing T_K. 71
3.11 The Kondo temperature in the excited case at a few δ. The increasing values away from $\delta = 0$ suggest effectively larger Γ with increasing magnitude of δ, pushing the starting point closer to the strong-coupling fixed point. 72
3.12 Impurity occupation (top) and spin (bottom). The nonzero offset polarizes the spin as expected. The occupation is increased with larger δ because one chemical potential becomes more distant from the impurity level. 73
3.13 The impurity spin at $T \approx 0$ shows some familiar dependence on δ. This result is equivalent to the shift in total spin $J_{z,val}$ from the variational calculation, revealing a sharp contrast between the results. 74
3.14 Impurity spectral functions for the excited model at $\delta/\lambda = 1/5$. The qualitative form is consistent with expectation, and is distinct from the variational result. The Friedel sum rule is satisfied within $\sim 20\%$. 75
3.15 The impurity spectral functions at various δ, for spin up (top) and down (bottom). The pattern of Fig. 3.14 is repeated as expected, with a reversal of roles as δ becomes negative. 76

B.1 The Green function with impurity scattering is represented as an infinite series involving the Green functions of the pure system and the self-energy. 96
B.2 A few of the simplest diagrams are shown from the exact self-energy due to impurity potentials. Dashes are interaction lines, crosses indicate impurity sites (each giving a factor of impurity concentration). 97
B.3 The series of diagrams for the Green function within the simple Born approximation. This is the same as Fig. B.1, but taking only the first piece on the r.h.s. of Fig. B.2. 98
B.4 The self-energy used within SCBA, in accord with Eq. (B.7), where the exact Green function is depicted by a double line. The second equality shows some terms resulting from the expansion of the internal Green function. 99

D.1 Energy levels relative to the ground state for even (top) and odd (bottom) chain lengths, for the unexcited system $\delta = 0$. The spectrum is certainly stable after going up to site $M = 30$. The subspace labels appearing in legends are $\{Q, J_z\}$. 114

D.2 Energy levels relative to the ground state for even (top) and odd (bottom) chain lengths, for the excited system $\delta > 0$. The spin values clearly split energy levels, giving this case much more structure. Interestingly, the system seems to stabilize more quickly, near site $M = 10$. 115

Chapter 1

Introduction

The discovery and importance of topological phases of matter has inspired a new school within condensed matter physics. The impact was made even more clear upon the announcement for the Nobel Prize in Physics of 2016, "for theoretical discoveries of topological phase transitions and topological phases of matter"[3]. Building upon those ideas, exploring the effects of interactions and the possibility of external device controls, is vital to the future development of technological devices. Exploring two prototypical systems, a layered heterostructure and a two-dimensional hexagonal crystal, we find a highly tunable topological phase complete with diagnostic properties accessible to experiments, and a remarkable spin-valley coupled system which forms a nonstandard Kondo state and whose spin structure can be manipulated with light.

In the following, we explain some of the background of topology in condensed matter physics, specifically the topics of nodal semimetals and topological bands corresponding to the specific cases studied here. This includes the specific construction of nodal semimet-

als studied in the first case (Chapter 2). Also we introduce a class of 2D materials and present some background to the Kondo effect, the result of placing a magnetic impurity in a metal and taking the temperature to zero, which provides context to the interactions and resultant phase appearing in the second case (Chapter 3). Lastly, we mention some of the key results.

1.1 Topology in Condensed Matter

The mathematical tools of topology had made their way into condensed matter physics by the 1970s, often in the discussion if defects[4], but it was really the famous "TKNN" paper of 1982 revealing the innate quantization of Hall conductivity[5] that sparked the explosion of deeper study. Further details[6] and the connection to adiabatic changes[7] were found within a few years after the TKNN work[1], with an explicit extension to Bloch states concluding the decade[8].

Over the past decades, many other advances have been made[9–19], showing that the trend of topology will be sticking around. Partly due to the relative youth of the topic, most of the work on topological phases and phenomena is focused on noninteracting systems (although they occasionally involve interaction-driven phases like superconductors). A mild exception is the spin Hall effect, which is now known to involve intrinsic topological sources as well as extrinsic contributions from scattering off classical magnetic impurities[20–22]. However, the interplay of topology and quantum interactions is not often explored and it is a topic that will be of great importance as topological devices continue development,

[1] See Appendix A for a generic derivation of the Berry phase from adiabatic changes.

motivating a significant part of the current work. The other common thread is a focus on tunable systems, where key properties of the topological phase can be manipulated with some external control.

1.2 Nodal Semimetals: Dirac, Weyl, and more

Among the outcomes of the study of topological materials are classifications of materials according to properties other than just band structure and symmetry. Important in the development has been the study of gapless systems, initially given serious consideration due to graphene, which are now known to exist in the surface states of topological insulators and elsewhere. The two-dimensional example of graphene provides a starting point, since it hosts massless Dirac fermions at low energies near the chemical potential; the degenerate spectrum is gapless at the $K(K')$ points leading to four-fold degeneracy at those points, the defining characteristics of a massless Dirac system.

Extending to three dimensions, one may consider preserving both inversion and time-reversal (TR) symmetry and obtaining some point where bands touch, but this procedure would require fine tuning some parameter at particular points in momentum space. On the other hand, breaking inversion or TR separates the points of contact and leads to one or more pairs of opposite-chirality Weyl nodes[2, 23–26]. The Weyl states are topologically equivalent to hedgehogs in momentum space, and they are protected against perturbations essentially because the dimensionality requires all three Pauli matrices in the minimal Hamiltonian. Candidates for Weyl semimetals, including one with 24 point nodes[26], have been proposed and examined for their interesting properties, such as chiral edge states and

a Hall conductivity which scales with the distance between the Weyl nodes[2].

In addition to point (Weyl) nodes, the breaking of a symmetry in the Dirac Hamiltonian can also lead to a "line-node" which is a curve in momentum space along which the bands touch. The line-node is not strictly as robust as Weyl nodes, meaning that they are insensitive to perturbations that satisfy particular symmetries, and the line-node can be displaced so that it's not at constant energy. Nevertheless, the line-node is still topologically robust in the sense that the bands will remain touching in the vicinity of the chemical potential despite the application of (many) perturbations. Interestingly, the structure of bands touching along a continuous curve is so exotic that, unlike familiar Dirac, Weyl, and Majorana particles, the elementary particles of the line-node have no counterparts in high energy physics and are thus unnamed.

1.2.1 Multilayer Construction of Nodal Semimetals

As remarked above, some candidates for Weyl semimetals have been proposed but they are often complicated, involving much more than the minimum of two Weyl nodes. However, by using the construction of 3D Dirac states from coupled 2D states and adding a magnetic coupling to break time-reversal symmetry, it was found that a Weyl semimetal may be obtained in the simplest possible outcome of two nodes[2]. The 2D states are provided by the surface states of topological insulators (TIs) which are protected linearly dispersing states[11, 13, 14], and they are separated by normal insulating layers (NIs) as in Fig. 1.1. These layers are not atomically thin but they are on the nanometer scale so states can tunnel between adjacent topological insulating surfaces, generally with different amplitudes for tunneling through the bulk of topological or normal insulators.

The TI/NI multilayer described so far leads to massive (gapped) Dirac states in 3D. To get Weyl nodes, a magnetic coupling parameter is introduced to break time-reversal symmetry. The origin of this parameter could be any magnetic coupling in the system, like ferromagnetic normal insulators or the introduction of magnetic impurities into either NI or TI layers. To get Weyl nodes, it is necessary to place this magnetic coupling along the direction orthogonal to the layers (along the growth direction); placing in the direction parallel to the layers leads to the line-node discussed above[25].

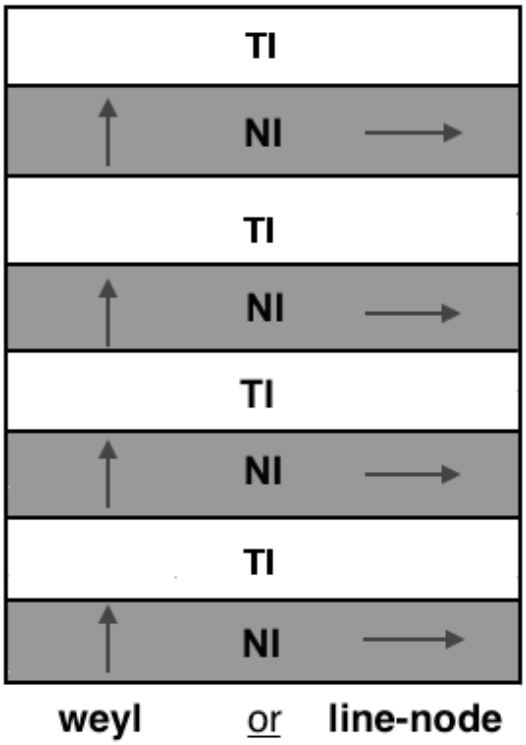


Figure 1.1: A schematic diagram of the layered topological/normal insulator (TI/NI) heterostructure. The direction of magnetic coupling, here depicted in the normal insulating layers, leads to either a Weyl or line-node phase.

In previous work, the Weyl phase was found to exist in a significant finite range

of magnetic coupling, meaning that there is no need for fine tuning that parameter to achieve the phase. The Weyl and line-node cases were investigated in some length, including basic transport calculations. The Weyl case is comparatively simple, possessing linear dispersions and lending itself to the Born approximation in the calculation of the effects of scattering off impurities. The line-node case on the other hand has a dispersion which is locally linear in the directions orthogonal to the curve and is thus more difficult to describe with a minimal Hamiltonian. Additionally, the slowly-vanishing density of states near the line-node makes the simple Born approximation unreliable and one must use the Self-Consistent Born Approximation (see Appendix B). Due in part to these complications, the previous work[25] obtained analytical results by approximating the dispersion and line-node as perfectly circular. In Chapter 2 of this work, we employ the layered TI/NI heterostructure model to investigate the line-node case more fully, in particular we avoid approximating the line-node as a circle and in fact we do not confine the case to closed curves, and the tunable properties of the phase are explored by examining the evolution of the Fermi surface as the magnetic parameter is varied.

1.3 Band Topology and Transition Metal Dichalcogenides

The appearance of topological properties in bands dates back at least to the famous work of TKNN[5], but the identification and clean derivation of quantities like Berry curvature and Berry phase appeared later[8]. By now, band topology is known to lead to several phases, importantly the topological insulators and Weyl semimetals discussed above. Topological bands often arise when a symmetry is broken, for example breaking inversion symmetry in

graphene leads to a gapped spectrum with Berry curvature and related effects[27].

Another option is to use a material similar to graphene but with broken symmetry coming from the crystal itself. This is realized in the single layer transition metal group-VI dichalcogendes (TMDs), an (almost) atomically thick hexagonal crystal lacking an inversion center but with preserved reflection and time-reversal symmetries (see Fig. 1.2). The formula for TMDs is MX_2, with transition metal M =Mo or W and chalcogenides X =S, Se, or Te. Because of the heavy transition metal, particularly for tungsten (W), the atomic spin-orbit coupling is very large, and the bands are greatly affected since the primary orbitals near the chemical potential all originate from the metal atoms and thus have d character[28–30]. In combination with broken inversion symmetry, spin-orbit coupling leads to a strong spin-splitting of the low-lying bands centered around the $K(K')$ points; the total splitting can be as large as 28% of the gap parameter as in WSe_2 or as small as 9% as in MoS_2. The topological properties like Berry curvature may be calculated, but are most easily seen by thinking about the Bloch sphere which describes the (pseudo-)spin state space of the band. In graphene, the Bloch angle is fixed at $\pi/2$ so only the equator is explored with the pseudo-spin forming either a chiral or a "hedgehog" pattern, either orthogonal or parallel to the 2D momentum vector. In TMDs, on the other hand, half of the Bloch sphere is explored by each band, with similar chiral or hedgehog patterns; this is indicative of some nontrivial topology.

The low energy band structure being focused around the corners of the Brillouin zone[2], giving "valleys" around the $K(K')$ points, alongside spin-splitting and preserved TR

[2]Note that MoS_2 is different, having a low-lying Γ point as well.

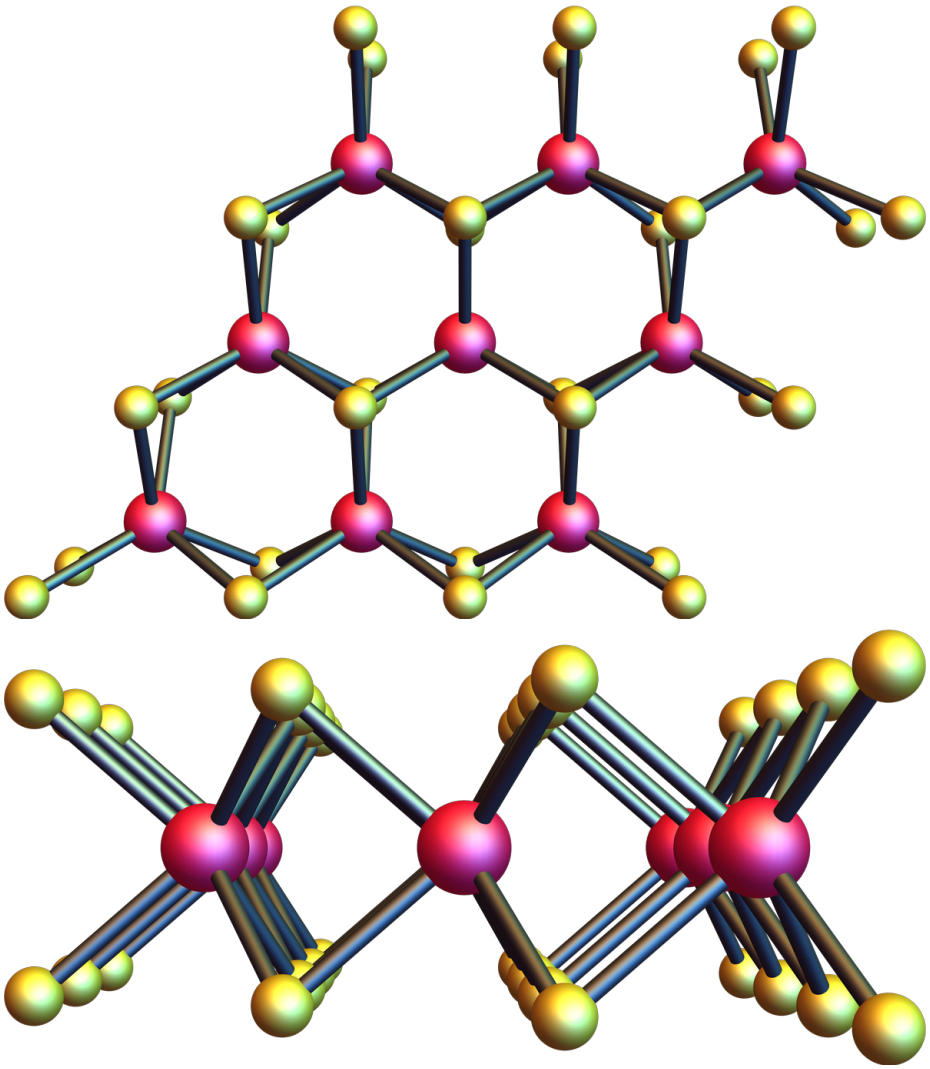


Figure 1.2: Top and side views of a monolayer TMD, MX_2. It appears like graphene viewed from above but it has some thickness, with each metal atom in a chalcogenide cage.

symmetry together give a structure with states at the same energy but opposite spin and on opposite sides of the Brillouin zone. This spin-valley locking built into the system is a particularly interesting point, particularly in the valence bands where the spin-splitting completely separates the spin up/down bands; the conduction bands are affected also but they are very closely spaced, like similar cups stacked one inside the other. In this work, we focus on the hole-doped regime where only the upper valence band crosses the chemical

potential, capitalizing on the spin-valley locking in the TMD system.

Another result of broken inversion symmetry is the selective absorption of circularly polarized light depending on the valley, termed "contrasted circular dichroism"[31]. Thanks to the presence of Berry curvature, and hence angular momentum, spin-preserving optical transitions are possible between the valence and conduction bands in TMDs despite the fact that all orbitals involved have d character, i.e. the same atomic angular momentum. By computing the optical transition probability directly for a particular circular polarization at an appropriate frequency, the absorption rate is seen to depend strongly on the valley and hence a particular spin may selectively be depleted from the valence bands. The optical probing and manipulation of a given spin/valley makes the system even more interesting, particularly when it is involved in an interacting state where spin is playing a crucial role — this is explored in Chapter 3.

1.4 The Kondo Effect

In correlated physics it is difficult to think of a more classic example than the Kondo problem, or the Kondo effect. In this section we give a very brief history and motivation of the problem, as well as an explanation of the effect and resolution of the problem. Alongside, we also present some basics concerning the methods that have been employed and developed to deal with it. Since we are most focused on an exceptional system, the monolayer TMDs described above, we also present some details having to do with the Kondo effect in that setting.

1.4.1 History and Methodology

The Kondo effect is the result of creating dilute alloys with magnetic metals, described most generally by the Anderson model of localized magnetic states[32]. In this model, the dilute limit is taken to an extreme with the inclusion of just a single magnetic impurity in a metal. A magnetic impurity is like any quantum impurity orbital, but with a strong Coulomb repulsion U acting when both spins occupy the orbital simultaneously. The coupling of the impurity to the band electrons V is due to the familiar Hartree-Fock exchange term. The Anderson Hamiltonian provides a good picture but the effective spin flips that result from exchange can be made more clear by projecting to the so-called Kondo Hamiltonian using the Schrieffer-Wolf transformation[33]. The result is an equivalent low-energy description which has the form of explicit coupling between two spins, with a scale $J \sim V^2/U$.

One can use perturbation theory to calculate various quantities to first order in J, such as resistivity, which give rather standard results, e.g. the resistivity will approach zero monotonically as the temperature decreases. However, experimental results revealed a minimum in the resistivity with a depth and location in temperature which scale with the concentration of magnetic impurities, suggesting that some increase in the resistivity at lower temperatures should be coming from the Anderson (or Kondo) Hamiltonian[34]. Investigating this deeper, Kondo took the perturbation further, to J^3, and indeed found a piece that explained the resistance minimum, but that piece was logarithmic in temperature and led to a singularity[35]. Perturbation theory can be carried out even further but the result just gives higher order logarithmic terms, thus revealing that the system is inherently non-perturbative in nature.

The "Kondo problem" is then given: how can one explain the resistance minimum and still go to temperatures lower than the so-called Kondo temperature? There was another problem as well: we have placed a magnetic state in a metal which can naturally lead to a local moment, but it is well-known that such moments cannot persist down to zero temperature — what happens to the moment in the Anderson (or Kondo) Hamiltonian? Attempts to answer these questions have come in many forms. Some have proposed a variational ground state, a many-body state with parameters which are varied such that the energy is minimized, which revealed that the magnetic impurity eventually forms a bound singlet state with the metal electrons[36, 37]. This method explains the "Kondo effect", the way that the moment disappears and also why the resistance would rise at low temperatures, and it gives a good energy scale for the problem (basically the Kondo temperature).

To get thermodynamic results, however, one must employ a method that gives more than just the ground state. To explain the formation of the singlet, the resistance trend, and every other property, a method was developed by Wilson in the 1970s called the Numerical Renormalization Group (NRG) [38], later refined and applied[39, 40]. Specific details of NRG and how it's used in this work are given in Sec. 3.4 (and Appendix D); here we give only a brief overview. Within NRG, one sets up a numerical procedure in a computer in which the system with the impurity is set up and diagonalized directly, with all subspaces of Fock space. Of course it is impossible to do this with the huge number of metal electrons, so one begins with effectively just one particle from the metal. The system of the impurity with this one particle is diagonalized numerically, with various matrix elements

(like impurity occupation and spin) being tracked and projected to the new eigenspace. To continue, a new metal particle is added to the Fock space, a new Hamiltonian matrix is built in the previously obtained eigenspace, and the diagonalization and tracking can be repeated. Eventually the space grows too large so the system is truncated, retaining only some number of lowest energy states (typically several hundred). Now, this procedure of extending the Fock space, diagonalizing, and truncating can be repeated as far as time and computer memory allow. With a diagonalized system, thermodynamics are easily obtained with traditional definitions, and it turns out that each extension of Fock space to include another particle also effectively lowers the temperature at which the thermodynamics are calculated. Thus one can obtain the spin, entropy, susceptibility, etc. for a finite temperature range approaching zero, and transport like resistivity may be obtained as well (although it is not calculated in this work), all in an inherently non-perturbative way. All of these results from NRG in the symmetric Anderson model agree very closely with other results in the appropriate limits: the entropy approaches zero as the temperature is lowered, indicating the formation of a spin singlet, and the susceptibility has a significant bump at moderate temperatures (for large repulsion U), indicating a local moment for some temperatures. Another useful quantity, the impurity spectral function, is calculable within NRG[41, 42], revealing deeper details about the structure of the impurity in the metal.

1.4.2 Application to Monolayer Transition Metal Dichalcogenides

The hybridization, or coupling, of the impurity with the band electrons is largely decided by the placement of the impurity on the lattice and the symmetry of the impurity and lattice orbitals. In the case of monolayer TMDs, as remarked above, the primary orbitals are

from the metal atoms and have d character; the low-energy basis involves d_{z^2}, and mixtures of $d_{x^2-y^2}$ and d_{xy}[29]. In two dimensions, a minimum requirement for the coupling to be nonzero is that the azimuthal symmetry of the impurity orbital must agree with that of the surrounding (nearest-neighbor) environment. For simplicity and to focus on the basic physics, the location chosen in this work is directly on top of a metal atom, i.e. the impurity is trying to share the site of a transition metal. As a result, given an impurity orbital, the coupling is nonzero only for the corresponding d orbital of the same symmetry. This strictly selective coupling to a particular orbital type is due to the location, but other high symmetry locations will have similar behavior.

In the Anderson model, the above considerations have little effect on the overall structure but the topological properties, the Bloch angles, enter when the lattice orbitals are projected to the band eigenspace. Thus, for doped systems like the one considered in Chapter 3 of this work, the model appears rather standard for an impurity in a metal, with the small catch that the hybridization will vary somewhat with the chemical potential. The real difference that is important here is the way that a single spin from each valley is crossing the chemical potential, making the impurity hybridize with a distinct spin structure. Also, the optical probing and manipulation of the TMD ground state discussed further above allow for the study of the Kondo effect in a very interesting quasi-equilibrium topological system.

1.5 Summary of Key Results

Given the background above, here we simply state some of the main findings of the work.

First, for the tunable line-node semimetal phase of Chapter 2, the main finding is the use of the magnetic coupling as a knob to manipulate the phase. The dispersion and conductivity are mapped as the node is tuned and even as it splits into open curves. Also, the Fermi surface is mapped and quantum oscillations are investigated for application and identification in experiment. In particular is a very interesting frequency-doubling when the Fermi surface closes, changing its topology from that of a torus to that of a sphere.

For the Kondo effect in doped TMDs in Chapter 3, both variational and NRG methods are used to assess the ground state. In true equilibrium, the energy and spin are addressed using the variational method with relative ease. In this case, the primary finding is that the spin state is not a many-body spin singlet, but rather an equal mixture of singlet and $m = 0$ triplet states. The outcome is nonmagnetic, but the triplet state implies some variance in spin. For the case of the TMD under application of light, we have a quasi-equilibrium case with effectively shifted chemical potentials in the two valleys, which due to spin-valley locking also gives a shift to the spins. Investigating this case rightly requires the use of NRG, the variational results giving an overreactive Fermi sea. The primary result is that the spin is in fact strongly polarized when the Fermi sea is shifted, the impurity giving a much larger contribution than the band electrons. To provide that evidence, the spectral function is constructed, showing the polarization explicitly.

Chapter 2

Tunable Line Node Semimetals

2.1 Introduction

The discovery of topological states of matter has brought a revolution in solid state physics. They provide impetus to develop new methodologies to find and characterize them, both theoretically and experimentally, and have opened new directions for technological innovation. Topological insulators in two and three dimensions which are gapped in the bulk and have surface states have already been realized. An important insight gained from these developments is the prominent role played by spin-orbit interaction in stabilizing such nontrivial phases[9–19]. A consequence of this line of investigation lead to the remarkable conjecture that some pyrochlore iridates, which possess all the necessary ingredients, such

This chapter consists of a reprinted article used with permission: M. Phillips and V. Aji, "Tunable line node semimetals", Physical Review B **90**, 115111 (2014), doi: https://dx.doi.org/10.1103/PhysRevB.90.115111. Copyright 2014 by the American Physical Society.

as large atomic number, localized moments and moderate correlation, are in a semimetallic phase where two nondegenerate bands touch at an even number of points in the Brillouin zone[26]. Moreover these nodes in the energy landscape are at the chemical potential and the low energy sector is described in terms of chiral massless electrons in three dimensions, which were first discovered by Hermann Weyl[43].

While pyrochlore iridates have yet to be unambiguously shown to house such a phase, a number of proposals have appeared in the literature that have the potential to do so. Balents and Burkov[2] showed that a heterostructure made up of alternating layers of magnetically doped topological insulator and normal insulator had Weyl fermions in its low energy sector. An alternate route is to find materials which have a Dirac dispersion in three dimensions and lift the spin degeneracy by breaking either time reversal or inversion. Angle resolved photoemission spectroscopy measurements on Na_3Bi and Cd_3As_2 have provided the first evidence for the existence of massless Dirac fermions[44–48]. The latter also breaks inversion and has the potential to be a Weyl semimetal, but the data lacks the resolution to verify the claim.

Here we focus on a variant of the heterostructure where a line is obtained instead of point nodes[25]. This requires the magnetization of either the magnetically doped topological insulator or that of the ferromagnetic insulator to be perpendicular rather than parallel to the symmetry axis of the device. The shape anisotropy of the device naturally favors such a geometry. Alternatively one can use an antiferromagnetic insulator with a suitable choice of terminating surfaces to provide the uniform exchange field needed. This construction has the advantage of the ability to tune the magnetization by varying tem-

perature. This provides a knob to manipulate the response of the device and access the interesting semimetallic phase. The main motivation of the study is that for line nodes the size, shape and density of states all depend on the magnetization. This is in contrast with the nodal semimetal where only the distance between the nodes depends on magnetization. The evolution of the low energy sector, as well as its consequence on thermodynamic and transport properties, as a function of magnetization is explored in this paper.

2.2 Model

As described by A. A. Burkov, M. D. Hook and Leon Balents[25], a simple way to construct a Weyl semimetal is to arrange alternating layers of topological insulator (TI) and normal insulator (NI). This setup leads to a Weyl semimetal dispersion containing the minimum of two nodes, provided time reversal symmetry is broken. To achieve this, the addition of magnetic impurities in each TI layer was proposed with magnetization along the z-direction – orthogonal to each layer, along the direction of growth. The two materials are set up such that each pair of layers (TI + NI) add up to a thickness d.

The full 2D Hamiltonian in terms of the momentum $\mathbf{k}_\perp = k_x\hat{\mathbf{x}} + k_y\hat{\mathbf{y}}$ describing this multilayered structure (using the notation and formalism in [25]) is

$$H = \sum_{\mathbf{k}_\perp, ij} c^\dagger_{\mathbf{k}_\perp i} c_{\mathbf{k}_\perp j} \left[v_F \tau^z (\hat{\mathbf{z}} \times \boldsymbol{\sigma}) \cdot \mathbf{k}_\perp \delta_{ij} + m\sigma^z \delta_{ij} + \Delta_S \tau^x \delta_{ij} + \frac{1}{2}\Delta_D (\tau^+ \delta_{j,i+1} + \tau^- \delta_{j,i-1}) \right]. \tag{2.1}$$

The first term describes the top and bottom states of a single TI layer (with $\hbar = 1$). The second term describes the spin splitting, resulting from magnetization in the z-direction. The remaining terms describe tunneling within an individual TI layer (the Δ_S term), and

between neighboring TI layers (the Δ_D terms). Without loss of generality one can set $\Delta_S, \Delta_D > 0$.

The eigenvalues for this Hamiltonian lead to the dispersion

$$\varepsilon_{\pm}^2 = v_F^2 \left|\kappa_\perp\right|^2 + (m \pm |\Delta(k_z)|)^2, \tag{2.2}$$

where $\Delta(k_z) = \Delta_S + \Delta_D e^{ik_z d}$ and $\kappa_\perp = k_y + ik_x$. There are a pair of non-degenerate nodes located at $k_x = k_y = 0, k_z = \frac{\pi}{d} \pm k_0$ where

$$k_0 = \frac{1}{d} \arccos\left[1 - \left(\frac{m^2 - (\Delta_S - \Delta_D)^2}{2\Delta_S \Delta_D}\right)\right]. \tag{2.3}$$

The nodes exist provided

$$(\Delta_S - \Delta_D)^2 < m^2 < (\Delta_S + \Delta_D)^2. \tag{2.4}$$

Such Weyl semimetals are expected to display a number of anomalous properties and house novel correlated phases. A variant of this setup is one where the axial symmetry is broken in addition to time reversal. The low energy sector is this case has line nodes and a system that is less studied.

Choosing the magnetization to be along the x-axis modifies the second term in Eq. (2.1). In practice this can be achieved by replacing the normal insulator with either ferromagnetic insulator, or antiferromagnetic insulator with appropriately chosen terminating surface. The Hamiltonian becomes

$$H = \sum_{\mathbf{k}_\perp, ij} c^\dagger_{\mathbf{k}_\perp i} c_{\mathbf{k}_\perp j} [v_F \tau^z (\hat{\mathbf{z}} \times \boldsymbol{\sigma}) \cdot \mathbf{k}_\perp \delta_{ij} + m\sigma^x \delta_{ij} + \Delta_S \tau^x \delta_{ij} + \frac{1}{2}\Delta_D(\tau^+ \delta_{j,i+1} + \tau^- \delta_{j,i-1})]. \tag{2.5}$$

The resulting dispersion is

$$\varepsilon_{\pm}^2 = v_F^2 k_x^2 + \left(m \pm \sqrt{v_F^2 k_y^2 + |\Delta(k_z)|^2}\right)^2 \tag{2.6}$$

which has an analogue condition to Eq. (2.4) for nodal behavior:

$$(\Delta_S - \Delta_D)^2 < m^2 - v_F^2 k_y^2 < (\Delta_S + \Delta_D)^2. \tag{2.7}$$

The new feature of such a geometry is that, instead of point nodes, this architecture supports line nodes. For our particular choice of magnetization, the zeros lie in the $k_z - k_y$ plane. The band for which this occurs is ε_-. The resulting surfaces $\pm\varepsilon_-(k_z, k_y)$ touch along a *curve*, called a "line-node", given by

$$v_F^2 k_y^2 + 2\Delta_S \Delta_D \cos(k_z d) = m^2 - \Delta_S^2 - \Delta_D^2. \tag{2.8}$$

The curve is always bounded in the k_y-direction,

$$m^2 - (\Delta_S + \Delta_D)^2 < v_F^2 k_y^2 < m^2 - (\Delta_S - \Delta_D)^2. \tag{2.9}$$

Since this relation potentially places a minimum on k_y, the curve is not necessarily closed. The upshot is that the variation of magnetization leads to an evolution of the nodal line from being closed within a Brillouin zone to being open. Thus the low energy sector of such an architecture is highly tunable. We explore the properties, such as density of states, conductivity and magneto-oscillations, in the rest of the paper.

2.3 Closed Line-Node

Let us first examine the parameter space $|\Delta_S - \Delta_D| < m < \Delta_S + \Delta_D$. A characteristic nodal line is shown in Fig. 2.1. To further examine the nature of the dispersion, we plot the energy as a function of $k_z - k_y$ for $k_x = 0$ in Fig. 2.2.

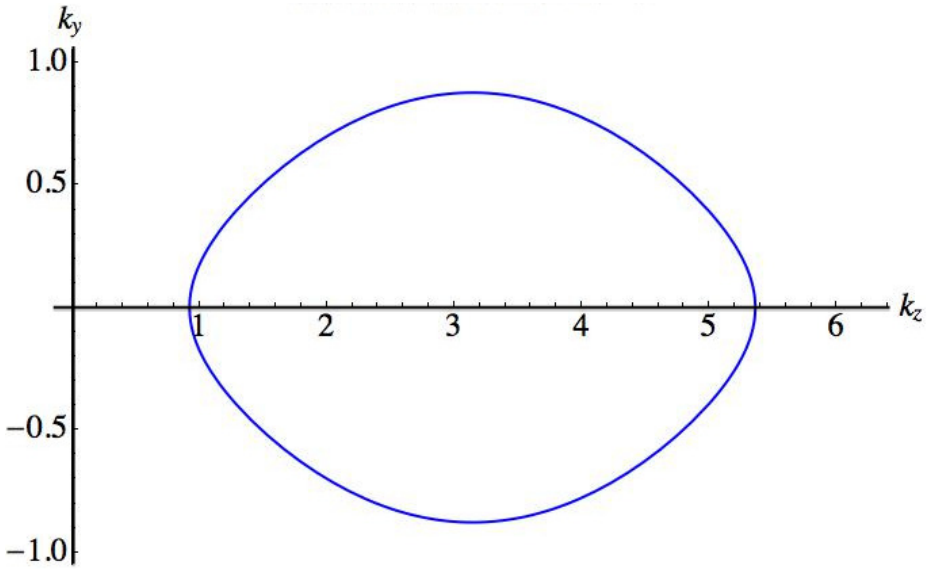


Figure 2.1: An example of the nodal curve for the closed region of parameters. The parameters chosen are $m = 0.9, \Delta_S = 0.6, \Delta_D = 0.4$ (with $d = v_F = 1$).

An interesting feature is that the dispersion is linear in momentum for deviations normal to the nodal curve. Parametrizing the curve as (k_z^0, k_y^0), which satisfy Eq. (2.8), the dispersion as a function of deviation normal to the curve is

$$\varepsilon_-^2 \approx v_F^2 \delta k_x^2 + \left(\frac{v_F k_y^0}{m \cos(\theta_0)} \right)^2 v_F^2 \delta k_\perp^2 \tag{2.10}$$

where $\tan(\theta_0) = \Delta_D \Delta_S d \sin(k_z^0 d)/v_f^2 k_y^0$.

The energy scale at which the deviation from linearity becomes substantial is also a function of where one is on the nodal curve. Thus an effective linear dispersion is valid only in an energy window which is the minimum of this function. To display this variation we plot the dispersion along various cuts across the nodal line in fig.2.3. We occasionally use $k_z' \equiv k_z - \frac{\pi}{d}$ as a convenient variable. The ratio of the velocities along the cuts for $k_y = 0$ and $k_z' = 0$ is

$$\frac{v_\perp(k_y = 0)}{v_\perp(k_z' = 0)} = \frac{md}{2v_F} \sqrt{\left(\frac{\Delta_S + \Delta_D}{m} \right)^2 - 1}\,. \tag{2.11}$$

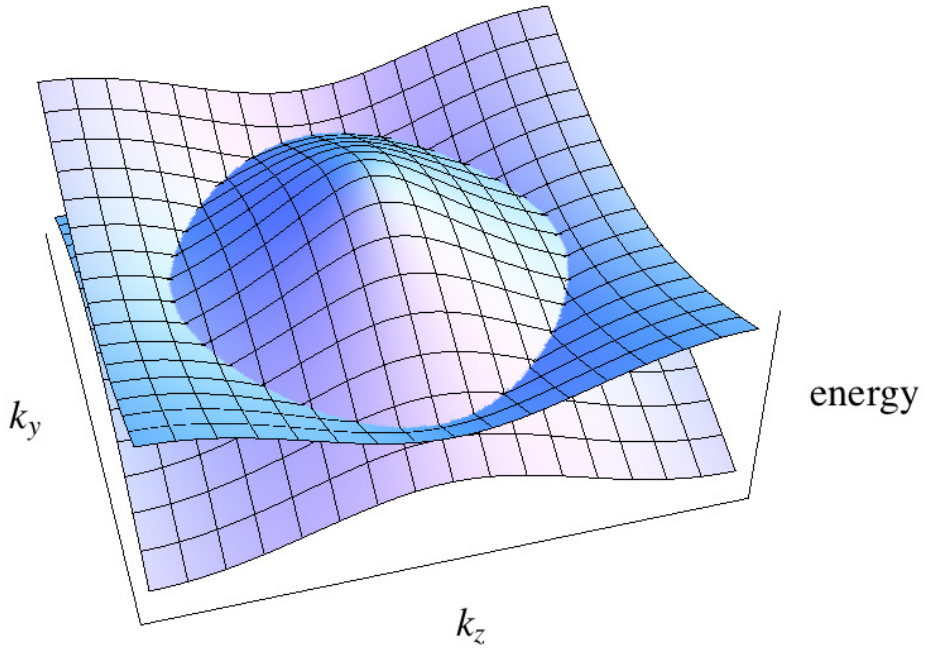


Figure 2.2: The dispersion surfaces $\pm\varepsilon_-(k_z, k_y)$, showing the nodal curve where the top and bottom surfaces touch along $\varepsilon_- = 0$. The parameter values are the same as for Fig. 2.1.

This is always less than one implying that the corrections to linearity are more pronounced along the growth axis of the heterostructure. Furthermore the monotonic increase of velocity from k_z to k_y axis implies that the density of states also varies along the node.

For a given device Δ_S and Δ_D are hard to tune but the magnetization can be modified. As a consequence the nodal structure evolves and as the magnetization is increased the curve extends out along k_z until it reaches the edge of the Brillouin zone. This is shown in Fig. 2.4. In general, analytic solutions are not possible. Under certain approximations the density of states and conductivity can be obtained in closed form. These are

1. The width of the nodal curve is "small" : $\cos(k_z d) \approx -1 + \frac{(k_z d - \pi)^2}{2}$.

2. The parameter m is "large" : $m \gg |\Delta_S - \Delta_D| \equiv \Delta \Rightarrow \Delta/m \approx 0$.

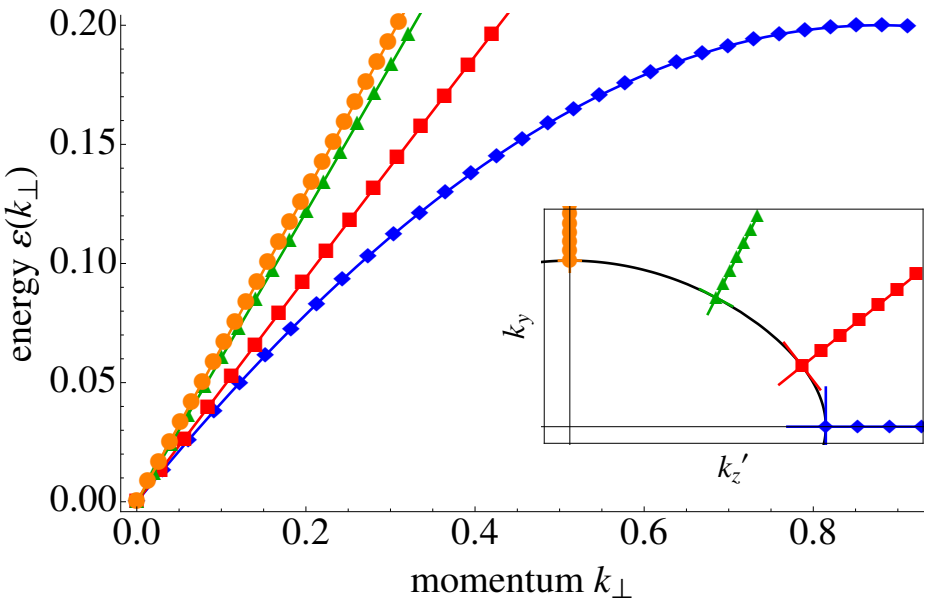


Figure 2.3: The variation of energy as a function of momentum perpendicular to the nodal line at four representative points is shown. Parameters remain as in Fig. 2.1.

Together, these greatly simplify the positive and negative dispersions that lead to the node, $\pm\varepsilon_-(\mathbf{k}) \equiv \pm\varepsilon(\mathbf{k})$ in Eq. (2.6). From here, the density of states is found by taking the derivative $g(\varepsilon) = \frac{d}{d\varepsilon}N(\varepsilon)$, where an integral must be done:

$$N(\varepsilon) = \int \frac{d^3k}{(2\pi)^3}\Theta[\varepsilon - \varepsilon(\mathbf{k})]. \tag{2.12}$$

With the above approximations, this integral becomes the volume of a torus in momentum-space with major radius m and minor radius ε, which can be calculated analytically to give a linear density of states (DoS): $g(\varepsilon) \propto \varepsilon$. The constant of proportionality (the slope of the DoS) comes out to be linear with respect to m. The resultant DC conductivity (using the Kubo formula, after the Self-Consistent Born Approximation[1]) is also linear in m[25].

[1]See Appendix B for details on this approximation.

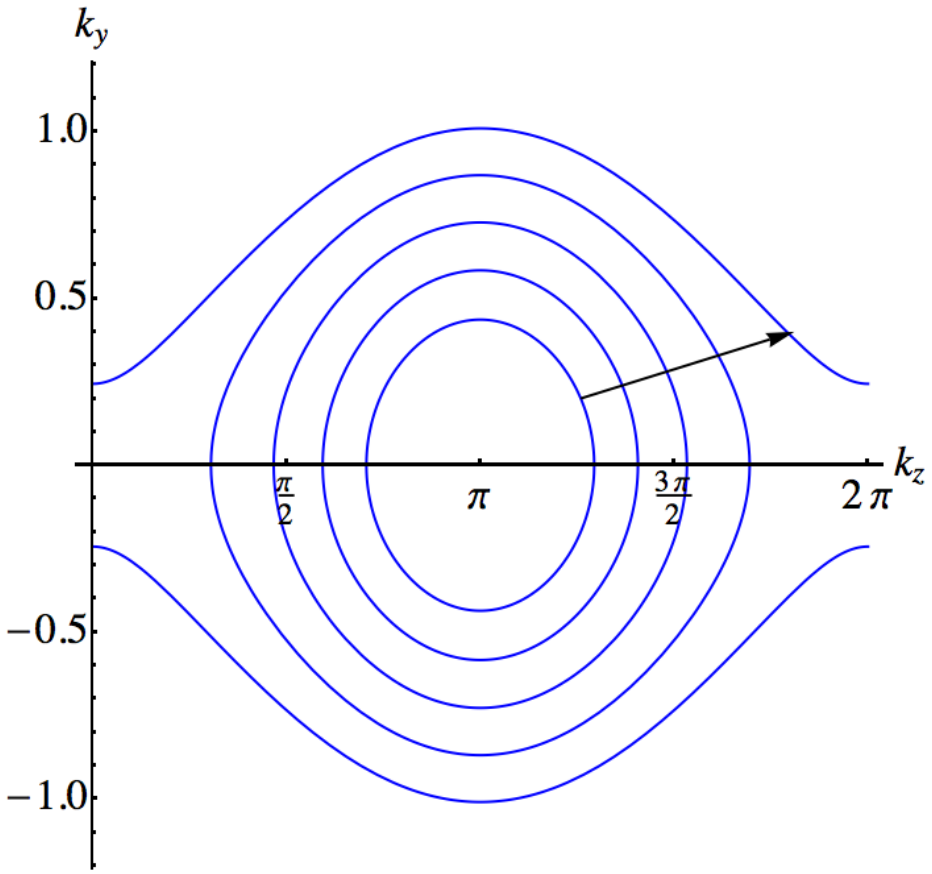


Figure 2.4: The shape of the closed line-node in Fig. 2.1 is plotted as the field parameter m is changed, while keeping Δ_S and Δ_D fixed. The arrow shows the direction of increasing m. The closed curves have $m < \Delta_S + \Delta_D$ while the open curve violates this condition.

The analytic expressions provide an interesting insight into the behavior of this device. The low temperature properties are all functions of the magnetization m. Thus tuning this parameter allows for the modification of transport and thermodynamic response. To get an accurate description numerical methods need to be employed as the approximations stated above are valid only for a finite intermediate window of m. As shown in Fig. 2.5, the equal energy surfaces have significant deviations from a uniform torus. Thus the DC conductivity will match the analytical expression for a finite range of magnetization.

To characterize the device better we employ numerical solutions for the full dis-

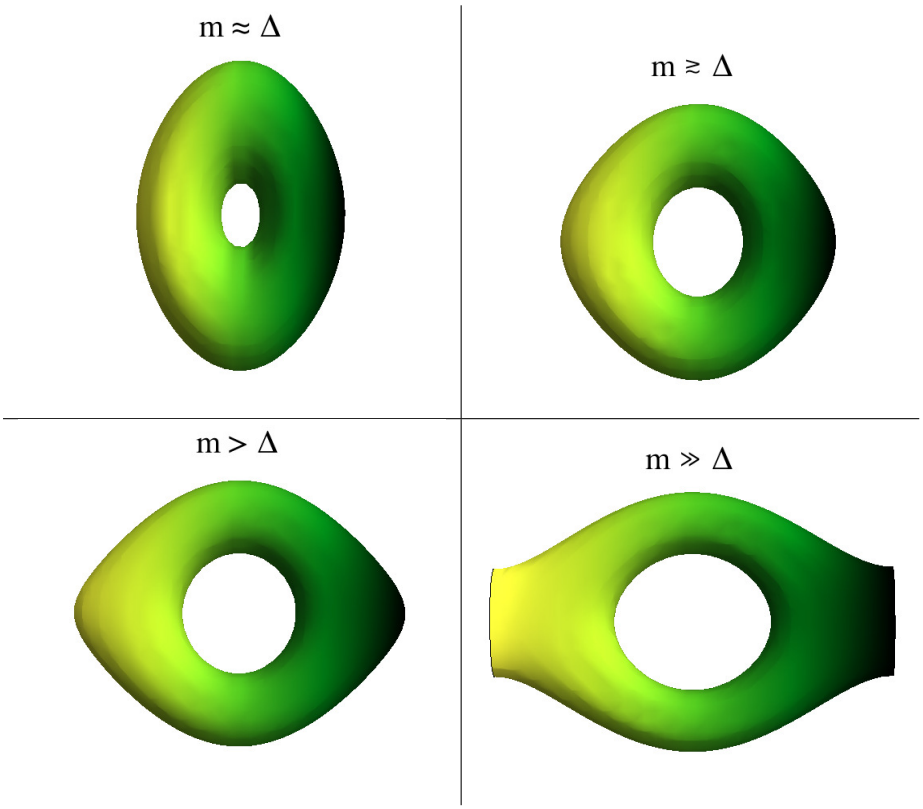


Figure 2.5: The volume enclosed by a surface of energy ε in momentum space, $N(\varepsilon)$, is plotted while varying the field parameter m. A perfect torus is obtained for a particular value of m. For smaller m, the torus gets squeezed, while for larger values the torus gets stretched (along the k_z-axis).

persion. Unless otherwise specified the parameters used are $\Delta_S = 0.6$eV and $\Delta_D = 0.4$eV. The results are qualitatively identical for different choices of parameters. We first compare the slope of the density of states near $\varepsilon = 0$ to that obtained analytically. This is shown in Fig. 2.6. A monotonically increasing slope is obtained as long as the nodal line remains closed. Once the nodal line hits the Brillouin zone boundary, the slope is roughly constant. We discuss the open node case in the next section.

For point-like impurities within the Self-Consistent Born approximation using Kubo formalism, the conductivity is proportional to the slope of the density of states.

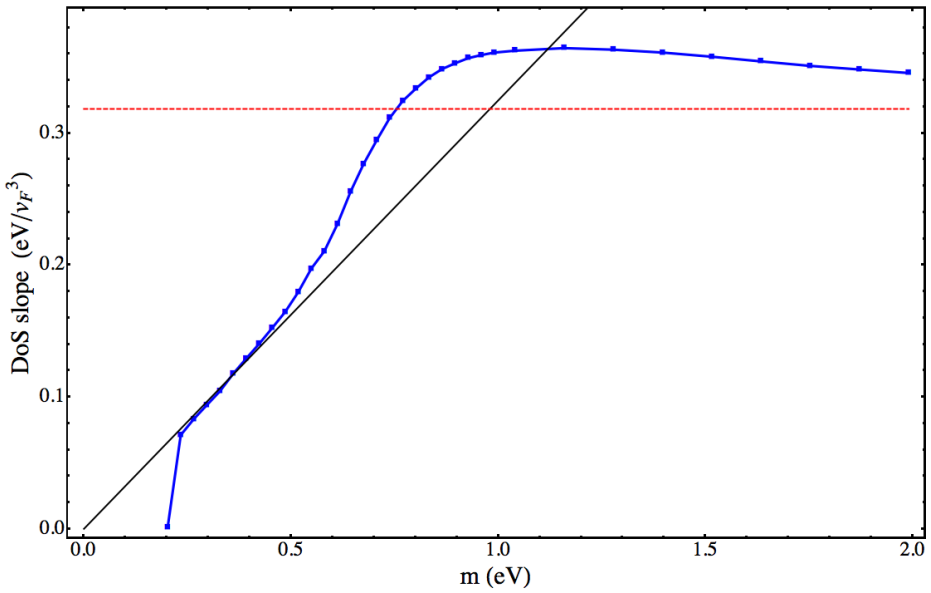


Figure 2.6: The slope of the linear (low-energy) density of states is plotted as a function of m. The points are obtained from numerical evaluation of the integral in Eq. (2.12). The black line is the analytical result from [25], while the dashed line shows the asymptotic value.

The linear DoS is found numerically over the entire range of m using Eq. (2.12), resulting in the conductivity shown in Fig. 2.7. For large values of m, the constant slope given by Eq. (2.17) leads to a conductivity that's also independent of m. This asymptotic value depends on the direction as there is an anisotropy in velocity parallel versus perpendicular to the growth axis of the device. To display the generic behavior we plot the ratio of the conductivity to the asymptotic value as a function of m.

The asymptotic values are obtained from the linear density of states with a constant slope (for details see the next section) and given by

$$\sigma_{\alpha\alpha} = \frac{2e^2}{h}\frac{v_{F,\alpha}^2}{\pi d v_F^2} \tag{2.13}$$

where $v_{F,x} = v_{F,y} = v_F$ and $v_{F,z} = d\sqrt{\Delta_S \Delta_D}$.

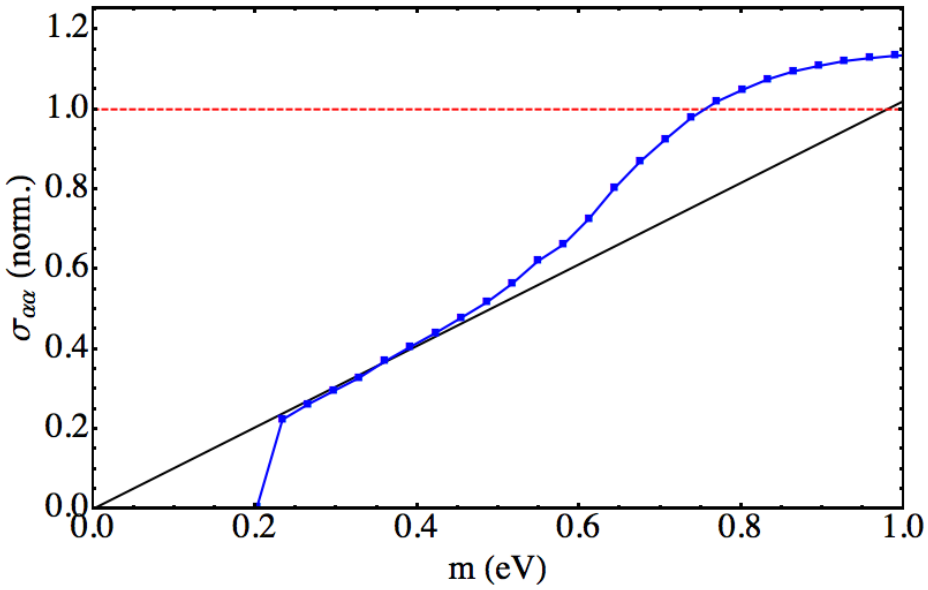


Figure 2.7: For large values of m, where the nodal line is open, the conductivity is roughly constant. Here we plot the conductivity divided by the asymptotic value as a function of m. These normalized curves are isotropic but the asymptotic values themselves are different for parallel and perpendicular directions with respect to the growth axis of the multilayer.

To better understand the nature of the density of states we also examine $N(\varepsilon)$ itself (see Eq. (2.12)) for various values of m. Its quadratic dependence of ε yields a linear density of states. As noted in the discussion of the dispersion and shown in Fig. 2.3, the deviation from linear dispersion occurs for small distances away from the node. The change in the dispersion is also evident in the evolution of $N(\varepsilon)$ plotted in Fig. 2.8. For small m a quadratic behavior is seen, but becomes linear as m is increased. The change in the density of states is reflected in the conductivity.

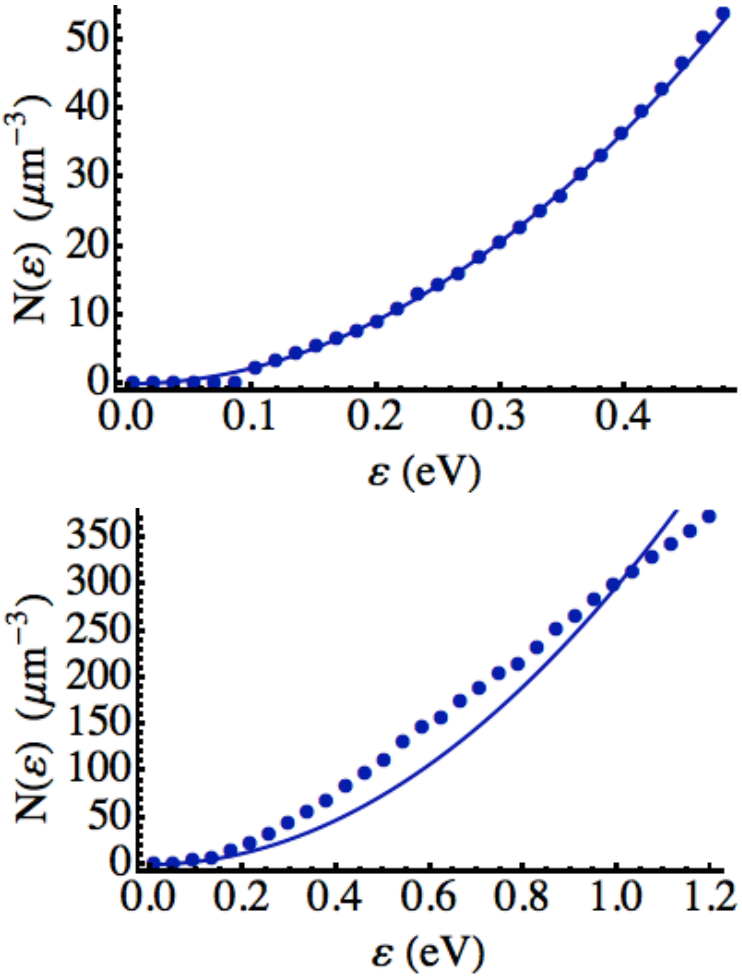


Figure 2.8: We plot $N(\varepsilon)$ for two different values of m. The left figure is for the case where we have a closed nodal line where the quadratic dependence is evident reflecting a linear density of states. For large m, for open line nodes, the quadratic dependence crosses over to a linear behavior very quickly as one departs from the node. This means that a linear DoS is trustworthy only for very low energies when $m \gg \Delta_S + \Delta_D$ (see Fig. 2.9).

2.4 Open Line-Node

We now turn to the regime of large m. This section examines the case $m > \Delta_S + \Delta_D$. For these values of m the node touches the sides of the first BZ along the k_z-axis. This implies that the analytic result, slope $\propto m$, of the previous section does not apply but the numerical techniques can be used. The density of states at low energies remains linear, but

its slope is constant as seen in Fig. 2.6. To evaluate the constant we use (2.10) and (2.8) assuming large m. Adding $2\Delta_S\Delta_D$ to both sides of Eq. (2.8) and with $m \gg |\Delta_S - \Delta_D|$, we drop $(\Delta_S - \Delta_D)^2$ from the right hand side of Eq. (2.8) to get

$$(v_F k_y^0)^2 + 2\Delta_S\Delta_D \left(1 + \cos(k_z^0 d)\right) \approx m^2 \tag{2.14}$$

where the notation k_α^0 refers to the points on the nodal line. The second term in Eq. (2.14) is bounded by the value of the cosine, and is small when $m^2 \gg 4\Delta_S\Delta_D$. Therefore $v_F k_y^0 \approx \pm m$. In other words, the open nodes evolve into straight lines stretching across the Brillouin zone at a fixed value of k_y. Similarly $\tan\theta_0 = \Delta_D\Delta_S d \sin(k_z^0 d)/v_f^2 k_y^0$ is bounded by the sine function and for $m \gg \Delta_S\Delta_D d/v_F$, $\theta_0 \ll 1$. Asymptotically Eq. (2.10) simplifies to

$$\varepsilon_-^2 \approx v_F^2 \delta k_x^2 + v_F^2 \delta k_y^2 \tag{2.15}$$

which, remarkably, is identical to the graphene dispersion. Setting $q = v_F\sqrt{\delta k_x^2 + \delta k_y^2}$, the DoS is

$$g(\varepsilon) = 2\int_0^{2\pi/d} \frac{dk_z}{2\pi} \int_0^{2\pi} \frac{d\phi}{2\pi} \int \frac{q dq}{2\pi v_F^2} \delta(\varepsilon - q) \tag{2.16}$$

$$= \frac{\varepsilon}{\pi d v_F^2}. \tag{2.17}$$

The resulting conductivity reflects this behavior and is nearly independent of m for $m >$ 1eV $= \Delta_S + \Delta_D$. The conductivity varies appreciably only when $|\Delta_S - \Delta_D| < m < \Delta_S + \Delta_D$. An interesting aspect of this device is its sensitivity to changes in magnetization. The change in conductivity from zero to the maximum value given in Eq. (2.13) occurs over the change

in exchange splitting of $2\Delta_S$ or $2\Delta_D$, whichever is smaller. This sensitivity is a generic feature of such nodal semimetals. A minimum time reversal breaking field is needed to close the gap and further increase leads to the nodal line spanning the Brillouin Zone. Over this energy window the conductivity changes from zero to the asymptotic value.

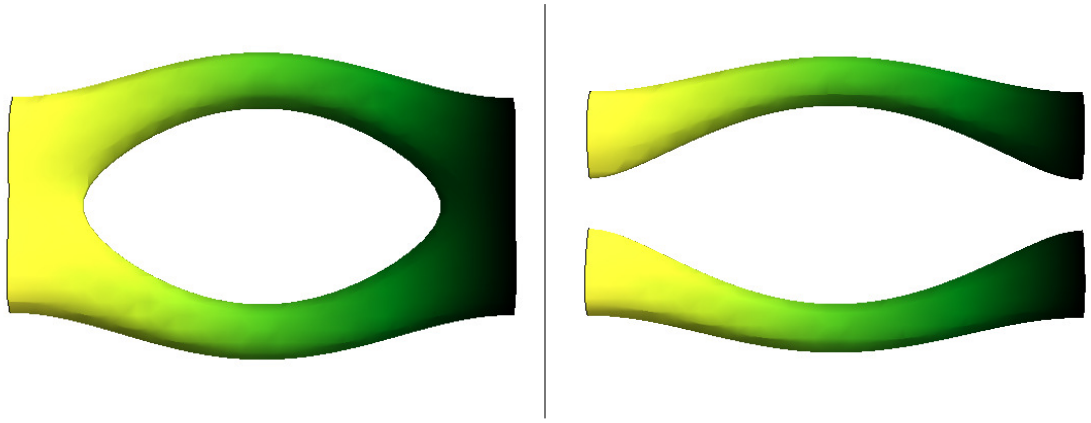


Figure 2.9: Constant energy surfaces for the same parameters as in Fig. 2.6, but with $m = 1.15\text{eV} > \Delta_S + \Delta_D$, and a larger $m = 1.28\text{eV} \gg \Delta_S + \Delta_D$. As m increases the topology changes to disconnected surfaces.

The evolution of the fermi surface as seen in Fig. 2.5 is measurable in magnetic oscillation experiments. Before we turn to the discussion of the expected behavior, it is worthwhile to note the shape of the equal energy surface for even larger m. In Fig. 2.9 we see that the the volume enclosed gets disconnected on increasing m. Thus the fermi surface of the doped system goes from a closed torus to two disconnected tubes, with an intermediate state where the outer surface of the torus is not closed within a Brillouin zone. Implications of these on quantum oscillations are discussed in the next section.

2.5 Quantum Oscillations

The evolution of the low energy sector as a function of the magnetization can be probed for systems with finite carrier density. For closed nodal lines the fermi surface has the topology of a torus, whose axis is parallel to the direction of magnetization. In the presence of an external magnetic field, the density of states is oscillatory. For large densities (i.e. Landau level index corresponding to Fermi energy is large), the oscillation is periodic in 1/B with a frequency proportional to the extremal area A_e of the fermi surface perpendicular to the applied field [49]:

$$f_{\frac{1}{B}} = \frac{\hbar c}{2\pi e} A_e(\varepsilon_F). \tag{2.18}$$

We consider two cases motivated by the geometry of equal energy surfaces. For magnetic field along the direction of the magnetization m (x-axis in our example), there are two frequencies at small magnetization while for large magnetization one of two contributing orbits changes from a closed to an open one. In Fig. 2.10 the two frequencies are plotted as a function of fermi energy. The fermi surface has the topology of a torus. For a field along the axis there are two extremal areas corresponding to the inner and outer circles. As the fermi energy increases the inner circle shrinks while the outer one grows. The smaller frequency vanishes when $\varepsilon_F = m - |\Delta_S - \Delta_D|$.

Alternatively, a field could be applied in the z-direction instead (i.e. along the growth direction). There is only one extremal orbit in this case. More precisely, there are two identical areas that contribute the same extremal area. As one increases the doping or carrier concentration, these areas grow approaching one another. At a critical value of

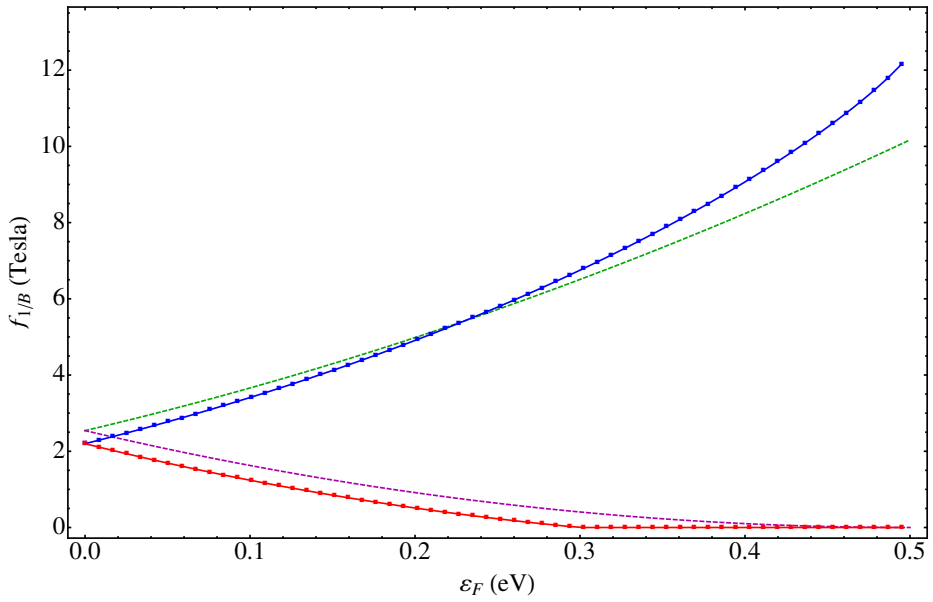


Figure 2.10: Frequency for quantum oscillations for magnetic fields applied along the x-direction is plotted as a function of energy. The top curve shows the result corresponding to the maximal area, while the bottom corresponds to the minimal area. Dashed curves are obtained in the approximation of treating the surfaces as a circular torus. The parameters are the same as above with $m = 0.5$eV, taking $v_F = 10^4$m/s and $d = 100$nm.

the fermi energy the two merge, and the resulting orbit continues to be extremal. Thus the frequency doubles at the critical value $\varepsilon_F = m - |\Delta_S - \Delta_D|$ (see Fig. 2.11).

This frequency-doubling is an interesting diagnostic of the line node. The experimental observation of the phenomenon depends on three conditions being satisfied: 1) the ability to tune the density of electronic carriers in the device; 2) the shape anisotropy of the magnetic insulator being sufficiently strong so as to allow for oscillations to be observed without reorientation of magnetization in the external magnetic field; and 3) the doubling occurs in the low energy regime of the device. While the first two are material challenges, the last can be addressed by looking at the energy at which the doubling occurs as a function of magnetization. From Fig. 2.12 it is clear that a parameter regime exists where the

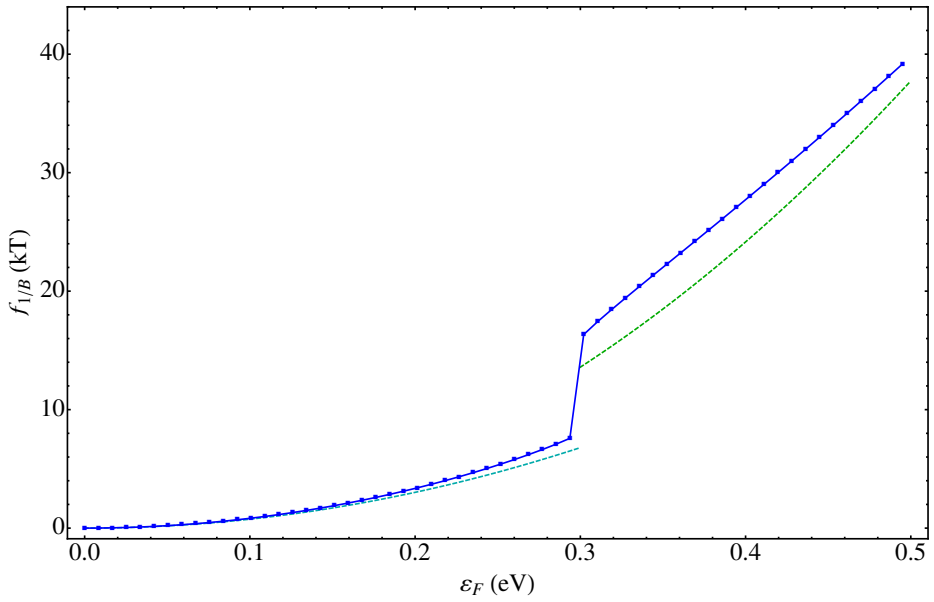


Figure 2.11: Fequency for magnetic fields applied along the z-direction as a function of the energy is plotted here. The solid curve shows the result corresponding to the only extremal orbit in this case. Note the orders of magnitude difference compared to Fig. 2.10 arising from the shape of the torus.

critical energy is small, i.e. less then an eV.

2.6 Experimental Outlook

Over the last few years remarkable progress has been made in realizing various elements required for the multilayer device. Given the wealth of novel phenomena expected with symmetry-broken surface states [14, 50–52], detailed theoretical studies have identified candidate materials to activate the time reversal breaking[53]. On the experimental side a number of ferromagnetic insulators have been grown with the aim of opening a gap in the spectrum of the surface states of topological insulators. Exchange coupling induced symmetry breaking has been observed when Bi_2Se_3 is grown on ferromagnetic EuS[54]. The

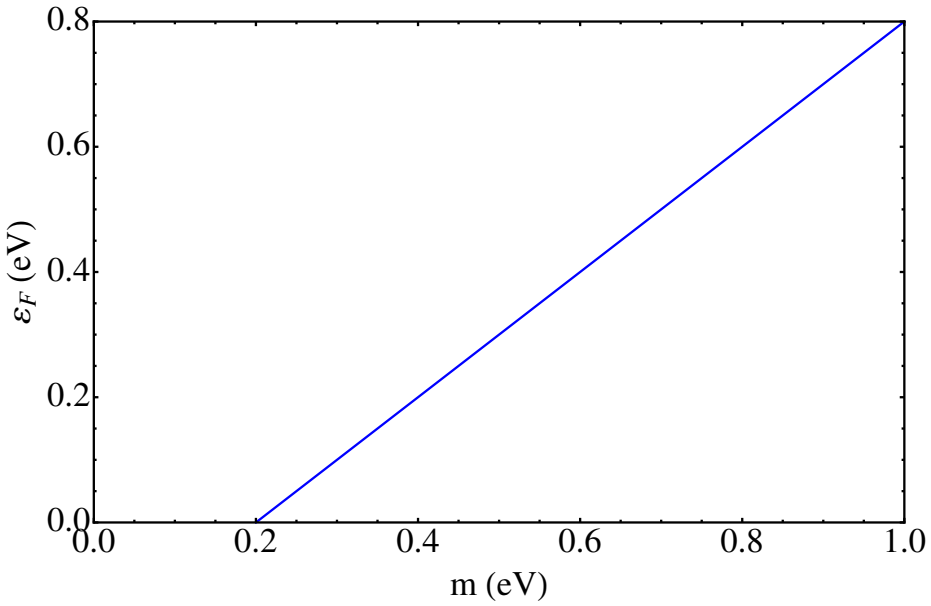


Figure 2.12: As m is varied, the density at which the jump in frequency occurs is modified. Here we plot the variation and note that it occurs for small densities when m is not too much larger than the difference $|\Delta_S - \Delta_D|$.

induced magnetic moment at the interface at low temperatures is $1.3 \pm 0.5 \times 10^2$ μ_B/nm^2 with a transition at about 20 K. EuO is a viable candidate but so far only growth on graphene has been demonstrated with a transition temperature of 69 K [55]. $Cr_2Ge_2Te_6$ has a transition temperature of 61 K [56] and is another possible substrate for epitaxial growth[57]. While YIG is an actively researched ferromagnetic insulator, its transition temperature of 559 K results in a constant magnetization at low temperatures which prevents its use as a tunable knob.

An alternative scenario is to follow the original suggestion of [2, 25] where a magnetically doped topological insulator is sandwiched between normal insulator layers. The ability to magnetically dope topological insulators has been experimentally demonstrated and resulted in the observation of the quantum anomalous hall effect [58]. The tempera-

tures at which the phenomenon is observed is 30 mK while the Curie temperature is 15 K. Ordering the moments in plane, rather than perpendicular to the interface will achieve the required geometry. Whether the requirements for line nodal semimetals are as stringent in terms of temperature is yet to be determined. Nevertheless the progress suggests that the prospect of growing devices with Weyl semimetallic characteristics is indeed promising, opening the possibility of new tunable devices discussed in this paper.

2.7 Conclusions

In this paper we have focussed on the tunability of the low energy sector of a heterostructure which is in a topological semimetallic phase with line nodes. The key insight is the dependence of the dispersion on the strength of the time reversal breaking. For an insulating magnetic layer, this is controlled by the magnetization which in turn depends on temperature. For example EuO has a T_c of 69.3 K and cooling provides a knob to continuously vary the magnetization. As one increases the magnetization, the gap in the spectrum closes and the line node appears. This evolves from a closed loop to two open lines which span the Brillouin zone in the direction parallel to the growth axis of the multilayer. The associated changes on density of states and topology of equal energy surfaces results in measurable signatures in thermodynamic and transport properties. We show that the slope of the density of states rises monotonically as a function of m as long as the line node is closed and is roughly constant for larger values. The trend is also reflected in conductivity.

The toroidal topology also has interesting implications for quantum oscillations in this device. On doping the system the minor radius of the torus grows and for sufficiently

large densities the equal energy surface changes topology to a sphere. This is accompanied by the doubling of the oscillation frequency for magnetic fields perpendicular to the symmetry axis of the torus. This is accessible even for small densities.

As noted in [25], the nodal line is not robust and that perturbations, such as particle-hole asymmetry, induce an energy dependence to the line where the bands touch. Thus the system is converted to a normal semimetal with electron-hole pockets. Nevertheless the size of these pockets depend on the size of the line node which in turn depends on m. Thus the qualitative feature of the evolution of density of states and associated properties as a function of magnetization continue to hold. The same is true of the change in geometry of the nodal line from a closed to an open one.

Chapter 3

Kondo Screening in p-Type Monolayer Transition Metal Dichalcogenides

3.1 Introduction

Single layer Transition metal Group-VI Dichalcogenides (TMDs), MX_2 (M = Mo, W; X=S, Se, Te), are direct band gap semiconductors whose physics is strongly influenced by spin orbit coupling. While they share the hexagonal crystal structure of graphene, they differ in three important aspects: 1) The spectrum possesses gaps at the K-points as opposed to Dirac nodes; 2) Broken inversion symmetry and coupling of the spin with momentum result in a large splitting of the valence bands; and 3) The two bands near the chemical potential arise from the partial filled transition metal d-orbitals[29, 59–61]. A striking consequence

is the nontrivial Berry's phase of the low energy bands. The symmetry of the system is such that the z component of spin, s_z (i.e. component perpendicular to the MX_2 plane) is conserved. Associated with each band is a Berry curvature, $\mathbf{\Omega}$, whose z component changes sign going from one valley to the other, and also when going from the conduction to the valence band. These properties allow for coupled valley and spin phenomena[29, 62].

Of particular significance is the ability to manipulate the valley degree of freedom. The Berry curvature engenders an intrinsic angular momentum associated with Bloch wave functions [63], which in turn allows for spin preserving transitions between valence and conduction bands induced by optical fields even though the atomic orbitals involved all have d character. Furthermore, the valley dependent sign of the Berry curvature leads to selective optical excitation where right circular polarization couples to one valley and left to the other. As a consequence a number of valleytronic and spintronic applications are enabled and have attracted a lot of attention over the last few years [27, 29, 62, 64, 65].

While much of the focus thus far has been on the nontrivial properties engendered in the noninteracting limit, our work emphasizes the band structure and valley contrasting probe to study and manipulate correlated phenomena in these systems. This is particularly interesting in hole doped systems where an experimentally accessible window in energy is characterized by two disconnected pieces of spin nondegenerate Fermi surfaces (see Fig. 3.1). (Note that these considerations do not apply to MoS_2 because there is also a spin degenerate Fermi surface at the Γ point.) Since one can preferentially excite electrons from one or the other Fermi surface, optical probes have spin specificity. These features have important implications on magnetic phenomena. Consequently we explore the nature of the Kondo

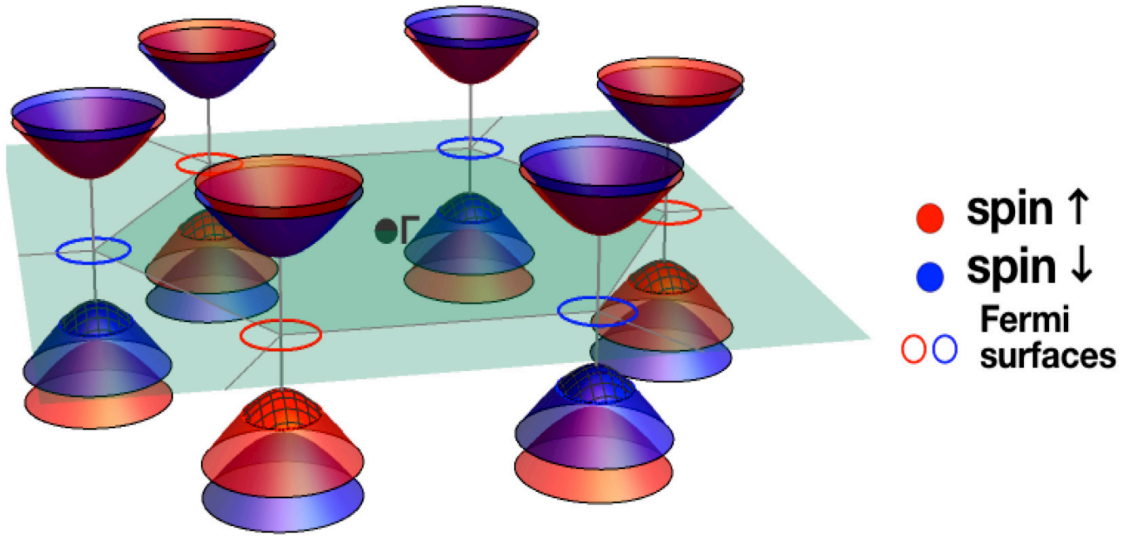


Figure 3.1: Low energy band structure of hole doped TMD. The unique aspect of the system is the spin split band allowing for spin nondegenrate Fermi surfaces around the K points.

effect. In doing so, particularly in the assessment of optical probing and manipulation, we employ two methods: a variational wave function[36, 37], and the numerical renormalization group (NRG)[38, 39, 66].

In conventional metals the screening of an isolated magnetic impurity relies on the formation of a singlet state between the impurity moment and the electrons. In TMDs the up and down spins at the same energy occupy different valleys and spin flip scattering requires inter valley processes. For a hole doped system, where the chemical potential intersects only one of the two spin split bands, the main findings are as follows: i) the Kondo resonance is an equal admixture of singlet and the $m = 0$ triplet formed between the impurity spin and the band fermions. Thus the ground state has total spin $(\mathbf{S}+\boldsymbol{\sigma})^2 = J^2 \approx \hbar^2$, where $\mathbf{S}$ and $\boldsymbol{\sigma}$

are spin operators for the impurity and band fermions respectively. The result reflects the fact that the Kondo energy scale as well as the level broadening are small compared to the spin splitting scale which is $\sim$ 0.1-0.5 eV; ii) the hybridization of the impurity state with the TMD depends crucially on the interplay between the symmetry of the atomic orbitals involved and band topology (i.e. Berry curvature). To illustrate, orbitals with similar atomic overlap with the fermionic states have different hybridization due to the additional orbital angular momentum associated with the Berry curvature; iii) the spin specificity of opto-electronic coupling allows access to components of the screening cloud which in turn allows for the tuning of spin in the Kondo state.

We first introduce the specifics of the model for Anderson impurities in monolayer TMDs (Sec. 3.2). The results of the spin structure are obtained using a variational wave-function approach (Sec. 3.3) for a single impurity located on top of a M (Mo or W) site. The location is chosen for illustrative purposes to show the interplay of topology and interaction, and other high symmetry sites for the impurity only modify the precise form of the hybridization. Since the density of states is always finite in the hole doped systems, the energetics and stability of the Kondo resonance are rather conventional. What is striking however is the composition of the Kondo cloud and its physical properties as emphasized above. Additionally, to understand the effect of spin/valley specific optical coupling, we find that the Kondo ground state starting from an optically excited Fermi sea is insufficient and a better picture is obtained from NRG (Sec. 3.4). In this case we do not find J^2 but we do expose a component in the Kondo cloud with a shift $J_z \neq 0$ which scales with the strength of optical field excitation, revealing a very strong tunability of the correlated

spin state with optical probes. Prior to concluding we compare the variational and NRG methods and results (Sec. 3.5).

3.2 Model

In this section we describe the material and impurity model Hamiltonians.

3.2.1 Low Energy Bands and Topology

The minimal model for TMDs in the low energy bands near $\mathbf{K}$ ($\mathbf{K}'$) is in terms of the two basis functions $|1\rangle = |d_{z^2}\rangle$ and $|2\rangle = \frac{1}{\sqrt{2}}\left(\left|d_{x^2-y^2}\right\rangle + i\tau\left|d_{xy}\right\rangle\right)$. The Hamiltonian is

$$H_m = at\left(\tau\sigma_x k_x + \sigma_y k_y\right) + \frac{\Delta}{2}\sigma_z - \lambda\tau\frac{\sigma_z - 1}{2}s_z \tag{3.1}$$

where σ_i are Pauli matrices in the space of two bands represented by the eigenvalues ± 1 of σ_z, $\tau = \pm 1$ is the valley index, s_z is the Pauli matrix for spin, a is the lattice constant, t is the effective hopping parameter, Δ is the gap at the K points and λ is the spin orbit coupling [29, 61]. Written in terms of the magnitude $k = |\mathbf{k}|$ and azimuthal angle $\phi = \arctan\left(k_y/k_x\right)$, the Hamiltonian (3.1) is diagonalized by the unitary matrix $U(\mathbf{k}, \tau, s)$:

$$U(\mathbf{k}, \tau, s) = \begin{pmatrix} \chi_{k,\tau,s} & w_{k,\tau,s} \\ \tau w_{k,\tau,s} e^{i\tau\phi} & -\tau\chi_{k,\tau,s} e^{i\tau\phi} \end{pmatrix} \tag{3.2}$$

with $\chi_{k,\tau,s} = \cos\left(\theta_{k,\tau,s}/2\right)$, $w_{k,\tau,s} = \sin\left(\theta_{k,\tau,s}/2\right)$ and Bloch angles

$$\cos\left(\theta_{k,\tau,s}\right) = \frac{(\Delta - \lambda\tau s)}{\sqrt{(\Delta - \lambda\tau s)^2 + (2atk)^2}} \tag{3.3}$$

where $s = \pm$ for eigenvalues of s_z. The eigenvalues, the diagonal elements of $U^\dagger H_m U$ labeled $n = \pm 1$, are given by $E_{n,k,\tau,s} = \frac{1}{2}(\lambda s\tau + n\sqrt{(2atk)^2 + (\Delta - \lambda s\tau)^2})$. The Berry curvature is

encoded in $\theta_{k,\tau,s}$. Mapping $(\mathbf{k}, E_{+,k,\tau,s}) \to (\phi, \tau\theta_{k,\tau,s})$ and $(\mathbf{k}, E_{-,k,\tau,s}) \to (\phi, \tau\theta_{k,\tau,s} - \tau\pi)$ wraps the conduction and valence bands (respectively) onto half the Bloch sphere with the texture of a skyrmion (either chiral or hedgehog).

3.2.2 Hybridization

To study the nature of Kondo screening in a hole doped system, where the chemical potential is in the topmost spin split valence band, we introduce an impurity orbital on top of the M atom. The choice is for simplicity and does not affect the results as long as a site of high symmetry is chosen. For generality however, this section does not presume a specific location — the on-site choice is evaluated and employed in following sections. The magnetic impurity brings its own orbital with Coulomb repulsion, $H_{imp} = \sum_s \varepsilon_0 f_s^\dagger f_s + U n_{f,\uparrow} n_{f,\downarrow}$. Next, since the Hamiltonian (3.1) is only an effective low energy theory, we impose an upper cutoff in energy, Λ, within which its hybridization with the impurity takes the form [32, 67, 68]

$$H_V = \sum_{\alpha,\tau,s} \sum_j \left(V_{\alpha,\tau,j} a^\dagger_{\alpha,\tau,s}(\mathbf{r}_j) f_s + h.c. \right) \tag{3.4}$$

where $a^\dagger_{\alpha,\tau,s}(\mathbf{r}_j) = N_M^{-1/2} \sum_{\mathbf{k}} a^\dagger_{\alpha,\mathbf{k},\tau,s} \mathrm{e}^{-i\mathbf{k}\cdot\mathbf{r}_j}$ is the creation operator at M site $\mathbf{r}_j$ with $\alpha =$ 1 or 2 corresponding to the basis states. The sum over j runs over the M nearest to the impurity site, f_s is the annihilation operator of the localized electron on the impurity (taken as the origin), and $V_{\alpha,\tau,j}$ is the hybridization strength between the localized orbital with the $|1\rangle$ and $|2\rangle$ orbitals on the M atom at site j.

To analyze the screening of impurity moments we must first project to the eigenspace, $a_{\alpha,\mathbf{k},\tau,s} = \sum_{n=\pm} U_{\alpha,n}(\mathbf{k}, \tau, s) c_{n,\mathbf{k},\tau,s}$. Generally, this means that the TMD and hybridization

Hamiltonians are simply

$$H_m = \sum_{n,\mathbf{k},\tau,s} E_{n,k,\tau,s} c^\dagger_{n,\mathbf{k},\tau,s} c_{n,\mathbf{k},\tau,s} \tag{3.5}$$

$$H_V = \frac{1}{\sqrt{N_M}} \sum_{n,\mathbf{k},\tau,s} \left(v_{n,\mathbf{k},\tau,s} c^\dagger_{n,\mathbf{k},\tau,s} f_s + h.c. \right) \tag{3.6}$$

where $v_{n,\mathbf{k},\tau,s} = \sum_j \left(\sum_{\alpha=1,2} U^\dagger_{n,\alpha}(\mathbf{k},\tau,s) V_{\alpha,\tau,j} \right) \mathrm{e}^{-i\mathbf{k}\cdot\mathbf{r}_j}$. Owing to the structure of the U matrices from (3.2), terms with no angular dependence pair with the $\alpha = 1$ orbital whereas those with the dependence $\sim \mathrm{e}^{-i\tau\phi}$ pair with the $\alpha = 2$ orbital.

To address the angular dependence rigorously, a discussion which is especially useful in the context of NRG [39], we transform to a quasi-angular momentum (QAM) basis (termed so because ϕ is defined with respect to the K rather than the Γ point). The $\mathbf{k}$-dependence is recast as the magnitude k and a quasi-angular momentum index $m \in (-\infty, \infty)$ [69]. The sums become $\sum_{\mathbf{k}} \to N_M \Omega_c/(2\pi)^2 \int d^2k$ and the eigenstate operators in the QAM basis are obtained with $c_{n,\mathbf{k},\tau,s} = (N_M \Omega_c k/2\pi)^{-1/2} \sum_m \mathrm{e}^{im\phi} c_{n,k,m,\tau,s}$, where $\Omega_c = (\sqrt{3}/2)a^2$ is the area of a unit cell. The Hamiltonians transform to

$$H_m = \sum_{n,m,\tau,s} \int dk\, E_{n,k,\tau,s} c^\dagger_{n,k,m,\tau,s} c_{n,k,m,\tau,s} \tag{3.7}$$

$$H_V = \sum_{n,m,\tau,s} \int dk \sqrt{\frac{\Omega_c k}{2\pi}} \left(v_{n,k,m,\tau,s} c^\dagger_{n,k,m,\tau,s} f_s + h.c. \right) \tag{3.8}$$

with an effective coupling $v_{n,k,m,\tau,s} = \int (d\phi/2\pi) v_{n,\mathbf{k},\tau,s} \mathrm{e}^{-im\phi}$ to the impurity. This form has departed greatly from the original $V_{\alpha,\tau,j}$ appearing in Eq. (3.4); the relationship is revealed by expanding in Bessel functions,

$$v_{n,\mathbf{k},\tau,s} = \sum_{\alpha=1,2} U^\dagger_{n,\alpha}(\mathbf{k},\tau,s) \sum_m \mathrm{e}^{im\phi} \overline{V}_{\alpha,k,m,\tau} \tag{3.9}$$

$$\overline{V}_{\alpha,k,m,\tau} = \sum_j V_{\alpha,\tau,j} (-i)^m J_m(kr_j) \mathrm{e}^{-im\phi_j} \tag{3.10}$$

where ϕ_j is the real-space angle from the position $\mathbf{r}_j$ of the M atom. To continue, one would like to integrate and arrive at a relation between $v_{n,k,m,\tau,s}$ and $\overline{V}_{\alpha,k,m,\tau}$, but the angular dependence in $U(\mathbf{k},\tau,s)$ complicates matters. Fortunately, the matrix may be factored into two distinct parts

$$U(\mathbf{k},\tau,s) \equiv M(\phi,\tau)\cdot N(k,\tau,s) = \begin{pmatrix} 1 & 0 \\ 0 & \mathrm{e}^{i\tau\phi} \end{pmatrix} \cdot \begin{pmatrix} \chi_{k,\tau,s} & w_{k,\tau,s} \\ \tau w_{k,\tau,s} & -\tau\chi_{k,\tau,s} \end{pmatrix} \tag{3.11}$$

so that the hybridization may be written in the alternate form

$$H_V = \sum_{m,\tau,s} \int dk \sqrt{\frac{\Omega_c k}{2\pi}} \times \\ \times \left\{ \begin{pmatrix} \overline{V}_{1,k,m,\tau} \\ \overline{V}_{2,k,m,\tau} \end{pmatrix}^T \cdot \begin{pmatrix} \chi_{k,\tau,s} c^\dagger_{+,k,m,\tau,s} + w_{k,\tau,s} c^\dagger_{-,k,m,\tau,s} \\ \tau w_{k,\tau,s} c^\dagger_{+,k,(m-\tau),\tau,s} - \tau\chi_{k,\tau,s} c^\dagger_{-,k,(m-\tau),\tau,s} \end{pmatrix} f_s + h.c. \right\}. \tag{3.12}$$

Note that the interaction $V_{1,\tau,j}$ couples only to the host states with quasi-angular momentum m, while $V_{2,\tau,j}$ couples only to the states with $m-\tau$. Interestingly, this pattern originates from a gauge choice in the diagonalization of (3.1) so we expect physical quantities be independent of the actual value of the QAM labels.

The above results reduce to the case of graphene and topological insulator when the gap and spin splitting vanish, $\Delta = \lambda = 0$ [67, 69, 70]. The key new aspect due to the Berry curvature is the dependence of the hybridization on the angle $\theta_{k,\tau,s}$ which encodes the nontrivial topology of the states, in addition to the orbital wave-function overlap that determines $V_{\alpha,\tau,j}$ and $\overline{V}_{\alpha,k,m,\tau}$.

3.2.3 Impurity at M Site

We focus on the Kondo effect for magnetic adatoms, where the impurity state is on the M site and the overlap (3.4) is with only one M atom. Symmetry mandates two classes: i) orbitals of type I defined as s, p_z, d_{z^2} and $f_{5z^3-3zr^2}$ couple to orbital $|1\rangle$, and ii) type II orbitals $d_{x^2-y^2}, d_{xy}, f_{zx^2-zy^2}$ and f_{zxy} couple to orbital $|2\rangle$. Therefore the hybridization strength $V_{\alpha,\tau,j}$ is nonzero for $\alpha = 1$ or 2 but not both, implying H_V enters with trivial angular dependence. Since the adatom orbitals have maximum overlap with the nearest M site the hybridization strength is $V_{\alpha,\tau,j} = V_{\alpha,\tau}\delta_{\mathbf{r}_j,0}$. Also, since we are interested in hole doped systems we project to the valence band. Then the simple form (3.6) for type I becomes

$$H_V = \sum_{\mathbf{k},\tau,s} \left(v^1_{-,\mathbf{k},\tau,s} c^\dagger_{-,\mathbf{k},\tau,s} f_s + h.c. \right) \tag{3.13}$$

with $v^1_{-,\mathbf{k},\tau,s} = w_{k,\tau,s} V_1$. For the type II case, the corresponding definition will need $w \to -\tau\chi e^{-i\tau\phi}$. The Berry curvature plays a crucial role in determining the coupling: $\theta_{k,\tau,s}$ goes from the north pole of the Bloch sphere at K (K') to the equator as k increases. Thus type II orbitals couple more strongly to the valence band than type I.

As above, for NRG it is useful to have the hybridization decomposed into QAM channels. Under the same conditions, the impurity lying on top of an M site gives $\overline{V}_{\alpha,k,m,\tau} = V_{\alpha,\tau,0}\delta_{m,0}$ so the alternate form (3.12) for type I is

$$H_V = \sum_{\tau,s} \int dk \sqrt{\frac{\Omega_c k}{2\pi}} \left(w_{k,\tau,s} V_1 c^\dagger_{-,k,0,\tau,s} f_s + h.c. \right). \tag{3.14}$$

This is clearly just Eq. (3.13) transformed to the new basis with apparently no change. On the other hand, for type II, we would see the same as above but with $w \to -\tau\chi$, as well as a shifted QAM label $0 \to -\tau$ on the operators. Thus the alternate forms (3.14) and (3.12)

are equivalent to the simpler (3.13) and (3.6), but with all angular dependence shifted to the operators with QAM labels. We will not employ this last form until the NRG setup where it is useful.

3.3 Variational Wave Function

We examine the ground-state properties using the variational wave-function approach. This method is known to capture the main spin content and energy scale of the Kondo effect, though further details and exceptional situations may be missed. The full Hamiltonian is $H = H_0 + H_V$, where $H_0 = H_m + H_{imp}$ describes the system with the impurity [32, 34], and H_V is written in the form (3.13). All energies are measured relative to the chemical potential μ.

For large Coulomb repulsion on the impurity level the variational state $|\psi\rangle$ includes the ground state of the pure system $|\psi_0\rangle$ and states with a singly occupied impurity level [36, 37]. Since inversion is broken both singlet and triplet combinations must be included[1]. Therefore,

$$|\psi\rangle = b_0 |\psi_0\rangle + \sum_\ell \left[p_\ell (f^\dagger_\uparrow c_{\ell,\uparrow} + f^\dagger_\downarrow c_{\ell,\downarrow}) + t_\ell (f^\dagger_\uparrow c_{\ell,\uparrow} - f^\dagger_\downarrow c_{\ell,\downarrow}) \right] |\psi_0\rangle \tag{3.15}$$

where b_0 is the amplitude of the ground state in the absence of the impurity, p_ℓ is the singlet amplitude, and t_ℓ is the triplet amplitude, giving a total of three variational parameters. For brevity we use $\ell = \{n, \mathbf{k}, \tau\}$. This state can be written more compactly by defining

[1] See Appendix C for details on the construction of this state and the following variational calculations, including parameters and the spin of the state.

$B_{\ell,s} = p_\ell + s\, t_\ell$:

$$|\psi\rangle = b_0 \,|\psi_0\rangle + \sum_{\ell,s} B_{\ell,s} f_s^\dagger c_{\ell,s} \,|\psi_0\rangle \,. \tag{3.16}$$

3.3.1 Variational Parameters

We determine the variational parameters and ground-state energy when the impurity level sits below the chemical potential, $\varepsilon_0 < 0$. The energy is written as $\langle\psi|\, H \,|\psi\rangle = (E_0 + \varepsilon_0 + \epsilon)\,\langle\psi|\psi\rangle$ where $E_0 = \langle\psi_0|\, H_m \,|\psi_0\rangle$, subject to the constraint $\langle\psi|\psi\rangle = 1$. The energy shift ϵ is determined by minimization, which then yields the variational parameters,

$$b_0 = \frac{1}{\sqrt{N_M}} {\sum_{\ell,s}}' \frac{v_{\ell,s} B_{\ell,s}}{\varepsilon_0 + \epsilon} \tag{3.17}$$

$$B_{\ell,s} = \frac{1}{\sqrt{N_M}} \frac{v^\star_{\ell,s} b_0}{\varepsilon_{\ell,s} + \epsilon}. \tag{3.18}$$

The notation $\sum'_{\ell,s}$ indicates summation over occupied states states: $E_{\ell,s} - \mu \equiv \varepsilon_{\ell,s} < 0$. Solving for ϵ,

$$\epsilon = -\varepsilon_0 + \frac{1}{N_M} {\sum_{\ell,s}}' \frac{|v_{\ell,s}|^2}{\varepsilon_{\ell,s} + \epsilon}. \tag{3.19}$$

Imposing the normalization $\langle\psi|\psi\rangle = 1$, the singlet/triplet parameters are found in terms of ϵ and b_0 given by

$$b_0 = \left[1 + \frac{1}{N_M} {\sum_{\ell,s}}' \frac{|v_{\ell,s}|^2}{(\varepsilon_{\ell,s} + \epsilon)^2} \right]^{-1/2} . \tag{3.20}$$

Using the above results we state the solution in terms of the original singlet/triplet parameters: $p_\ell = (B_{\ell,\uparrow} + B_{\ell,\downarrow})/2$, and $t_\ell = (B_{\ell,\uparrow} - B_{\ell,\downarrow})/2$. In the absence of spin orbit coupling, every point in **k**-space is doubly degenerate and we expect the singlet parameters to survive while the triplet parameters to go to zero. Indeed, for weak spin orbit coupling (i.e. $\lambda \ll \Delta$), to leading order $p_\ell \propto$ const. and $t_\ell \propto \lambda$.

For hole doped systems of interest, $-\frac{\Delta}{2} - \lambda < \mu < -\frac{\Delta}{2} + \lambda < 0$. With cutoff $E_{-1,k_\Lambda,s,s} = -\Lambda$, Eq. (3.19) to leading order is

$$\epsilon = -\varepsilon_0 + 2\,\Omega_c \int_{k_\mu}^{k_\Lambda} dk\, \frac{|v_{\ell,s}|^2}{E_{\ell,s} - \mu + \epsilon}\bigg|_{\substack{n=-1 \\ \tau=s}} . \tag{3.21}$$

The integrand is strongly peaked at the chemical potential. Thus for $|\epsilon| \ll |\varepsilon_0|$, the shift is

$$\epsilon \approx -(\Lambda - |\mu|)\mathrm{e}^{\varepsilon_0/2g(\mu)|v_\mu|^2} \tag{3.22}$$

where $g(\mu) = \frac{\sqrt{3}}{8\pi t^2}\,|2\mu - \lambda|$ is the density of states and $|v_\mu|^2 \equiv V_1^2 w_\mu^2 = \frac{V_1^2}{2}\left(1 - \frac{\Delta - \lambda}{2|\mu| + \lambda}\right)$ is the effective type I hybridization, at the chemical potential.

For $\lambda = 0$ there is no spin splitting. Thus the density of states is typically doubled compared to the spin split case studied here. Thus the Kondo temperature is lowered for large λ[70–72]. In Fig. 3.2 we plot the Kondo energy scale ϵ as a function of the inverse hybridization strength times the density of states: $Vg \equiv V_1 g(\mu)$ with $\Lambda = \Delta$ and $\varepsilon_0 = -\Delta/20$. Results are shown for different TMDs when the chemical potential is halfway between the spin split valence bands, $\mu = -\Delta/2$. The larger density of states and a larger deviation away from the pole of the Bloch sphere leads to an enhanced Kondo scale for WS_2 and WSe_2 as compared to $MoSe_2$, revealing the mixed influence of the band and its topological character.

3.3.2 Spin and Susceptibiltiy

Since time reversal symmetry is not broken, the expectation value of the impurity spin $\langle \mathbf{S} \rangle$ and the electron spin $\langle \boldsymbol{\sigma} \rangle$ individually go to zero. We verify this by explicitly computing $\langle \mathbf{S} \rangle$ and $\langle \boldsymbol{\sigma} \rangle$. Since only the $m = 0$ component of the triplet is admixed, the x and y components

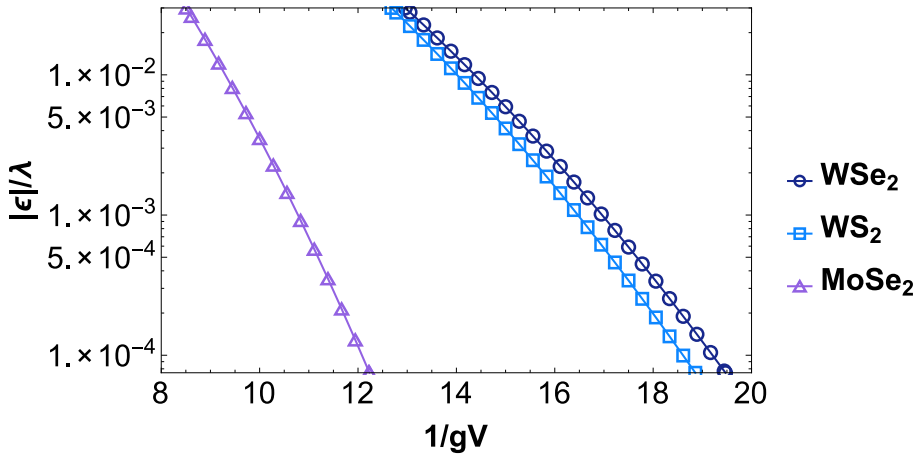


Figure 3.2: Kondo energy scale for TMDs as a function of the inverse of the hybridization normalized to the spin splitting and density of states respectively, for the case where the chemical potential is halfway between the spin split valence bands.

are automatically zero. The z components are given by

$$\langle\psi|\, S_z\, |\psi\rangle \equiv \langle S_z\rangle = {\sum_{\ell,s}}' s|B_{\ell,s}|^2 = -\langle\sigma_z\rangle \tag{3.23}$$

$$= {\sum_{\ell}}' (|B_{\ell,\uparrow}|^2 - |B_{\ell,\downarrow}|^2). \tag{3.24}$$

The sum is zero due to time reversal symmetry.

The existence of the triplet component implies that the impurity is under screened. Thus we consider the expectation value of the total spin $\mathbf{J}^2 = (\mathbf{S} + \boldsymbol{\sigma})^2$. Due to spin orbit coupling in the pure system the ground state $|\psi_0\rangle$ does not have a simple singlet configuration, so the meaningful quantity is $\langle J^2\rangle \equiv \langle\psi|\, \mathbf{J}^2\, |\psi\rangle - \langle\psi_0|\, \boldsymbol{\sigma}^2\, |\psi_0\rangle$. Defining also $\delta\theta_k \equiv \theta_{k,+,\uparrow} - \theta_{k,+,\downarrow}$, the difference in polar angle on the Bloch sphere of opposite spin states,

$$\langle J^2\rangle = 2\sum_{\tau,\mathbf{k}=k_\mu}^{k_\Lambda} \cos\frac{\delta\theta_k}{2}\left[|p_{-1,\mathbf{k},\tau}|^2\left(\cos\frac{\delta\theta_k}{2} - 1\right) + |t_{-1,\mathbf{k},\tau}|^2\left(\cos\frac{\delta\theta_k}{2} + 1\right)\right] \tag{3.25}$$

$$\approx \cos^2\frac{\delta\theta_\mu}{2}. \tag{3.26}$$

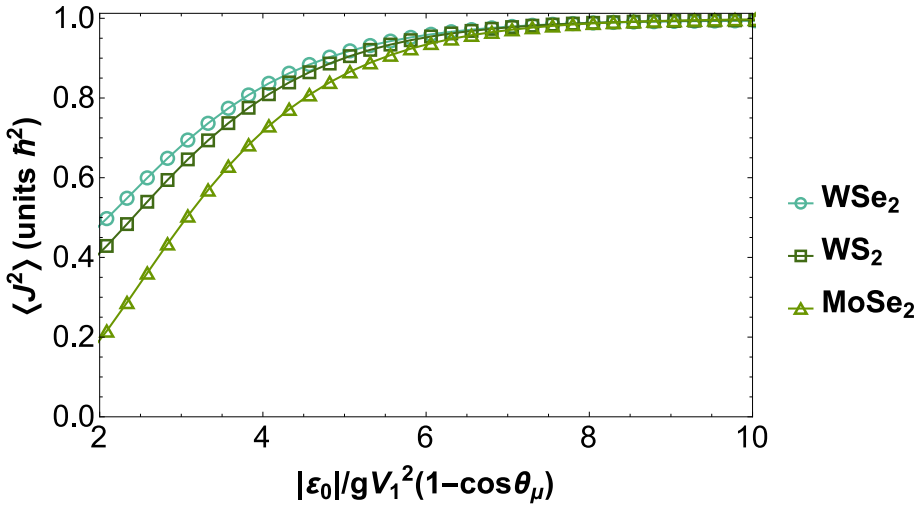


Figure 3.3: The expectation value of J^2 is plotted as a function of the effective coupling that controls the Kondo scale (see Eq. (3.22)).

In Fig. 3.3 we plot the variation of $\langle J^2 \rangle$ as a function of the exponent on the RHS in Eq. (3.22). For weak hybridization, the resonance is an equal mixture of singlet and triplet and $\langle J^2 \rangle \approx \hbar^2$. The interacting system remains nonmagnetic, as revealed by $\langle \mathbf{J} \rangle = 0$, but fluctuations give $\langle J^2 \rangle \neq 0$. Note that the pure system also has these fluctuations; the additional contribution from the Kondo mixture alone is given by Eq. (3.25). As the hybridization gets larger so does the width of the Kondo resonance leading to a decrease in J^2. Since the spin splitting in WS_2 and WSe_2 is large compared to $MoSe_2$, the deviation away from $\hbar^2$ occurs for a larger value of V_1 for the former two.

Concluding this section we consider the magnetic susceptibility. Note that the conservation of the z-component of spin yields an anisotropic susceptibility. For the ground state considered here we focus on the out of plane response. To do so we couple the magnetic field to the impurity spin which further splits the energies: $\varepsilon_{\ell,s} \to \overline{\varepsilon}_{\ell,s} = \varepsilon_{\ell,s} + \mu_0 h_z s$. The only nonzero component of the susceptibility tensor is $\chi^{imp} \equiv \chi^{imp}_{zz} = \frac{d}{dh_z}\mu_0 \langle S_z \rangle$. The zero

field value is

$$\chi^{imp}|_{\mathbf{h}=0} = \frac{2\mu_0^2 b_0^2}{N_M} \sum_{\ell,s}{}' \frac{|v_{\ell,s}|^2}{|\varepsilon_{\ell,s} + \epsilon|^3} \sim |\epsilon|^{-1}. \tag{3.27}$$

Thus a finite spin orbit coupling reduces the Kondo energy scale enhancing the susceptibility.

3.3.3 Optically Excited Kondo State

With the Kondo state and its properties for the simple hole doped case in hand, we next build a Kondo state starting from an optically excited TMD. Ultimately, we are interested in the spin properties of the Kondo state formed in the presence of optical excitations, but first we must build the pure excited state. In this case, for appropriate frequencies affecting states near the chemical potential $\hbar\omega \sim 2|\mu| + \lambda$, states are taken from the upper valence bands to the upper conduction bands via spin-preserving vertical transitions that are k-dependent and highly valley selective[29]. Once the states are excited they can relax to the conduction band minimum and eventually back to the chemical potential, only to be excited again. The steady-state Fermi sea with optical excitations depends on all the scattering rates involved and is thus complicated to determine thoroughly, however we may construct a simple state that captures the main points.

Due to the valley selective circular dichroism, we allow the valence band valleys to be unequally populated, the chemical potentials lowered by δ_τ. Denoting right/left circular polarization $\nu = \pm$, we can write $\delta_\nu - \delta_{-\nu} > 0$ since the primarily activated valley has $\tau = \nu$. Due to the form of transition amplitudes (see Ref. [29]), the shifts are approximately related by $\delta_{-\nu} = q\delta_\nu$ with $q = |P_-(k_\mu)|^2/|P_+(k_\mu)|^2$ and

$$|P_{\pm}(k_\mu)|^2 = \left(\frac{m_0 a t}{\hbar}\right)^2 \left(1 \pm \cos\theta_{k_\mu,+,\uparrow}\right)^2, \tag{3.28}$$

where m_0 is the free electron mass. Since the lower (filled) bands are essentially inert and valley-selectivity translates to spin-selectivity in the hole doped regime of interest (as in Fig. 3.1), one can interpret the above shifts as a difference in spin up/down chemical potentials, $\mu_\uparrow - \mu_\downarrow = \delta_- - \delta_+ \approx -\nu\delta_\nu$.

Remembering the excited states in the conduction band and valley (spin) conservation, we write the sum over conduction band states formally as $\sum_{\mathbf{k}}^{ex}$ with

$$\sum_{\mathbf{k}}^{ex} 1 \equiv \sum_{\mathbf{k}=0}^{k_{ex,\tau}} 1 = \sum_{\mathbf{k}=k_\mu}^{k_{\mu-\delta_\tau}} 1. \tag{3.29}$$

Now the excited Fermi Sea is

$$|\psi_0^{ex}\rangle = \prod_{\tau} \prod_{\boldsymbol{\xi}=0}^{k_{ex,\tau}} \prod_{\mathbf{k}=k_{\mu-\delta_\tau}}^{k_\Lambda} c^\dagger_{+1,\boldsymbol{\xi},\tau,\tau} c_{-1,\mathbf{k},\tau,\tau} |\psi_0\rangle . \tag{3.30}$$

With this new 'ground state', we can again analyze the Kondo physics and determine the effect on total spin $\langle J^2 \rangle$. Typically the Kondo bound state forms with the highest energy states having the largest amplitude, but here the conduction band states are all excited and short-lived so we focus on the valence band states near the offset chemical potentials. Due to unequal offsets the valley $\tau = -\nu$ has higher energy and is dominant; the result is that the main equations (3.17)-(3.20) simply require shifts $\varepsilon_0 \to \varepsilon_0 + \delta_{-\nu}$ and $\varepsilon_{\ell,s} \to \varepsilon_{\ell,s} + \delta_{-\nu}$.

Despite their simplicity, evaluating the Kondo results (e.g. energy) is not very straightforward; since the correction to the energy shift is expected to be minuscule we apply the previous result (3.22) here as well. As for the spin results, conservation of spin

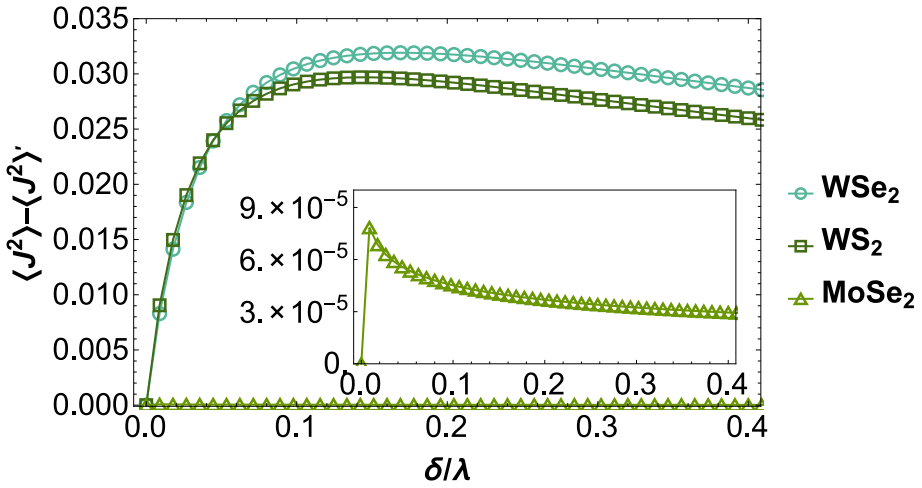


Figure 3.4: The difference in expectation values of J^2 from normal Fermi sea compared to excited case, plotted against the chemical potential shift in the selected valley, $\delta \equiv \delta_\nu$, compared to the spin splitting λ. The unexcited case is always greater so the difference shown is always positive.

requires that the system is still nonmagnetic $\langle \mathbf{J} \rangle^{ex} = 0$ while the total spin $\langle J^2 \rangle^{ex} \equiv \langle \psi^{ex} | \mathbf{J}^2 | \psi^{ex} \rangle - \langle \psi_0^{ex} | \boldsymbol{\sigma}^2 | \psi_0^{ex} \rangle$ takes an approximate form similar to (3.25). The result is shown in Fig. 3.4, where we have fixed the value $1/gV = 13$ (cf. Fig. 3.2). It is important to note that we have included the conduction band in $\mathbf{J}$; if one is looking only at the valence bands, $\mathbf{J}_{val}$, the equivalent result is that the spin is not changed upon introduction of the impurity: $\langle \mathbf{J}_{val} \rangle^{ex} = \langle \mathbf{J}_{val} \rangle_0^{ex}$.

Interestingly, the valley/spin specificity of optical excitations is not the controlling factor for the properties of the this variational state. Indeed, the result for tuning the spin state is independent of which circular polarization is used. Rather, the key factor is the further deviation of the Bloch angles from the pole as one effectively lowers the chemical potential in either (or both) valleys. The spin state in each valley is still an equal mixture of singlet and triplet (as mandated by the hole-doped band structure) so we are required to

still have $\langle J^2 \rangle \approx \hbar^2$, with any difference due to the projection to eigenstates (i.e. the Bloch angles).

3.4 Numerical Renormalization Group

The case of a magnetic impurity in a Fermi sea with effectively offset spin up/down chemical potentials is of particular interest. The variational method above, which ought to present the main features of the ground state, ignores all doubly-occupied states and may miss crucial features of the offset system; specifically, only combinations with zero spin along z are allowable in the state (3.15) even in the case of an excited Fermi sea. Thus in this section we assess the same system, including both zero and finite offset of chemical potentials, using Wilson's numerical renormalization group (NRG) method [38].

Before entering the discussion we explain the focus of our NRG study. We are interested in aspects of the ground state, such as the spin structure, of the Anderson Hamiltonian in hole-doped monolayer TMDs. In particular, we are interested in the possibility of tuning the properties of the many-body Kondo bound state by application of circularly polarized light. This is possible, in principle, because of the topological nature of the low-lying states in monolayer TMDs which allows for optical transitions between two bands of d character and which endows the transition rates with strong valley-selectivity with circular polarization [29]. To capture the main point, we depart from the picture of Sec. 3.3.3 and consider only the upper valence bands which actually cross the chemical potential. These bands are identical in form but have opposite spin and live in opposite valleys in momentum space. As stated in the previous, valley-selectivity translates to spin-selectivity so one may imagine

that the steady-state system created by application of light forms a Fermi sea with unequal chemical potentials for spin up/down; this effective difference in chemical potentials is now denoted δ, and the midpoint of the potentials μ. In terms of the previous section, the scale is $\delta \sim \delta_\nu$ and the chemical potential top is raised slightly (so that the new midpoint is at the top). We use $\delta > 0$ for higher spin up occupation, i.e. the excitative circular polarization is given by $\nu = -\mathrm{sgn}\,(\delta)$.

Below, we describe the usual projection of the initial problem onto a semi-infinite linear chain with nearest-neighbor hoppings and the impurity situated at the end. Next, we describe how interesting quantities are calculated; the total spin J^2 is difficult to obtain within NRG, particularly for our spin-split system, so the critical quantities include entropy, spin J_z, and the impurity spectral functions. Results for the unexcited (zero offset) case are presented alongside the initial definitions, whereas those for the excited case are presented in the final part of this section. Numerical parameters are set to match the conditions of the variational state from the previous section, with specifics stated prior to the results for the excited case, Sec. 3.4.5.

3.4.1 Generic Setup

To begin with, we use a simplified model considering only the valence bands that cross the chemical potential, taking the lower spin-split bands to be completely filled and inert. This simplified picture is most applicable when the spin-splitting is largest, so the most appropriate materials are WSe_2 and WS_2. To begin with, we modify the Anderson Hamiltonian

by using $n_{f,s}\left(n_{f,s}-1\right)=0$ [39],

$$
\begin{aligned}
H' &= H-\sum_{s=\uparrow,\downarrow}\mu_s N_s && (3.31)\\
&= \sum_{\mathbf{k},s}\left[\left(E_k-\mu_s\right)c^\dagger_{\mathbf{k},s}c_{\mathbf{k},s}+\left(v^\alpha_{\mathbf{k}}c^\dagger_{\mathbf{k},s}f_s+h.c.\right)\right]+\sum_s\left(\varepsilon_0-\mu_s\right)f^\dagger_s f_s+Un_{f,\uparrow}n_{f,\downarrow} && (3.32)\\
&= H_m+H_V^\alpha+\sum_s\left(\varepsilon_0-\mu_s+\frac{U}{2}\right)f^\dagger_s f_s+\frac{U}{2}\left(\sum_s n_{f,s}-1\right)^2-\frac{U}{2} && (3.33)
\end{aligned}
$$

where the number operators are $N_s=n_{f,s}+\sum_{\mathbf{k}}c^\dagger_{\mathbf{k},s}c_{\mathbf{k},s}$, and H_m and H_V^α are the material (TMD) and hybridization Hamiltonians as in (3.5) and (3.13), respectively. The remaining terms (aside from $U/2$) are now collected to form H_{imp}. The chemical potentials are $\mu_s=\mu+s\delta/2$ so that the difference is δ. The low-energy model leading to H_m is only valid within a cutoff, $|E_k|<\Lambda$ of the order of the gap Δ. Offsetting about the hole doped chemical potential, we set $D=\Lambda+\mu$ as the effective cutoff and we note the top of the band $e_0=E(0)-\mu$ so that $-D<E(k)-\mu<e_0$.

As in the previous sections, we use the most basic form of hybridization with the impurity sharing a metal (i.e. W, Mo) site with type $\alpha=1$ or 2 orbital. The operators appearing in H_m and H_V^α above refer only to the upper valence band, with labels $n=-$ and $\tau=s$.

Moving out of discrete $\mathbf{k}$-space, we construct effective states labeled with energy ε relative to the chemical potentials. Specifically, we use the quasi-angular momentum (QAM) operators as in Eq. (3.14); to complete the transformation to energy one simply uses the density of states $g(\varepsilon)$. In doing so we are moving to continuous space, and we concentrate on the states hybridizing with the impurity, i.e. those with QAM $m=0$ for type I or $m=-\tau$ for type II. The remaining states, those with QAM labels not appearing

in H_V^α, are treated as inert just like the lower valence bands — all such states are ignored here as they will not be affected by the presence of the impurity. Once in continuous energy space we rescale to the dimensionless variable $\xi = \varepsilon/D$. After the above steps, we have a new Hamiltonian

$$\begin{aligned} \frac{H'}{D} &= \sum_s \int_{-\ell_s}^{e_s} d\xi \left[\xi\, c^\dagger_{\xi,s} c_{\xi,s} + \sqrt{\frac{\Gamma}{\pi D}} \left(c^\dagger_{\xi,s} f_s + h.c. \right) \right] \\ &+ \frac{1}{D} \sum_s \left(\varepsilon_{0,s} + \frac{U}{2} \right) n_{f,s} + \frac{U}{2D} \left(\sum_s n_{f,s} - 1 \right)^2 \end{aligned} \tag{3.34}$$

where we have the bottom/top of the rescaled bands $\ell_s = 1 + s\delta/2D$ and $e_s = e_0/D - s\delta/2D$, effective impurity levels $\varepsilon_{0,s} = \varepsilon_0 - s\delta/2$, and half-width $\Gamma = \pi g(\mu)|v_\mu^\alpha|^2$ (the type label α is dropped). The terms on the second line form H_{imp}/D. The new Hamiltonian is a recasted duplicate of (3.33); it is an exact transformation for the upper valence band only TMD model under consideration (other than the irrelevant constant $U/2$ and inert states).

Proceeding, we make our first approximation: we re-discretize energy space into logarithmic intervals approaching each chemical potential[2]. The reason for this step is to catch the logarithmic divergences that are expected at low temperatures — each interval will contribute an equal amount to integrals like $\int_{-1}^{-k_BT/D} d\xi/\xi$. Specifically, one chooses intervals at positive and negative 'energy' labeled by $n = 0, 1, 2, ...$ approaching zero[39]

$$e_s R^{-(n+1)} < \xi < e_s R^{-n} \tag{3.35}$$

$$-\ell_s R^{-n} < \xi < -\ell_s R^{-(n+1)} \tag{3.36}$$

where $R > 1$ is the discretization parameter[3]. The continuous limit is obtained by taking $R \to 1$, although it is established that the approximation works well for up to $R = 3$. With

[2]See Appendix D for details on this and the following transformations.

[3]The notation here is different from that of Ref.s [39, 41] and others since we have already used their symbol, Λ, for the model energy cutoff.

positive/negative energy operators $a_{n,s}$ and $b_{n,s}$ corresponding to the left/right of (3.36), respectively, we can write an approximate version of the Hamiltonian:

$$\frac{H'}{D} \approx \frac{1+R^{-1}}{2} \sum_{n,s} \left(e_s R^{-n} a^\dagger_{n,s} a_{n,s} - \ell_s R^{-n} b^\dagger_{n,s} b_{n,s} \right) + \frac{H_V}{D} + \frac{H_{imp}}{D}. \tag{3.37}$$

We now have the band (bath) operators appropriately discretized to focus on states near the chemical potentials and that part of the Hamiltonian is diagonal, but the interaction with the impurity involves a different state:

$$\begin{aligned} \int_{-\ell_s}^{e_s} d\xi \, c^\dagger_{\xi,s} &= \sum_n \sqrt{\frac{1-R^{-1}}{R^n}} \left[(e_s)^{1/2} a^\dagger_{n,s} + (\ell_s)^{1/2} b^\dagger_{n,s} \right] & (3.38) \\ &\equiv (1+e_0/D)^{1/2} \, d^\dagger_{0,s}. & (3.39) \end{aligned}$$

The state created by $d^\dagger_{0,s}$ is interpreted as the zeroth site of a semi-infinite chain, which has the impurity coupled to it. To construct operators $d^\dagger_{m,s}$ for the remaining sites $m = 0, 1, 2, ...$ the Lanczos procedure is used[34, 41, 66]. Note that since the bath part of (3.37) is diagonal, it will necessarily become non-diagonal when transformed to the new basis; the goal of the Lanczos procedure is to create states orthogonal to the $m = 0$ state (3.39) such that the Hamiltonian is as close to diagonal as possible, i.e. with only nearest-neighbor hoppings. Skipping to the result (see Appendix D.2 for details),

$$\begin{aligned} \frac{H'}{D} &\approx \sum_{m=0}^{\infty} \sum_s \left(\epsilon_{m,s} d^\dagger_{m,s} d_{m,s} + t_{m,s} \left(d^\dagger_{m+1,s} d_{m,s} + h.c. \right) \right) \\ &+ \sqrt{\frac{\Gamma(1+e_0/D)}{\pi D}} \sum_s \left(d^\dagger_{0,s} f_s + h.c. \right) + \frac{H_{imp}}{D} \end{aligned} \tag{3.40}$$

where the site energies/hoppings $\epsilon_{m,s}$ and $t_{m,s}$ must generally be determined numerically.

From here, we must consider how to handle the still-infinite number of degrees of freedom. In the following we describe the main NRG iterative diagonalization procedure, and later we get corresponding physical quantities.

3.4.2 Iterative Diagonalization

The starting point of this section is the semi-infinite chain Hamiltonian (3.40). Since we cannot handle an infinite number of sites, we consider breaking the chain off at some site M. Previous experience tells us that hoppings scale as $R^{-m/2}$, so we rescale the Hamiltonian by something $\propto R^{M/2}$ to make each new site enter the system with order unity[38, 39]. Specifically, we write

$$\begin{aligned}\overline{H}_M &= \frac{2}{1+R^{-1}} R^{(M-1)/2} \left[\sum_s \left(\sum_{m=0}^{M} \epsilon_{m,s} d^\dagger_{m,s} d_{m,s} + \sum_{m=0}^{M-1} t_{m,s} \left(d^\dagger_{m+1,s} d_{m,s} + h.c. \right) \right) \right. \\ &+ \left. \widetilde{\Gamma}^{1/2} \sum_s \left(d^\dagger_{0,s} f_s + h.c. \right) + \sum_s \widetilde{\delta}_{f,s} n_{f,s} + \widetilde{U} \left(\sum_s n_{f,s} - 1 \right)^2 \right] \end{aligned} \tag{3.41}$$

where $\widetilde{\Gamma} = \Gamma(1 + e_0/D)/\pi D$, $\widetilde{\delta}_{f,s} = (\varepsilon_{0,s} + U/2)/D$, and $\widetilde{U} = U/2D$. Now, the semi-infinite Hamiltonian is recovered with

$$\frac{H'}{D} = \lim_{M \to \infty} \left[\frac{1+R^{-1}}{2} R^{-(M-1)/2} \overline{H}_M \right]. \tag{3.42}$$

Furthermore, we can write a simple recursion relation to build the $M+1$ Hamiltonian from the previous:

$$\overline{H}_{M+1} = R^{1/2} \overline{H}_M + \frac{2\, R^{M/2}}{1+R^{-1}} \sum_s \left(\epsilon_{M+1,s} d^\dagger_{M+1,s} d_{M+1,s} + t_{M,s} \left(d^\dagger_{M+1,s} d_{M,s} + h.c. \right) \right). \tag{3.43}$$

Rather than go into details, like building each Hilbert space (see for example Ref.s [39, 66]), we simply remark on the general methodology of the iterative procedure. One begins with the simplest chain consisting only of the impurity and the zeroth chain site coupled to it ($\overline{H}_0$) and the system is numerically diagonalized in Fock space, broken down by subspaces. To label the subspaces, one notes that the number of spin up/down

is conserved; the operators $N_s = n_{f,s} + \sum_m d^\dagger_{m,s} d_{m,s}$ commute with the Hamiltonian. For convenience, one chooses the subspace labels of 'charge' $Q = \sum_s N_s - (M+2)$ and spin $J_z = (1/2)(N_\uparrow - N_\downarrow)$.

Once the initial $M = 0$ Hamiltonian is diagonalized in each subspace, the $M = 1$ Hamiltonian is constructed by extending the previous eigenspace to include the new site and using Eq. (3.43). The only problem with this approach is that the Hilbert space grows by a factor of 4 with each additional site; the total number of states to describe up to site M is 4^{M+2}, since each site has spin up/down slots which can be either empty or filled. To deal with this, one chooses some number of states to keep and throws out everything above the energy of the last state (keeping degenerate states). The number of states one must keep is related to the choice of discretization parameter $R > 1$; approaching unity is the same as approaching continuity so one must keep a larger number of states to describe the system accurately. Typically, a choice of $R = 3$ requires about 400 states whereas $R = 2.5$ requires 600 or more. The rate of convergence is also influenced by R (larger is faster), so for the sake of time and memory usage we choose $R = 3$ and 400-425 states[4].

With the truncation step, the number of states is always numerically manageable so one can repeat the steps of diagonalization, truncation, and Hamiltonian construction until a sufficiently large site M is reached. How large do we need? Again, it depends on the size of R — the larger the value, the faster the procedure converges, leading to fewer required iterations/sites. Generally one must iterate until the system has stabilized, as revealed particularly by vanishing differences in the energy spectrum in going from M to $M + 2$. Also, one must note that finite-size effects create oscillations in various results for

[4]See Appendix D.3 for demonstrations of convergence.

even/odd total sites; for thermodynamic results (next) we will interpolate and average the even/odd curves to get a better curve for the system. To do even better, one could employ a z-averaging technique to use fast computations with $R = 4 - 10$ and obtain properly averaged results[41], however this would require the numerical Lanczos procedure to be repeated at each z and we really only require accurate qualitative results, so the simple even/odd average should be sufficient.

3.4.3 Thermodynamics

Now that we have built a reliable way of solving the finite systems of any size (within reason), we can use the information to extract thermodynamic and other quantities. First we note that, because of the rescaled form (3.42), we must be careful about calculating the partition function and thermodynamic averages. The appropriate form of the partition function is

$$Z(T) = \mathrm{Tr}\, \exp\left(-\beta H'\right) = \lim_{M\to\infty} \mathrm{Tr}\, \exp\left(-\overline{\beta}_M \overline{H}_M\right) \tag{3.44}$$

$$\equiv \lim_{M\to\infty} Z_M(T) \tag{3.45}$$

where $\beta = 1/k_B T$ is the usual inverse temperature while $\overline{\beta}_M = ((1+R^{-1})/2)R^{-(M-1)/2} D/k_B T$ is a rescaled dimensionless version. Since the states are actually truncated, each step introduces an error in calculated states and higher energies should be neglected by choosing a lower temperature. Denoting the maximum energy scale of the finite system $K(R)$, the replacement of Z by Z_M is a good approximation provided that [41]

$$1/K(R) \ll \overline{\beta}_M \ll R. \tag{3.46}$$

Choosing $R = 3$ one has $K(R) \sim 10$, so a good choice is to fix $\overline{\beta}_M = 1/2$ so that the condition is satisfied with $0.1 \ll 0.5 \ll 3$. In this case, we are effectively considering a set of temperatures which are decreasing exponentially with the number of sites M included: $k_B T_M/D = (1 + R^{-1})R^{-(M-1)/2}$.

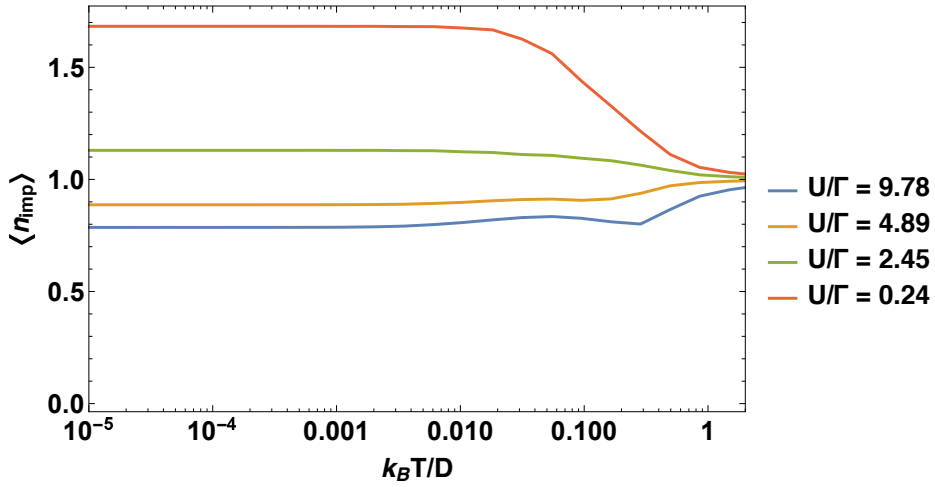


Figure 3.5: Impurity occupation in the unexcited case, $\delta = 0$, for several choices of U at fixed Γ (see Sec. 3.4.5 for parameter details). The occupation is diminished or enhanced from 1 due to the asymmetry of the impurity level about the chemical potential.

Next, we simply write some of the quantities of interest to us. Impurity properties are the main focus, so first we consider the average occupation of each spin

$$\langle n_{f,s} \rangle = \mathrm{Tr}\left[n_{f,s} \exp\left(-\overline{\beta}_M \overline{H}_M\right)\right] / Z_M = \sum_q \langle q | \, n_{f,s} \, | q \rangle \exp\left(-\overline{\beta}_M \overline{E}_q\right) / Z_M \tag{3.47}$$

where we have introduced eigenstates $|q\rangle$ with energies $\overline{E}_q$ (in the space up to site M). In order to calculate such objects, one must keep track of the matrix elements $\langle q | \, n_{f,s} \, | q \rangle$ projected to the eigenspace the each successively longer chain. With matrix elements and energies in hand, quantities like (3.47) are straightforward to calculate, giving impurity occupation and spin values $\langle n_f \rangle = \sum_s \langle n_{f,s} \rangle$ and $\langle s_z \rangle = (\langle n_{f,\uparrow} \rangle - \langle n_{f,\downarrow} \rangle)/2$. To display the

typical behavior in our case, we show in Fig. 3.5 the impurity occupation for WSe_2 with equal chemical potentials (the spin is omitted because it is identically zero in this case).

Since the system is broken down to 'charge' Q and total spin J_z subspaces, their averages are very simple to obtain — sums like (3.47) are calculated in each subspace (each with fixed Q, J_z), which are then totaled. The same can be done for powers, e.g. J_z^2.

To assess the nature of the low-temperature system, i.e. the formation of a bound singlet state, we are also interested in the impurity contributions to entropy and susceptibility. To calculate those we actually find the results for the system as a whole, then subtract the part arising from the band (bath) alone without the impurity [38, 66]:

$$S_{imp} = S_{total} - S_b \; ; \; \chi_{imp} = \chi_{total} - \chi_b. \tag{3.48}$$

To compare the spin J_z to the variational results, one would also like to subtract the spin of the chain without the impurity $\langle J_z \rangle - \langle J_z \rangle_b$ but we find that the same quantity is accurately given by the impurity spin $\langle s_z \rangle$ as one might expect.

Also, we wish to avoid derivatives of the free energy (to minimize numerical errors) so we use the alternative form of entropy

$$S_{total}/k_B = \beta \langle H' \rangle + \ln Z = \overline{\beta}_M \langle \overline{H}_M \rangle + \ln Z_M \tag{3.49}$$

where the average energy is very simply $\langle \overline{H}_M \rangle = \sum_q \overline{E}_q \exp\left(-\overline{\beta}_M \overline{E}_q\right)/Z_M$. For the susceptibility, we use the fluctuation-dissipation theorem to write

$$\chi_{total}/(g\mu_B)^2 = \beta \left(\langle J_z^2 \rangle - \langle J_z \rangle^2 \right). \tag{3.50}$$

As stated above, the impurity contributions are found by subtracting the values arising from the system with no impurity site. One may calculate those pure-chain values by hand,

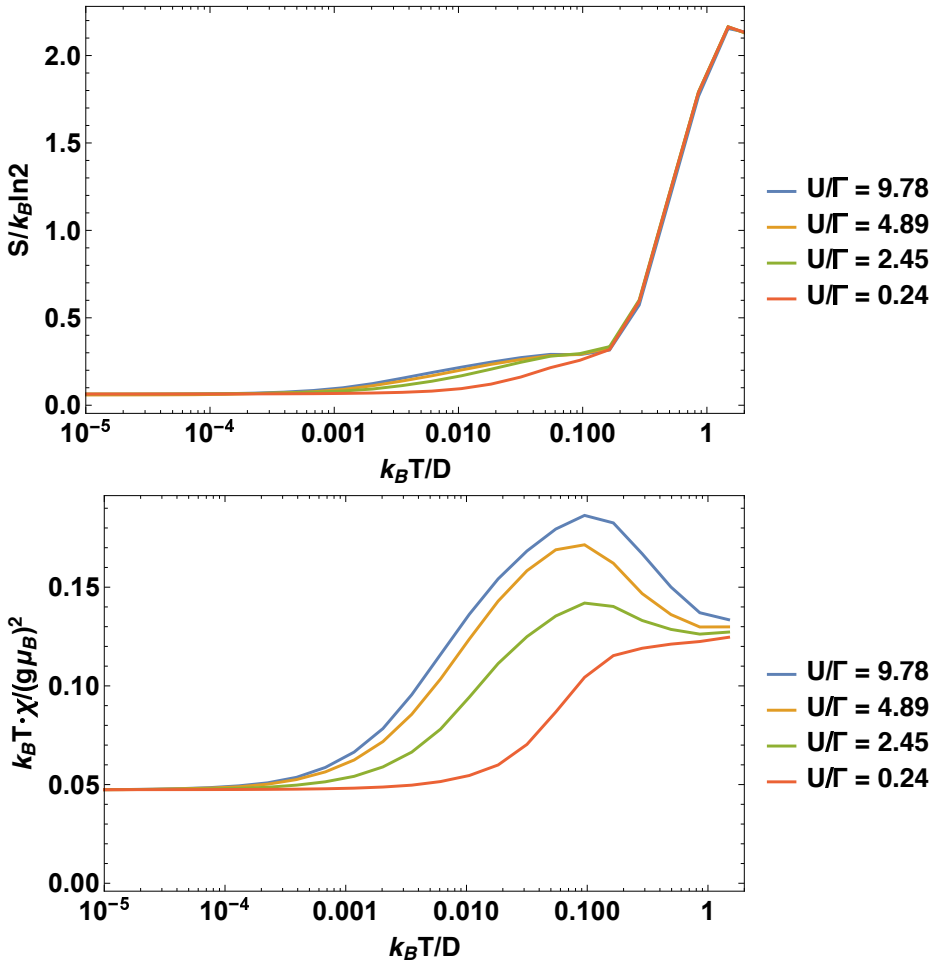


Figure 3.6: Impurity entropy (top) measured in units of $k_B \ln 2$ and susceptibility (bottom) in units of $(g\mu_B)^2/k_B T$, in the unexcited case. The trends are typical (as in fig. 6 of Ref. [41]), except for the asymptotic value of susceptibility.

but for numerical consistency we choose to run a separate NRG procedure for the chain without the impurity. Results in Fig. 3.6 for the unexcited case of WSe_2 reveal rather typical behavior for the Anderson model within NRG, except that we have a nonzero value of $T\chi$ as $T \to 0$ revealing the persistence of a local moment.

In addition to providing information about the formation or persistence of a local moment, we can follow Wilson[38] to obtain the Kondo temperature scale from the shape of

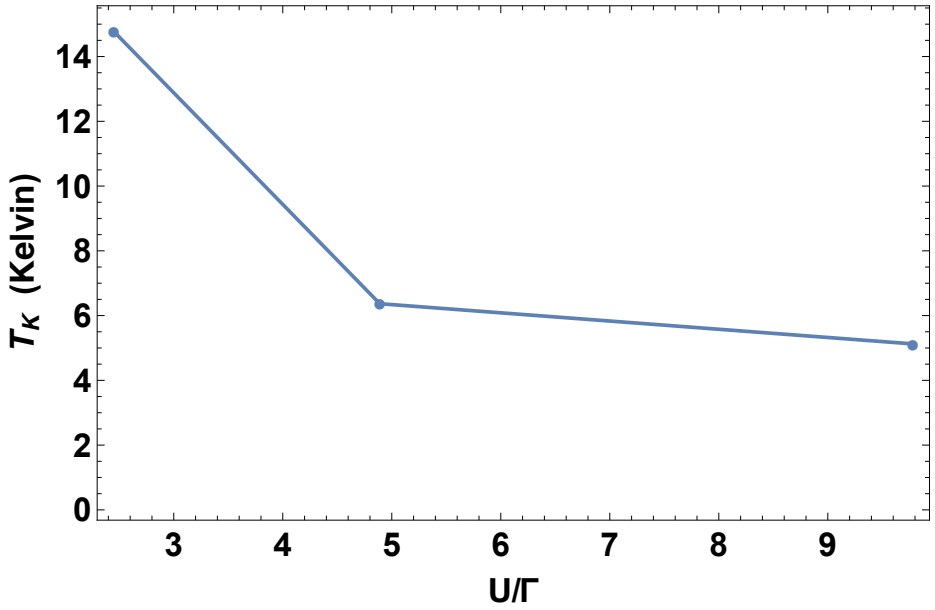


Figure 3.7: The Kondo temperature as given by Wilson's relation for the unexcited case of WSe_2 at a few U/Γ. The trend of increasing T_K at decreasing U/Γ is due to the proximity to the strong-coupling fixed point in parameter space.

the susceptibility curve; T_K is the temperature at which $k_B T\chi/(g\mu_B)^2 = 0.17/3 \approx 0.0567$. We show in Fig. 3.7 the temperature obtained in this way for a few values of U/Γ in the unexcited case.

One way to explain the increasing temperature with decreasing U is to recall NRG flow diagrams (as in fig. 8 of Ref. [39]) which reveal the fixed points and their stability. The final configuration for basically any starting point is the strong-coupling ($U \to 0, \Gamma \to \infty$) fixed point, at which the impurity is fully bound. For small U/Γ, a local moment is never formed (i.e. the flow stays away from the local moment fixed point) and the impurity is easily bound so the Kondo temperature is higher. On the other hand, large U/Γ places the system very near to the local moment fixed point so that the flow initially gives a local moment, and only after more iterations does the system begin to approach the strong-

coupling fixed point, so the Kondo temperature is lower. This point is not just useful for the temperature scale; the same description from the flow diagram also nicely explains the susceptibility and how it changes with various U/Γ as seen in Fig. 3.6, the presence and size of the bump at moderate temperatures revealing the formation of a local moment.

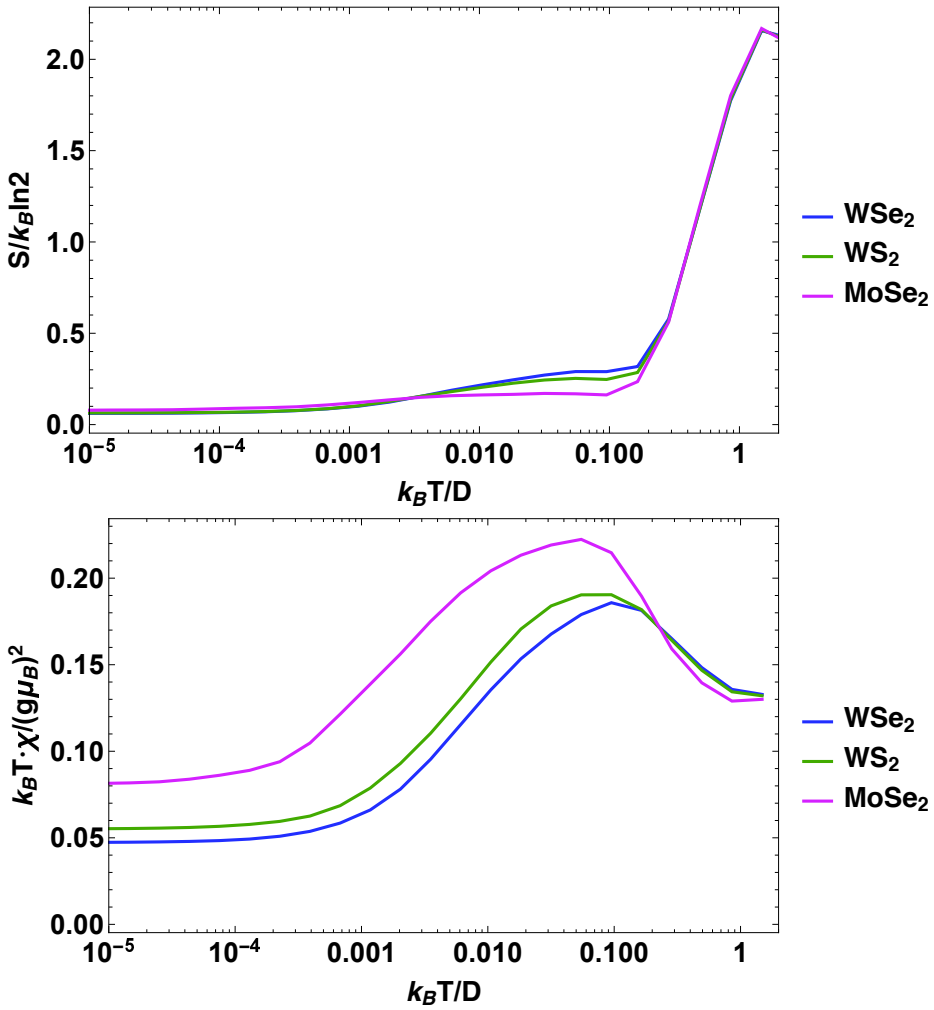


Figure 3.8: Impurity entropy (top) measured and susceptibility (bottom) for three monolayer TMD materials. They are all in the unexcited case, and with fixed $U/\Gamma = 9$. The trends are explained in the same way as for Fig. 3.6.

To compare across materials, we present in Fig. 3.8 the entropy and susceptibility

for three TMDs (recall MoS_2 is excluded). One can see that, despite the constant ratio $U/\Gamma = 9$, the materials look like they have local moment regimes of varying intensity. This is actually due to the topological content captured by the Bloch angles appearing in the effective coupling to the impurity, i.e. the $w = \sin(\theta_\mu/2)$ of (3.13) and (3.14). The angle θ approaches zero as the chemical potential approaches the lower valence band top, the distance from which given by the magnitude of the spin-orbit coupling λ. Thus the tungsten compounds with larger λ start off with larger Γ and their NRG trajectories form relatively weaker local moments, quickly going to the strong-coupling fixed point. On the other hand, $MoSe_2$ has the smallest spin splitting and hence the smalleset deviation of the Bloch angle from the pole so its NRG trajectory begins close to the free orbital fixed point ($U = \Gamma = 0$), leading quickly to a strong local moment and very slowly to the strong-coupling point. This pattern among the three materials and the explanation related to the Bloch angles is consistent with the discussion in Sec. 3.3.1, following Eq. (3.22).

3.4.4 Spectral Function

Next we turn to the impurity spectral function. The $T = 0$ spectral function is given by [42, 66]

$$A_s(\omega) = \frac{1}{Z(0)} \sum_q \left[|\langle q| f_s |0\rangle|^2 \, \delta\left(\omega + (E_q - E_0)\right) + |\langle 0| f_s |q\rangle|^2 \, \delta\left(\omega - (E_q - E_0)\right) \right] \quad (3.51)$$

where the energies E_q are referring back to the full system H' as in (3.40). We are primarily interested in ground-state properties so we use the $T = 0$ spectral function only, in which only states differing from the ground state by one particle and one unit of spin appear: $|Q_q - Q_0| = 1$ and $|J_{z,q} - J_{z,0}| = 1/2$. If one is interested in the spectral function for $T \neq 0$

then one must consider combinations between *all* states with such differences in Q and J_z, and the following construction becomes much more involved[42].

In order to construct a spectral function within NRG, one must obviously keep track of matrix elements of impurity operators f_s projected to the eigenspace of each successive chain. Additionally, the energy range must be restricted for each M since each iteration reduces the energy window in which results are accurate. The restriction cuts off the low energies which are yet to be obtained from larger M and cuts out the high energies which are already accurately described from previous M. Setting $\omega_M = ((1+R^{-1})/2)R^{-(M-1)/2} = \overline{\beta}_M/(D\beta)$, the ranges are roughly $\omega_M < |\omega| < K(R)\omega_M$.

Furthermore, the energy ranges for different M will overlap and one must properly combine the spectral function aplitudes without double counting and while maintaining the accuracy of low-energy states. There is a well-defined method for this purpose [42], which is described as follows. Consider chains M and $M+2$ (recall that even and odd are separated due to finite size effects): the overlap region will involve the higher energies from $M+2$ and the lower energies from M. Since its accuracy is at lower energy, the $M+2$ spectral function is weighted in the overlap region with a linear distribution going from one down to zero towards higher energy. Conversely, the M spectral function is also weighted in the overlap region but its line is zero at the lower end and rises to one in joining with the values at yet higher energy. After adding the weighted M and $M+2$ spectral functions, we have a description over a larger energy range with appropriate emphasis and without double counting (the sum of the linear distributions is unity). One can thus build a total spectral function covering the full energy range by adding all even/odd functions as described up to

some maximum chain length. Still, one will observe some difference between the even and odd functions. To complete the total function the even and odd results are simply averaged, $A = (A^{even} + A^{odd})/2$.

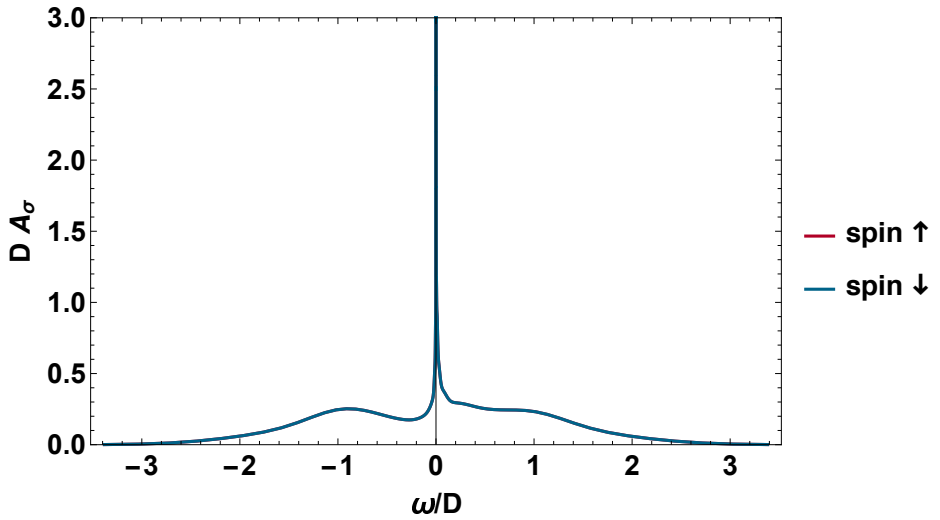


Figure 3.9: Impurity spectral functions for the unexcited case, with fixed $U/\Gamma \approx 4.9$. The spin up/down results overlap due to preserved time-reversal. They are consistent with conventional models[34], as expected from the metal-like structure of our model and choice of parameters.

As a final step, we must have some way to interpret the δ-peaks appearing in (3.51). There are many different options for broadening functions; here we replace the peaks with Gaussians

$$\delta(x) \to \frac{1}{\sqrt{\pi\eta_M^2}} \exp\left(-x^2/\eta_M^2\right) \tag{3.52}$$

where the widths are $\eta_M \approx \omega_M$. This final step gives final, accurate, and smooth spectral functions for the impurity. When plotting these, because of the exponentially decreasing widths, it is beneficial to sample the energies logarithmically so that most sample points lie near $\omega = 0$. The above construction leads to final spectral functions, representatives shown in Fig. 3.9 for our case with equal chemical potentials in WSe_2.

It is worth noting here the way to check the accuracy of the above construction. The spectral function should obey the Friedel sum rule, $\int_{-\infty}^{0} A_s(\omega)\, d\omega = \langle n_{f,s} \rangle$, with the occupations $\langle n_{f,s} \rangle$ given by Eq. (3.47). It is well documented that the conventional construction above works well on a qualitative level but may disobey the rule quantitatively; typically the difference is quite small (a few percent) for models with time-reversal symmetry, but it can be very significant ($\sim 20\%$) when a magnetic field or other spin dependence is introduced (see fig. 10 of Ref. [41]). This quantitative discrepency can be remedied by using a reduced density matrix method for calculating the spectral function, which enforces the Friedel sum rule by construction, but the overall shape and behavior is unchanged so we stick to the simpler conventional method here.

3.4.5 Numerical Results

Recall that in our model system we can have slightly different chemical potentials in the two valleys due to optical excitation, and with spin-splitting and time-reversal this implies effectively spin-dependent chemical poentials. The effective difference is denoted $\delta = \mu_\uparrow - \mu_\downarrow$, and the midpoint of the potentials is $\mu = (\mu_\uparrow + \mu_\downarrow)/2$.

For the numerical results we would like to compare as closely as possible to the variational case, we take $\mu = -\Delta/2$ (midway between the spin-spit valence bands) and include several cases $\delta = 0$, $\delta = \pm\lambda/10$, and $\delta = \pm\lambda/5$ (see Eq. (3.1) for a reminder of the band parameters). As in the variational section we take the impurity to be slightly below the chemical potential $\varepsilon_0 = -\Delta/20$, placing the model in a "mixed-valence" regime[34]. Note that we should have $\delta/2 < |\varepsilon_0|$ to make sure that the impurity level is still below both chemical potentials; the largest splitting parameter is $\lambda \sim \Delta/6$ so the condition is

satisfied with $1/60 < 1/20$. Also, using an absolute cutoff energy scale $\Lambda = \Delta$, the effective cutoff relative to μ is $D = \Delta/2$. To make sure we can comfortably neglect the hybridization of the lower (filled) valence bands, we choose for now the material with the largest spin-splitting: WSe_2. For the width Γ we need the hybridization strength so we set $V_1 = t/2$ for type $\alpha = 1$ coupling, i.e. half of the hopping energy associated with the TMD, leading to $\Gamma/D \approx 0.051$. Lastly, we allow the Coulomb repulsion U to vary but we fix it at a benchmark value $U = \Delta/8 = D/4$, giving $U/\Gamma \approx 4.9$, unless otherwise stated.

Before jumping to the results, we recall a vital difference between this case and other asymmetrical cases. A typical "asymmetrical" model[40] has the impurity level set away from $-U/2$ so that the impurity term of (3.41) has $\widetilde{\delta} \neq 0$, but the band is kept symmetric, i.e. the energy is on the interval $[-D, D]$. Here, we have $\widetilde{\delta} \neq 0$ (and spin-dependent in the excited case) but we also have the chemical potential close to the band top so that our energy interval is $[-D, e_0]$ with $e_0 < D$, making our model have site energies $\epsilon_m \neq 0$ as well.

We begin the presentation of results for the excited case, with chemical potential offset $\delta \neq 0$, with thermodynamic quantities. To deal with oscillations between even/odd chain length M, due to finite-size effects, we find separate interpolation functions and take the average. We consider four values of δ, a pair of equally spaced values $\delta/\lambda = 1/10\,, 1/5$ and their negative counterparts, along with the zero offset values from the previous section. The choice allows for a rough idea of how various quantities vary with the offset δ while still keeping both chemical potentials above the impurity level.

The entropy and susceptibility, Fig. 3.10, show little difference compared to those

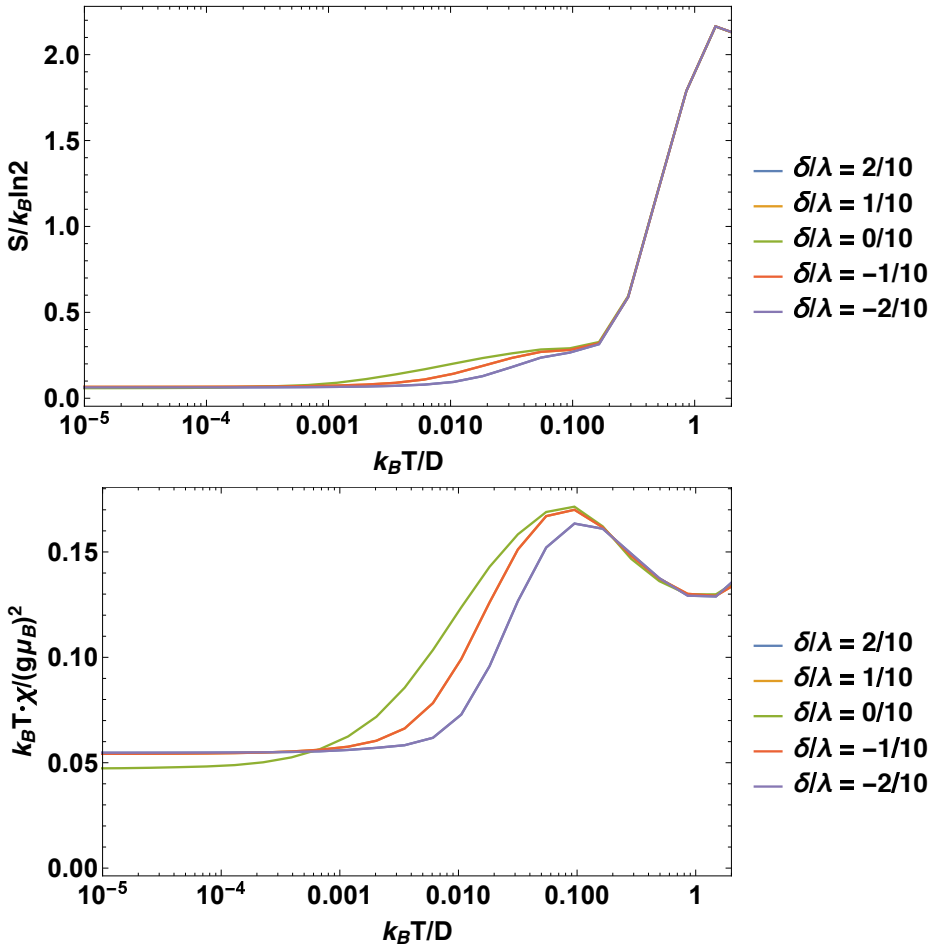


Figure 3.10: Impurity entropy and susceptibility in the excited system for various offset δ. The numerical values are as described at the beginning of this section. The rightward evolution reveals increasing T_K.

of the previous Fig. 3.6. The susceptibility lands higher as the temperature is decreased, corresponding to a larger moment surviving at $T = 0$. Also, both suggest an increasing T_K with δ since the asymptotic values are approached more quickly; indeed that is what we observe in Fig. 3.11. The reason for the larger moment is obvious, but the larger Kondo temperature may not be so obvious. Apparently, due to the difference in energies for spin up/down, the system is rapidly pushed in the direction of the inevitable moment and T_K

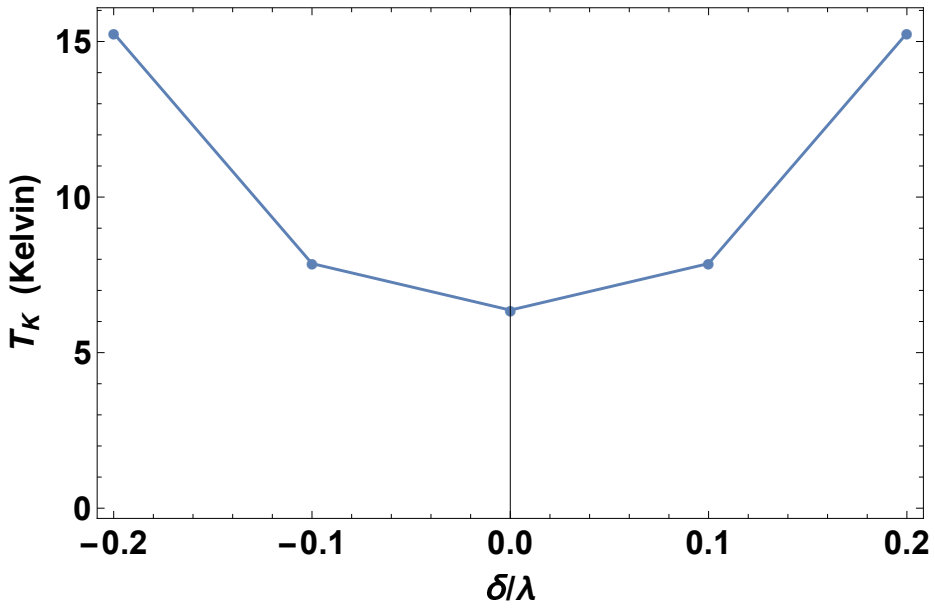


Figure 3.11: The Kondo temperature in the excited case at a few δ. The increasing values away from $\delta = 0$ suggest effectively larger Γ with increasing magnitude of δ, pushing the starting point closer to the strong-coupling fixed point.

is increased.

Examining impurity properties further, the occupation $\langle n_f \rangle \equiv \langle n_{imp} \rangle$ and spin $\langle s_z \rangle$ are presented in Fig. 3.12. Recall that the impurity spin $\langle s_z \rangle$ here is essentially the same quantity as the difference $\langle J_{z,val} \rangle^{ex} - \langle J_{z,val} \rangle_0^{ex}$ from the above variational results, Sec. 3.3.3, which was identically zero there even with a nonzero offset. Here, we see a more expected result: the spin is polarized overall with sign and magnitude reflecting the difference δ. As for the occupation, the value is increased because one of the impurity levels (up or down) is effectively deeper below its chemical potential, increasing the occupation of that spin, while the other is shallower but still remains below, preventing its value from decreasing too much. One may also be interested in the bump at moderate temperatures which shrinks with increasing δ; it aligns closely with the bump in susceptibility which marks the point

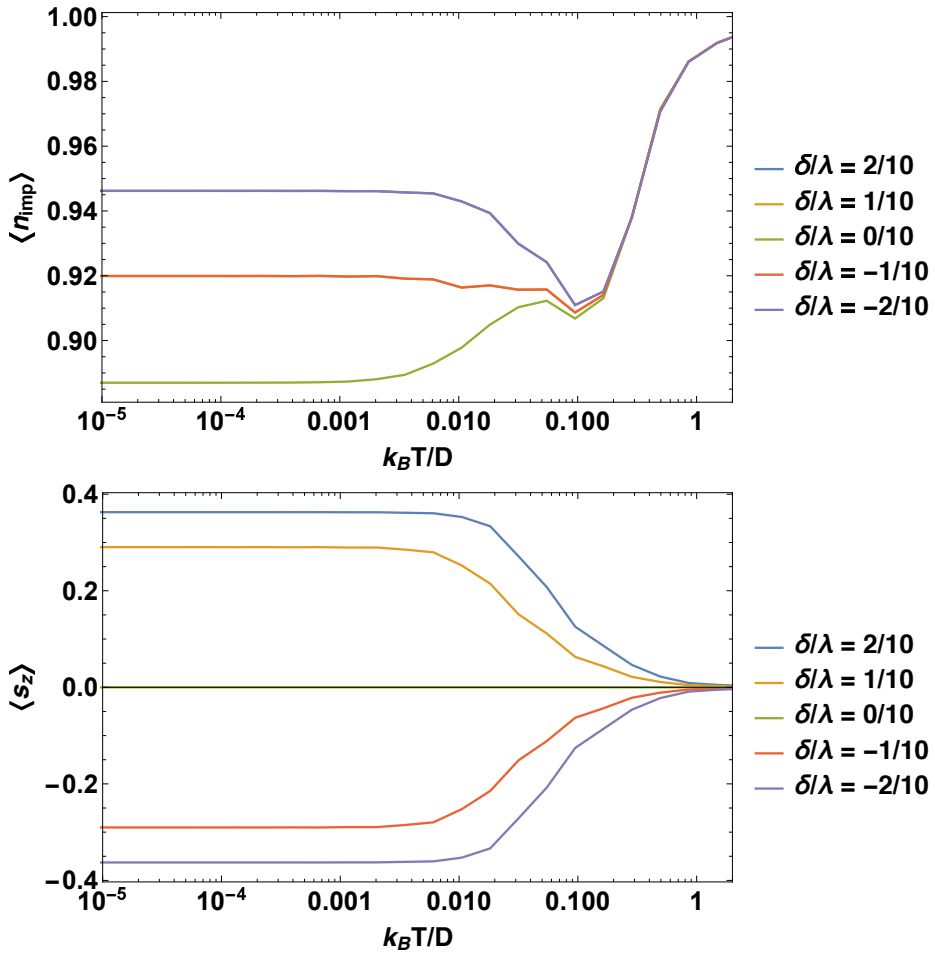


Figure 3.12: Impurity occupation (top) and spin (bottom). The nonzero offset polarizes the spin as expected. The occupation is increased with larger δ because one chemical potential becomes more distant from the impurity level.

at which the system begins to depart the local moment neighborhood and heads toward the strong-coupling fixed point. Similarly, the average occupation will drop as the local moment is formed since double occupation is not present there (the effective U/Γ becomes very large), while the approach to strong-coupling allows for a growth of occupation (now $U/\Gamma \to 0$) if the effective depth of the impurity is large enough.

To better understand the spin at $T = 0$, we show in Fig. 3.13 the impurity spin

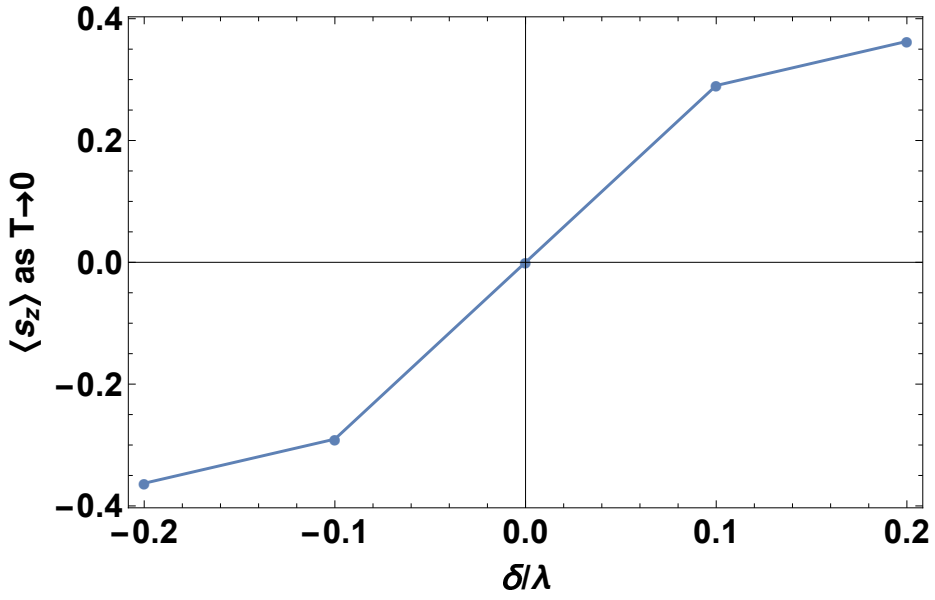


Figure 3.13: The impurity spin at $T \approx 0$ shows some familiar dependence on δ. This result is equivalent to the shift in total spin $J_{z,val}$ from the variational calculation, revealing a sharp contrast between the results.

at the lowest available temperature plotted against the offset δ. Our offset choice results in only five points total, but the trend is reminiscent of the familiar hyperbolic tangent for a paramagnetic system with δ playing the role of magnetic field. The big point here, however, is that the impurity spin (and hence the shift of the total spin) varies monotonically with the offset, in contrast to the corresponding variational results.

Finally, we come to the spectral functions for the excited case. A representative with both spins together is shown in Fig. 3.14. As stated during the construction of the spectral function, the spin polarization is typically under-approximated unless one employs reduced density matrices, but the qualitative spin polarization is very clear. The spin up chemical potential is higher for $\delta > 0$ leading to an effectively deeper impurity level; the resultant increase in occupation appears as a more pronounced bump in $A_\uparrow(\omega)$ at negative

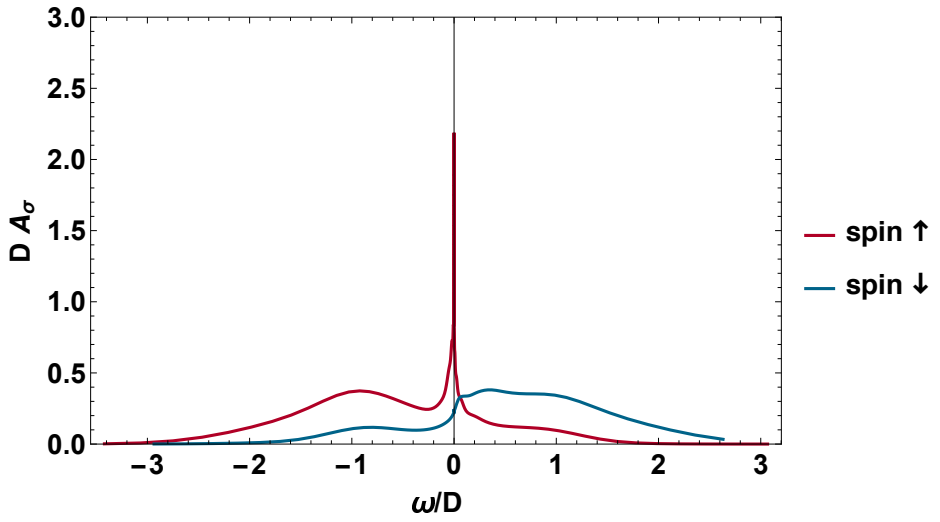


Figure 3.14: Impurity spectral functions for the excited model at $\delta/\lambda = 1/5$. The qualitative form is consistent with expectation, and is distinct from the variational result. The Friedel sum rule is satisfied within $\sim 20\%$.

ω, alongside a very diminished amplitude for positive ω. We see that the impurity is tightly bound for spin up, but almost completely unbound for spin down, in qualitative agreement with the large impurity spin seen in Fig. 3.12. This behavior is suggested by the variational result, although here the spin difference is much more significant and it does not get cancelled out by a counter-reaction from the band (bath) electrons.

One may like to view the spectral functions together for all the chosen offsets. For clarity, in Fig. 3.15 we plot the spin up/down functions separately, side by side, and we make the figures as large as possible. It is very clear that the pattern is repeated as expected for all the given offsets δ.

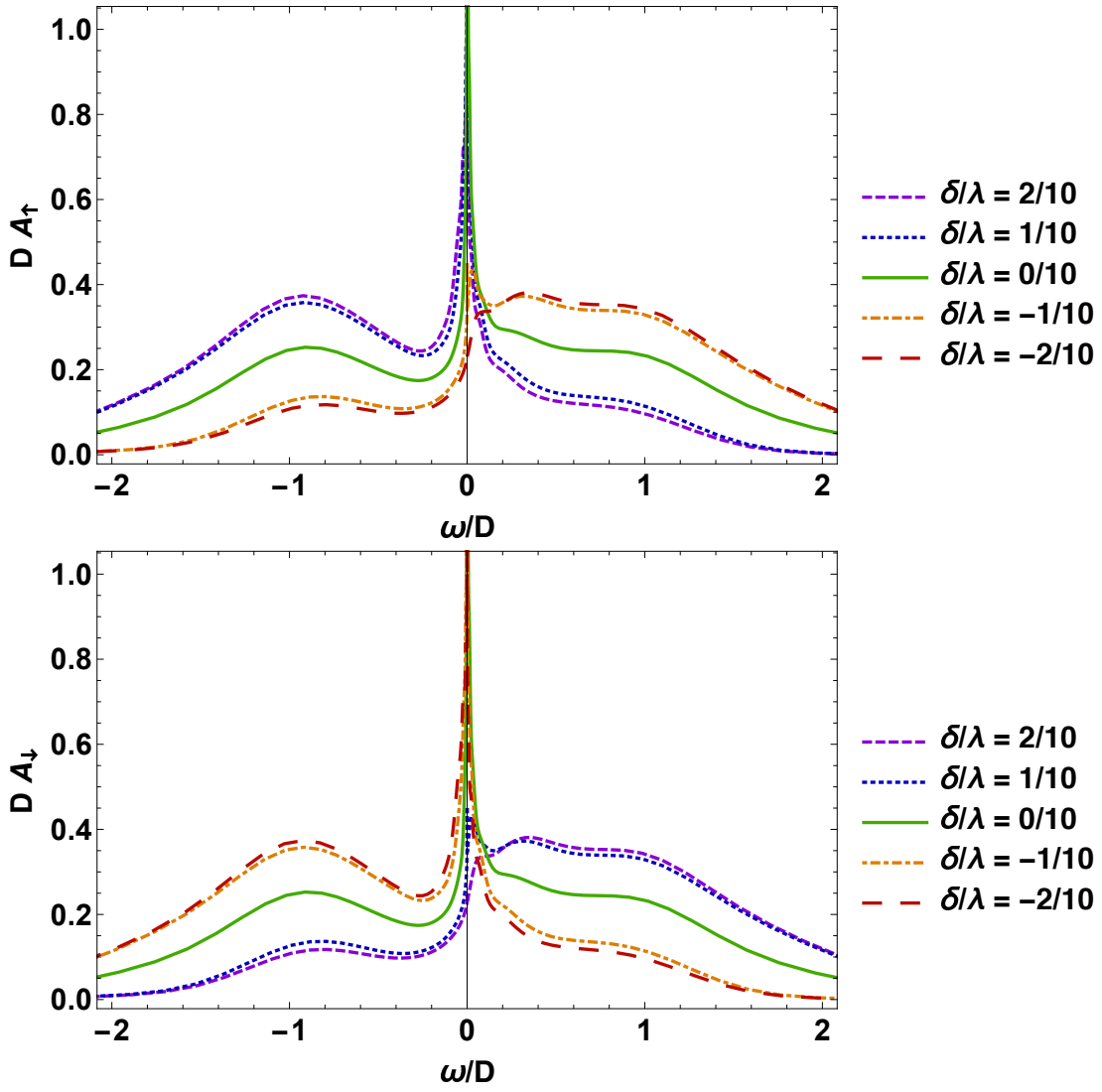


Figure 3.15: The impurity spectral functions at various δ, for spin up (top) and down (bottom). The pattern of Fig. 3.14 is repeated as expected, with a reversal of roles as δ becomes negative.

3.5 Comparison of Methods

The two methods used to explore the Kondo effect in monolayer TMDs, a variational ground state and NRG, have yielded some very contrasting results but they still have much in common. For example, the temperature scale in the variational method (for WSe_2 with

the parameters of the previous section) is $\sim 2-4$ K, and we found that in NRG at large U the scale is roughly in agreement at $\gtrsim 4$ K. Also, the primary spin content for the impurity and the system as a whole is the same (zero) in both methods so long as the excitative circularly polarized light is not shining. We do not have a J^2 to compare, but in NRG the nonzero value of susceptibility $T\chi$ as $T \to 0$ suggests that there is s some moment surviving with $J_z = 0$, apparently agreeing with the variational result. Since NRG is a widely used and trustworthy method[34, 38, 39, 41, 42, 66], these agreements give some grounding of truth in the variational state.

The differences between the two methods really become apparent once the system is excited by the appropriate circularly polarized light, under the right conditions giving the impurity a spin preference when hybridizing with the bath electrons. A common thread is that the impurity spin $\langle S_z \rangle$ becomes polarized in either method, but the magnitude is much larger in NRG. Also, the variational method leads to a conservation response from the bath electrons, cancelling out the polarization of the impurity, but this is entirely absent from NRG. In fact, the spin in Fig. 3.13 is representative of the change in total spin $\langle J_z \rangle - \langle J_z \rangle_0$ due to the presence of the impurity and reveals a paramagnetic character, rather than the static nonmagnetic character of the variational state. Correspondingly, we see in Fig. 3.10 an increase in the low-temperature part of $T\chi$ with the magnitude of the induced offset δ, signaling an increase in J^2 from the development of a moment on the impurity along z; meanwhile, we saw almost no shift in J^2 in the variational method (Fig. 3.4), with the only change being due to the varying distance from the Bloch pole with offset δ. It appears that the variational wave function (3.15), forced to have only components with z

spin $m = 0$, cannot capture the polarized state that should arise, according to NRG, when optical excitations offset the chemical potentials.

The spectral functions from the NRG method offer further information that was not available in the variational method. As we saw in Fig. 3.9, the case that is not excited by light displays rather conventional features for an impurity level in the mixed-valence regime, with its energy level placed relatively close to the chemical potential. Once the chemical potentials are offset, however, the spectral functions are split but they appear very different from simply applying a magnetic field[73]. Because we are shifting the impurity levels ε_0 and the bath (or chain) levels ϵ_m, we see a preservation of the sharp resonance peak corresponding to the spin at higher chemical potential, while the lower chemical potential leads to a greatly diminished peak for the opposite spin. Of course the sign of offset acts like the sign of some kind of magnetic field so in Fig. 3.15 we see the appropriate role-reversal of spin up and down, along with the gradual disappearance of the sharp peak for one of the spins as δ is increased. It is worth noting also that the appropriate sharp peak, while preserved, is actually shifted slightly in the expected direction as δ is increased (note the difference in sign between our effective field and the H of ref. [73]).

3.6 Conclusions

TMDs provide an exciting new venue to study the interplay of spin orbit coupling, topology and correlations. While prior studies on two dimensional systems have focussed on Rashba spin orbit coupling [74, 75] predicting an increased Kondo temperature, a more general analysis in noncentrosymmetric metals showed that the conclusions deduced from

them were not universally true [71]. In TMDs we have a particular realization of Dresselhaus spin orbit coupling that leads to a lowering of the Kondo scale which arises from the reduced density of states due to spin splitting, reduction of effective band width, and suppression of hybridization due to Berry curvature. The dominant hybridization channel is also determined by the symmetry of the impurity state and the Berry curvature. The finite triplet admixture assures the resonance contains spin fluctuations though it remains nonmagnetic under normal conditions. Furthermore the composition of the Kondo cloud can be tuned by circularly polarized light leading to a (steady-state) optically excited Fermi sea.

Apparently, due to the shortcomings of the variational state, one must use a more systematic approach like NRG to correctly capture even the qualtiative behavior of the excited system. In particular we have found that the spin content of the ground state in the presence of dilute magenetic impurites, usually described by a Kondo singlet, is described by a mixed singlet and $m = 0$ triplet state, and from NRG we infer that $m \neq 0$ triplet components are added when the Fermi sea is excited to give an offset $\delta \neq 0$. We thus have in monolayer TMDs a Kondo effect with triplet contributions and whose magnetic/spin content may be tuned by the application of circularly polarized light, allowing for optomagnetic manipulation and providing a new route for studying Kondo phenomena.

Chapter 4

Conclusions

This work has gone through some case studies on the subject of topological phases and phenomena in materials. A lot of ground has been covered, so here we restate the main findings.

4.1 Diagnostics of Nodal Semimetals

In the first case, explored in Chapter 2, we have examined an interesting instance of a nodal semimetal called a line-node semimetal. The phase is realized by the heterostructure of alternating topological/normal insulator layers proposed previously[2, 25], but the direction of magnetic coupling is switched to be in-plane. We have assessed the band structure by looking at the energy near the node, going perpendicular to the curve, which revealed a linear dependence up to a particular distance away from the node dependent on the position along the curve. For very open (almost straight) curves, the result of very large magnetic coupling, the outcome is invariant in the k_z direction and the linear trend means that a

graphene-like dispersion is obtained. As one might expect, the similarity of open curves to graphene leads to a conductivity which is independent of the magnetic coupling, providing an asymptotic value.

As discussed in Chapter 2 and Appendix B, the line-node semimetal requires the Self-Consistent Born Approximation in order to calculate the conductivity using the Kubo formula. In this work we utilize the previous calculations[25] on the point that the density of states $g(\varepsilon)$ is linear in energy, but the slope of that line is determined by numerically calculating the volume of the Fermi surface $N(\varepsilon)$ whose derivative gives the density of states. The slope, and correspondingly the conductivity σ, grows with increasing magnetic coupling m although the details of the growth differ from the simple approximation $\sigma \propto m$, particularly at very small and very large coupling.

The manipulation of the line-node, its size and whether or not it's closed, is easily demonstrated by changing the magnitude of magnetic coupling. Since the coupling may originate in ferromagnetic insulators (such as EuO), it can be modified with temperature changes and thus the Fermi surface itself can be tuned. One can observe this via the transport as described above, or the Fermi surface can be probed directly by looking at magnetic (de Haas-van Alphen) oscillations. We map out the frequencies of oscillation in $1/B$ as the field B is varied, which are related to the extremal areas of the Fermi surface. Interestingly, there is a particular point where the Fermi surfaces changes its topology from that of a torus to that of a sphere, effectively doubling the frequency.

The exploration of this exotic topological phase has several lessons, but the common thread is that everything is *tunable*. This case was focused on a noninteracting system

(aside from some potential scattering), but it displayed some striking tunable features which could, in principle, be accessed experimentally.

4.2 Kondo Effect in Exceptional Circumstances

In the second case of this work, discussed in Chapter 3, we looked at the monolayer transition metal group-VI dichalcogenides (TMDs), specifically considering the Kondo effect. While the hole-doped TMD system has a finite density of states like normal metals, it is exceptional in that it has two valleys which are acting independently and which contain oppositely polarized holes in opposite valleys. The spin-splitting in the bands is so extreme that, for particular chemical potentials, holes have a single spin within a particular valley. This spin-valley locking leads to a Kondo bound state which is nonmagnetic but which is unusual, having both singlet and $m = 0$ triplet combinations. The mixture in the variational ground state is equal in each valley, so the result of total spin is almost exactly half of the triplet value: $J^2 \approx \hbar^2 = (1/2)J^2_{\text{triplet}}$.

We also considered the same situation but under application of circularly polarized light. When the frequency is chosen appropriately, to span the energy gap from the upper valence band vertically up to the conduction band, holes of a particular spin are added to the matching valley, chosen by the polarization. The valley/spin selectivity is due to optical circular dichroism which results from broken inversion symmetry, spin-splitting, and the topological character of the bands. Effectively, the chemical potentials for spin up and down in the upper valence bands are slightly shifted apart by some amount δ and the spin structure of the Kondo state is affected.

To address this point, we found that the variational method was insufficient and it was necessary to move to the Numerical Renormalization Group (NRG) method. Using the same asymmetrical Anderson model as for the normal case described above, NRG results revealed strongly polarized impurity occupations and even a net magnetization which depends on the chemical potential offset δ. The finding is that $m = \pm 1$ triplet combinations must also be included, although those pieces are not possible within the variational formulation. To make the case and understand the whole picture, many results are found within NRG including entropy, susceptibility, and spectral functions. Despite their differences, the Kondo temperature within NRG was found to be of the same order of magnitude as the energy scale from the variational ground state, indicating an important physical consensus.

In this case we investigated Kondo screening in a very interesting two-dimensional system, and we considered the effects of circular dichroism. The common thread of this case was the inclusion of *interactions* in an already nontrivial topological material. Interestingly, the ability to manipulate the spin populations with light also allowed for the internal structure to be *tunable*. The investigation of this last point required an entirely new approach beyond a simple variational or mean field method, and led to an interesting result.

4.3 Future Directions

The future is bright for topological phases and phenomena. The work here has shown that the tunable parameters can have drastic effects on the low energy structure, and introducing interactions like an Anderson impurity creates new physical outcomes.

Future works may focus on the surface states implied by line-node semimetals or

other nodal semimetals, and how those states may be tuned with some parameter. Or they may look at the TMDs in with other interactions like superconductivity, or with respect to spintronic applications, which can be tuned with circularly polarized light. One important point that could be applied to interacting systems is that the basic existence of phases, like the Kondo bound state, does not go away in topological systems but the properties can be unexpected.

Of utmost importance is future experimental work. It would require strong fields, but the magnetic oscillations of the line-node semimetal would be very interesting to witness, especially the frequency-doubling that results from a simple change of temperature. In the case of tuning the Kondo state with light, a challenge would be the measurements on the system which should be made while the light is still shining on it. However, again the possible result would be very interesting, the system becoming clearly magnetic when the appropriate circularly polarized light is shining. If one is measuring the resistivity, the expectation is rather standard since the system is still forming a Kondo bound state of some sort, but the Kondo temperature is expected to be lower due to spin-splitting. After characterization, the next step would be to investigate and implement the devices which may be built.

From a theoretical point of view, the primary next step is to look at the possibilities of interactions in other tunable systems with topological properties. Additionally, the use of interacting systems and topology may be investigated for applications, in parallel to the use of superconductors with Majorana modes intent on applications to quantum computing.

Appendix A

Berry Phase and Adiabatic Changes

In his 1984 paper, M. V. Berry showed that general quantum states pick up a *geometrical* phase when taken around some adiabatic path. This is exactly the same phase that appears classically in the case of the Foucault pendulum as it rotates (adiabatically) with the Earth. In this treatment, Berry phase is derived, and the related quantities Berry connection and Berry curvature are defined. Additionally, the parallel between these quantities and magnetism is built up, with a brief discussion of physical versus unphysical quantities. We focus on the most general appearance of these topological quantities in quantum mechanics, with no specific system assumed. A generic example is also provided.

A.1 Adiabatic Changes in Quantum Mechanics

First off is the adiabatic theorem for quantum mechanics. Imagine a system in an eigenstate $|n\rangle$ of some Hamiltonian $\mathcal{H}$, with a corresponding energy E_n. If $\mathcal{H}$ picks up a slowly-varying time dependence, the adiabatic theorem states that the system will remain in the n^{th} eigenstate (now also dependent on time).

For example, consider the ground state of the one-dimensional infinite well. On the one hand, if the width of the well is changed from a to $2a$ instantaneously, the wave function will remain the same:

$$\psi_0(x) = \begin{cases} A\sin(\pi x/a) & , \quad 0 < x < a \\ 0 & , \quad \text{otherwise.} \end{cases} \tag{A.1}$$

From here, one could calculate a transition probability to the ground state of the final Hamiltonian (which is neither 1 nor 0). However, if the width is changed from a to $2a$ very slowly (adiabatically), the wave function will change accordingly, leading to a final wave function

$$\psi_0'(x) = \begin{cases} A'\sin(\pi x/2a) & , \quad 0 < x < 2a \\ 0 & , \quad \text{otherwise.} \end{cases} \tag{A.2}$$

In this example, it's clear how the changes in the Hamiltonian appear as changes in some parameter like the width of the well.

A.1.1 Rigorous Setup

To put this all together, the take the eigenvalue equation

$$\mathcal{H}(\mathbf{R}(t))\,|n(t)\rangle = E_n(\mathbf{R}(t))\,|n(t)\rangle \tag{A.3}$$

where $\mathbf{R}(t)$ is the vector made out of N time-dependent parameters (assuming $N \geq 1$ for generality)[1].

Now, take a *general* state $|\Psi(t)\rangle = \sum_n |\psi_n(t)\rangle$, with the definition

$$|\psi_n(t)\rangle = c_n(t)\mathrm{e}^{-i\phi_n(t)} |n(t)\rangle \tag{A.4}$$

such that $|\Psi(0)\rangle = |n(0)\rangle$ at $t = 0$. The "dynamical phase" $\phi_n(t) = \frac{1}{\hbar}\int_0^t E_n(t')dt'$ is the expected evolution for a state subject to a time-dependent Hamiltonian. The factors $c_n(t)$ are determined by the time-evolution equation given by

$$\mathcal{H}(\mathbf{R}(t)) |\Psi(t)\rangle = i\hbar \frac{d}{dt} |\Psi(t)\rangle \tag{A.5}$$

To proceed, use the definitions of $|\Psi(t)\rangle$ and $\phi_n(t)$, and use Eq. (A.3) where possible:

$$\sum_n c_n E_n \mathrm{e}^{-i\phi_n(t)} |n(t)\rangle = \sum_n \left(c_n E_n \mathrm{e}^{-i\phi_n(t)} + i\hbar \dot{c}_n \mathrm{e}^{-i\phi_n(t)} + i\hbar c_n \mathrm{e}^{-i\phi_n(t)} \frac{d}{dt} \right) |n(t)\rangle \tag{A.6}$$

$$\Rightarrow \quad \dot{c}_{n'} = -\sum_n c_n \mathrm{e}^{-i(\phi_n - \phi_{n'})} \langle n'| \frac{d}{dt} |n\rangle \tag{A.7}$$

where a dot above means a time derivative (and some explicit time-dependence is omitted). The second line is obtained by applying $\langle n'|$ to both sides, assuming the usual orthonormality relation: $\langle n'(t)|n(t)\rangle = \delta_{n,n'}$. We essentially seek to solve for $c_n(t)$, so some simplification is required. Taking the time derivative of Eq. (A.3), then applying the state bra $\langle n'(t)|$ and using the hermicity of $\mathcal{H}$ to act to the left gives

$$\langle n'| \dot{\mathcal{H}} |n\rangle + E_{n'} \langle n'| \frac{d}{dt} |n\rangle = \dot{E}_n \delta_{n,n'} + E_n \langle n'| \frac{d}{dt} |n\rangle \ . \tag{A.8}$$

[1]To tie this formulation to the case of Bloch electrons, the role of time-dependent parameters is taken by the crystal momentum $\mathbf{k}$.

Substituting this (assuming non-degenerate eigenvalues) into Eq. (A.7) for the two cases $n = n'$ and $n \neq n'$ results in a first-order differential equation for $c_n(t)$ given by

$$\dot{c}_{n'} = -c_{n'} \left\langle n' \right| \frac{d}{dt} \left| n' \right\rangle - \sum_{n \neq n'} c_n \mathrm{e}^{-i(\phi_n - \phi_{n'})} \left(\frac{\left\langle n' \right| \dot{\mathcal{H}} \left| n \right\rangle}{E_n - E_{n'}} \right) . \tag{A.9}$$

Note that this result is actually *exact*[2]. The actual adiabatic approximation is yet to come.

A.1.2 Berry Phase

Now, the adiabatic approximation is formally employed by blatantly ignoring the entire sum with $\dot{\mathcal{H}}$ in Eq. (A.9). This is essentially what was stated previously: the Hamiltonian $\mathcal{H}$ is still dependent on time, but it varies extremely slowly[3]. This leads to the most simple possible solution

$$c_n(t) = \mathrm{e}^{i\gamma_n(t)} , \tag{A.10}$$

since the definition Eq. (A.4) forces $c_n(0) = 1$. Finally, Berry Phase is defined as the quantity

$$\gamma_n(t) = i \int_0^t \left\langle n(t') \right| \frac{d}{dt'} \left| n(t') \right\rangle dt', \tag{A.11}$$

which appears as the "geometrical phase" present in the solution for Eq. (A.4). Note that, due to the time derivative, this phase is indeed real-valued[4].

Up to this point, the time-dependent parameter-space $\mathbf{R}(t) \in \mathbb{R}^N$ has been ignored. To "simplify" Eq. (A.11), a transformation can be made to make the integral over time into an integral over the parameter-space:

$$\frac{d}{dt'} \rightarrow \frac{d\mathbf{R}}{dt'} \cdot \boldsymbol{\nabla}_R . \tag{A.12}$$

[2]For details, see Ref. [76].

[3]For a more rigorous (nontrivial) justification, see Ref. [77].

[4]If not convinced, take the derivative of the orthonormality relation following Eq. (A.7) to show that $\frac{d}{dt} \langle n|n \rangle = 2 \cdot \mathrm{Re}(\langle n| \frac{d}{dt} |n\rangle) = 0$.

Furthermore, if one assumes periodicity (i.e. $\mathbf{R}(T) = \mathbf{R}(0)$ for some $T > 0$) then Berry phase becomes a function of the closed path $\mathcal{C}$

$$\gamma_n(\mathcal{C}) = i \oint_{\mathcal{C}} \langle n(\mathbf{R})| \boldsymbol{\nabla}_R |n(\mathbf{R})\rangle \cdot \mathbf{dR} \,. \tag{A.13}$$

A.2 Berry Connection and Curvature

Now that Berry phase is well defined as a function of eigenstates and a path in parameter-space, we can define additional quantities to make use of Stokes' Theorem.

A.2.1 Definitions

First off is the Berry Connection, defined as the total integrand of Eq. (A.13):

$$\boldsymbol{\mathcal{A}}^{(n)}(\mathbf{R}) = i \langle n(\mathbf{R})| \boldsymbol{\nabla}_R |n(\mathbf{R})\rangle \ . \tag{A.14}$$

Then, the Berry Curvature (pseudo-vector form) is simply defined as

$$\boldsymbol{\mathcal{B}}^{(n)}(\mathbf{R}) = \boldsymbol{\nabla}_R \times \boldsymbol{\mathcal{A}}^{(n)}(\mathbf{R}) \tag{A.15}$$

which makes it possible to express Berry Phase in the form

$$\gamma_n(\mathcal{C}) = \oint_{\mathcal{C}} \boldsymbol{\mathcal{A}}^{(n)}(\mathbf{R}) \cdot \mathbf{dR} = \int_{\mathcal{S}(\mathcal{C})} \boldsymbol{\mathcal{B}}^{(n)}(\mathbf{R}) \cdot \mathbf{dS} \tag{A.16}$$

where Stokes' theorem has been used to convert the N-dimensional contour integral into a "surface" integral in $\mathbf{R}$-space.

A.2.2 Alternate Forms

By applying $\boldsymbol{\nabla}_R$ to both sides of Eq. (A.3), the Berry Curvature can be expressed in the form[5]

$$\boldsymbol{\mathcal{B}}^{(n)}(\mathbf{R}) = i \sum_{n' \neq n} \frac{\langle n | \boldsymbol{\nabla}_R \mathcal{H} | n' \rangle \times \langle n' | \boldsymbol{\nabla}_R \mathcal{H} | n \rangle}{(E_n - E_{n'})^2} \, . \tag{A.17}$$

Also, the curvature can be expressed more generally as a tensor:

$$\mathcal{B}^{(n)}_{\mu\nu}(\mathbf{R}) = \frac{\partial}{\partial R^\mu} \mathcal{A}^{(n)}_\nu - \frac{\partial}{\partial R^\nu} \mathcal{A}^{(n)}_\mu \, . \tag{A.18}$$

This results in a corresponding identity $\mathcal{B}^{(n)}_{\mu\nu} = \varepsilon_{\mu\nu\lambda} (\boldsymbol{\mathcal{B}}^{(n)})_\lambda$ relating to the previous pseudo-vector definition Eq. (A.15) where $\varepsilon_{\mu\nu\lambda}$ is the Levi-Civita symbol.

In the same spirit as Eq. (A.17), the tensor form can be written as

$$\mathcal{B}^{(n)}_{\mu\nu}(\mathbf{R}) = i \sum_{n' \neq n} \left[\langle n | \frac{\partial \mathcal{H}}{\partial R_\mu} | n' \rangle \langle n' | \frac{\partial \mathcal{H}}{\partial R_\nu} | n \rangle - (\mu \leftrightarrow \nu) \right] / (E_n - E_{n'})^2 \, , \tag{A.19}$$

where the notation $(\mu \leftrightarrow \nu)$ indicates a label swap of the previous term.

A.2.3 Relation to Magnetism

Absolutely everything is now defined in the most general way. So how does this tie in with magnetism? The notation should provide a hint: identify the Berry connection given by Eq. (A.14) with the magnetic vector potential $\mathbf{A}(\mathbf{r})$ and note that the result is a parallel between the curvature Eq. (A.15) and the magnetic field $\mathbf{B}(\mathbf{r})$. This finally implies, via Eq. (A.16), that Berry phase is identified with the magnetic flux $\Phi_B(\mathcal{C}_r)$ through the area bounded by the closed curve $\mathcal{C}_r$ in physical space.

[5] For details, see Supplement I of Ref. [78].

Putting this all together:

$$\boldsymbol{\mathcal{A}}^{(n)}(\mathbf{R}) \quad \longleftrightarrow \quad \mathbf{A}(\mathbf{r}) \tag{A.20}$$

$$\boldsymbol{\mathcal{B}}^{(n)}(\mathbf{R}) \quad \longleftrightarrow \quad \mathbf{B}(\mathbf{r}) \tag{A.21}$$

$$\gamma_n(\mathcal{C}) \quad \longleftrightarrow \quad \Phi_B(\mathcal{C}_r) \ . \tag{A.22}$$

In fact, the parallel runs even deeper than this: the magnetic field and flux are known to be "physical" quantities, whereas the vector potential depends on the gauge. To continue the parallel given by the above (A.20)-(A.22), consider the set of eigenstates offset by an arbitrary (parameter-dependent) phase:

$$|\widetilde{n}\rangle = \mathrm{e}^{-i\beta(\mathbf{R})}\,|n\rangle \ . \tag{A.23}$$

For continuity following from the periodicity of $\mathbf{R}$, we must have $\beta(\mathbf{R}(T)) = \beta(\mathbf{R}(0)) + 2\pi m$, where m is some integer. By looking at Eq. (A.13) (or elsewhere), we observe that Berry phase changes to

$$\widetilde{\gamma}_n(\mathcal{C}) = \gamma_n(\mathcal{C}) + 2\pi m \tag{A.24}$$

which is invariant in the phase sense (i.e. invariant modulo 2π). Conversely, the connection (from the definition Eq. (A.14)) is not invariant

$$\widetilde{\boldsymbol{\mathcal{A}}}^{(n)} = \boldsymbol{\mathcal{A}}^{(n)} + \boldsymbol{\nabla}_R\beta, \tag{A.25}$$

while the curvature (from Eq. (A.15)) actually *is* invariant

$$\widetilde{\mathcal{B}}^{(n)} = \mathcal{B}^{(n)} + \boldsymbol{\nabla}_R \times \boldsymbol{\nabla}_R\beta = \mathcal{B}^{(n)} \ . \tag{A.26}$$

This shows how, in the quantum mechanical sense, Berry phase and curvature are gauge-invariant (hence "physical") quantities, while the connection is not – just as one would guess given the parallel in (A.20)-(A.22).

A.3 An Example: Particle in Slow-Varying B Field

To illustrate the meaning of Berry phase and curvature, take the example of a spin-s particle sitting in a time-dependent magnetic field $\mathbf{B}(t)$. Then, assume the field maintains a constant magnitude B_0 so that it can be expressed as

$$\mathbf{B}(t) = B_0 \left[\hat{z}\cos\theta + \sin\theta\left(\hat{x}\cos\omega t + \hat{y}\sin\omega t\right)\right] \tag{A.27}$$

with a fixed polar angle θ. To satisfy the adiabatic limit, the frequency ω is assumed to be 'very small'. With these definitions, consider eigenstates along the *field* direction $\hat{z}' = \mathbf{B}(t)/B_0$:

$$\mathcal{H}(t)\left|m\right\rangle = E_m\left|m\right\rangle, \quad S_{z'} = m\hbar \quad (m = -s, -s+1, ..., s-1, s)\,. \tag{A.28}$$

The Hamiltonian and eigenvalues become

$$\mathcal{H}(t) = -g\mu\mathbf{S}\cdot\mathbf{B}(t)/\hbar \equiv \mathcal{H}(\mathbf{B}), \quad E_m = -g\mu B_0 m \tag{A.29}$$

where μ is the Bohr magneton.

At this point, we seek to find Berry phase using the 3D curve $\mathcal{C}$ specified by Eq. (A.27). First, we obtain the *curvature* using Eq. (A.17).

Notice that the gradient of $\mathcal{H}$ in parameter space is $\boldsymbol{\nabla}_B\mathcal{H} = -g\mu\mathbf{S}/\hbar$. The z-component of this gradient will go to zero in Eq. (A.17), since the sum runs over non-degenerate states and S_z doesn't modify the states. To evaluate the other components, use the ladder operators $S_\pm = S_x \pm iS_y$ to write the matrix elements

$$\left\langle m \pm 1\right| S_x \left|m\right\rangle = \frac{\hbar}{2}\sqrt{(s \mp m)(s \pm m + 1)} \tag{A.30}$$

$$\left\langle m \pm 1\right| S_y \left|m\right\rangle = \mp i\frac{\hbar}{2}\sqrt{(s \mp m)(s \pm m + 1)}\,. \tag{A.31}$$

Now, Berry curvature has two terms

$$\boldsymbol{\mathcal{B}}^{(m)} = \frac{i\hat{z}}{\hbar^2 B_0^2}\left[-2i\frac{\hbar^2}{4}[(s-m)(s+m+1)-(s+m)(s-m+1)]\right] = -\frac{m}{B_0^2}\hat{z} \tag{A.32}$$

and Berry phase can be evaluated exactly (using Eq. (A.16)) as

$$\gamma_m = \int_{\mathcal{S}(\mathcal{C})} -\frac{m}{B_0^2}\hat{z}\cdot d^2\mathbf{B} = 2\pi m(\cos\theta - 1) = -m\Omega_B \tag{A.33}$$

where the Ω_B in the last equality denotes the solid angle traced by the curve $\mathcal{C}$ in $\mathbf{B}$-space, with respect to the origin.

Note, from the form of $\mathcal{H}(\mathbf{B})$ in Eq. (A.29), that there was a degeneracy at the point $\mathbf{B} = 0$ (where $E = 0$ also). This would lead to a divergent curvature at this point, as can be seen by taking $B_0 \to 0$ in Eq. (A.32). The existence of such a point is required to give a finite phase for any curve $\mathcal{C}$ that avoids crossing $\mathbf{B} = 0$, which is evident since the solid angle in Eq. (A.33) is taken with respect to the degeneracy point.

Appendix B

Self-Consistent Born Approximation

Here we explain the background and main concepts behind the simplest calculations of the conductivity in a generic system. We will not go into full detail; we present only the main structure with accompanying references. Semi-classically, the conductivity is (basically) proportional to the density of charge carriers n and the time between scatterings off of impurities τ[49]. The latter comes from inverting the scattering rate, which is calculated using some chosen method, with some form of impurity potentials. For rigor and transparency, Green functions and diagrammatic expansions are typically employed to calculate impurity effects[34, 79, 80]. To get things like the conductivity more directly, a linear response formalism can be developed leading to the Kubo formula, which involves the Green functions in a transparent way and allows for an examination of all possible contributions.

We first explain the starting point and the generic method for extracting the

scattering rate from a Green function, given potentials from a random distribution of impurities. Then, the Born Approximation and Self-Consistent Born Approximation (SCBA) are explained. Schematic diagrams are included where appropriate.

B.1 Potential Scattering

Since we are not focusing on any particular system, the Hamiltonian with impurity scattering is easily stated:

$$H = \sum_{\alpha} \epsilon_{\alpha} c_{\alpha}^{\dagger} c_{\alpha} + \sum_{\alpha,\beta} v_{\alpha,\beta} c_{\alpha}^{\dagger} c_{\beta} \; . \tag{B.1}$$

In a typical metal one has Bloch electrons labeled by $\alpha \sim \{\mathbf{k}, s\}$, although we will drop the spin labels since they play little role here. With impurities located at $\mathbf{R}_j$ giving central potentials u, the total scattering contribution is $V(r) = \sum_j u\left(\mathbf{r} - \mathbf{R}_j\right)$. At the end of a calculation, one must average over the random locations $\mathbf{R}_j$. After projecting to momentum space, we see that

$$v_{\alpha,\beta} \to \frac{1}{\Omega} V_{\mathbf{k},\mathbf{k}'} = \frac{1}{\Omega} \int d^d r \, V(r) \mathrm{e}^{-i(\mathbf{k}-\mathbf{k}')\cdot\mathbf{r}} \tag{B.2}$$

where the system volume (d-dimensional) is written Ω. In order to do something very specific, the central potential u must be chosen; in Sec. 2.3 we use point-like impurities with $u(\mathbf{r}) = u_0 \delta(\mathbf{r})$, giving $V_{\mathbf{k},\mathbf{k}+\mathbf{q}} = u_0 \sum_j \exp(i\mathbf{q}\cdot\mathbf{R}_j)$.

With the Hamiltonian including impurity potentials, we can proceed to the Green functions. In a clean system with zero impurities, the (retarded) Green function for the Bloch electrons is

$$\mathcal{G}_{\mathbf{k},\mathbf{k}'}(\omega) = \frac{\delta_{\mathbf{k},\mathbf{k}'}}{\omega - \epsilon_{\mathbf{k}} + i\eta} \tag{B.3}$$

where the limit $\eta \to 0^+$ is taken at the end. Diagrammatically, the clean Green function is depicted by a simple line. The introduction of impurities gives some more terms in the denominator of the Green function for the Bloch electrons. A simple way to capture the

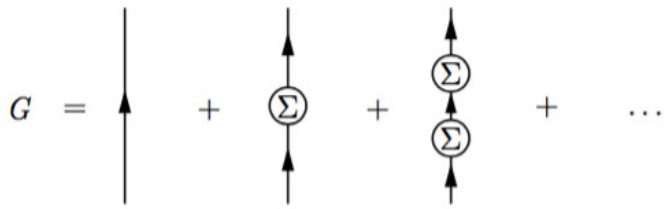


Figure B.1: The Green function with impurity scattering is represented as an infinite series involving the Green functions of the pure system and the self-energy.

effects is to introduce a self-energy, i.e. the new Green function is written in the form

$$G(\omega) = \frac{1}{\omega - \epsilon_{\mathbf{k}} - \Sigma_{\mathbf{k}}(\omega) + i\eta} = \mathcal{G} + \mathcal{G}\Sigma\mathcal{G} + \mathcal{G}\Sigma\mathcal{G}\Sigma\mathcal{G} + \dots \tag{B.4}$$

where the second equality is a schematic series expansion (see Fig. B.1). The self-energy is defined essentially as the sum of all scattering diagrams which cannot be separated by cutting a single Green function line. Thus all of the complexity is moved into the determination of the self-energy, and naturally this is where the key approximations are typically made. Before moving on to describing the approximations, we note a very useful property of the self-energy: it is related to the width of the energy peak and thus the scattering rate by $\hbar/\tau = -2\,\mathrm{Im}[\Sigma]$.

B.2 Born and SCBA

The most general self-energy, with a sample shown in Fig. B.2, contains many combinations of potential scatterings (depicted by dashed lines) off of one ore more impurities (depicted by crosses). It is not possible to take into account every single diagram that will appear in

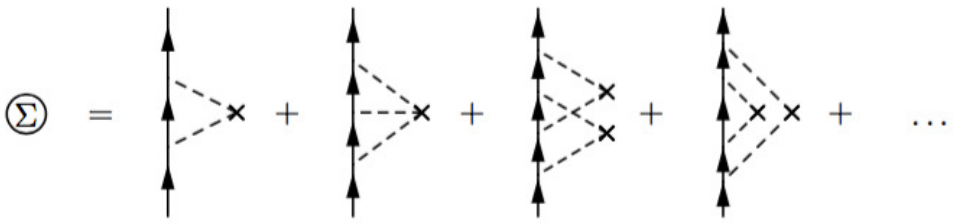


Figure B.2: A few of the simplest diagrams are shown from the exact self-energy due to impurity potentials. Dashes are interaction lines, crosses indicate impurity sites (each giving a factor of impurity concentration).

the exact self-energy. To make a rough approximation, one can take only the first diagram of Fig. B.2 and put it into the Green function — this is the Born approximation, the result depicted in Fig. B.3. The corresponding equation for the self-energy is, schematically,

$$\Sigma(\omega) \approx V\mathcal{G}(\omega)V \ . \tag{B.5}$$

In this case, one is neglecting a very large subset of diagrams and it is important to understand the conditions under which the approximations is trustworthy.

First, it is a single impurity diagram so the contribution will be proportional to the impurity concentration $n_{imp.}$, which is taken to be comparatively small for clean systems. Second, only a single scattering event is included on that one impurity. In other words, the electron enters alone, scatters alone, and then leaves. For this to be an accurate description,

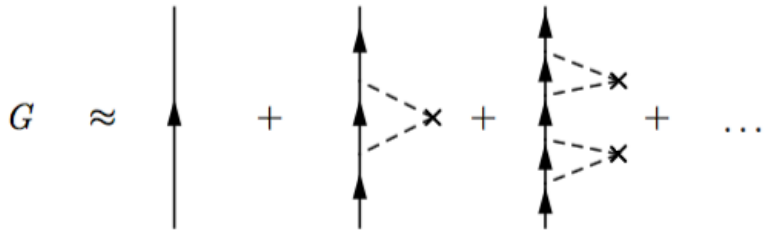


Figure B.3: The series of diagrams for the Green function within the simple Born approximation. This is the same as Fig. B.1, but taking only the first piece on the r.h.s. of Fig. B.2.

the influence of the impurity potential must be comparatively small, meaning that the strength (e.g. the above u_0 for point-like impurities) must be small compared to the energy of the incoming electrons. When a large number of electrons is involved it is more useful to refer to the density of states; the equivalent statement is that the typical electron energy must be large compared to the interaction times the density of states, $\epsilon \gg |V|^2 g(\epsilon)$. At low temperatures only the lowest-energy states are affected, and we see that the key property is how the density of states scales with energy near the chemical potential. With a power law $g(\epsilon) \propto \epsilon^P$, one would require that $P > 1$ for the Born approximation to apply; for Weyl semimetals, $P = 2$ and indeed the Born approximation is used with confidence[25]. One may note also that the use and trust of the simple Born approximation is better captured within the semiclassical formulation with Boltzmann's equation, but the diagrammatic approach allows for more transparency and further approximations such as the one we are about to take.

What if we have a density of states with $P \leq 1$, as in the case of line-node semimetals? Physically, this means that the density of electrons is too high, i.e. too many

are scattering simultaneously, so that multiple-scattering diagrams become more important. In Fig. B.2, we see various choices for further corrections to the self-energy. The second diagram, with three interaction lines, is higher-order and represents a corrected single-scattering event. The next diagram has crossing interaction lines, so the two impurities are said to be "interfering" and the result is typically a very small correction. The last diagram, however, looks just like the first except that the internal electron line is replaced by a line with the first correction included; this is the best picture of what we mean by multiple-scattering diagrams, since the electron taking part in an event has already been scattered.

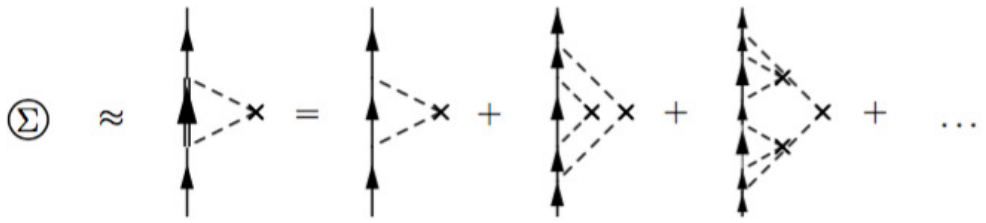


Figure B.4: The self-energy used within SCBA, in accord with Eq. (B.7), where the exact Green function is depicted by a double line. The second equality shows some terms resulting from the expansion of the internal Green function.

Including all diagrams like the rightmost of Fig. B.2 generates the Self-Consistent Born Approximation. As suggested, this is the same as the regular Born approximation except that the electron taking part in the process is assumed to be corrected already. The

result involves coupled equations for the Green function and the self-energy appearing in it,

$$G(\omega) \approx \frac{1}{\omega - \epsilon_{\mathbf{k}} - \Sigma_{\mathbf{k}}(\omega)} \tag{B.6}$$

$$\Sigma(\omega) \approx VG(\omega)V \tag{B.7}$$

hence the term "self-consistent". As seen in Fig. B.4, the structure of the self-energy diagram is identical to that of the Born approximation, but the structure of the Green function involved is very different, like a deeply nested version of Fig. B.3. Clearly, it is advantageous to use the simple Born approximation in most cases, but the SCBA must be employed in exceptional cases where the density of states remains too large evan at low energies, such as the line-node of Chapter 2.

Appendix C

Variational State and Spin

Here we present details and supplemental information for the calculations of Sec. 3.3. First we discuss the form of variational state chosen to describe the Kondo effect in monolayer TMDs, and how the parameters are determined. Then, we go into the details of how properties are extracted from the state, specifically the spin and susceptibility.

C.1 State and Parameters

The variational approach to understanding the Kondo effect and the underlying ground state dates back to the early years of Kondo physics[36, 37]. The main idea is that the ground state for the Anderson model should be a superposition of states which are closely related to the ground state of the pure metal (i.e. the Fermi sea),

$$|\psi_0\rangle = \prod_{\ell,s}^{\mu} c^\dagger_{\ell,s} \, |\text{vacuum}\rangle \ . \tag{C.1}$$

As elsewhere, we use the shorthand $\ell = \{n, \mathbf{k}, \tau\}$. At most, the impurity should be singly-occupied because of the strong Coulomb energy U. Due to the spin-spin valley-locked band

structure of the TMDs, we already expect that the parameters will be spin-dependent within each valley. Allowing this, we get the simple form stated in Sec. 3.3,

$$|\psi\rangle = b_0 |\psi_0\rangle + \sum_{\ell,s} B_{\ell,s} f_s^\dagger c_{\ell,s} |\psi_0\rangle \ . \tag{C.2}$$

As noted in that section, the above for is equivalent to Eq. (3.15) with separated singlet/triplet parameters $p_\ell = (B_{\ell,\uparrow} + B_{\ell,\downarrow})/2$ and $t_\ell = (B_{\ell,\uparrow} - B_{\ell,\downarrow})/2$. Here we use the compact form above for calculations involving the state.

To determine the parameters b_0 and $B_{\ell,s}$ of the ground state, the energy is calculated and minimized. The Hamiltonian is $H = H_m + H_{imp} + H_V$ as defined in Chapter 3. The energy is traditionally calculated as the quantum average $\langle\psi| H |\psi\rangle / \langle\psi|\psi\rangle = E_{\text{var.}}$, which then has to be minimized[78]. To avoid differentiating a quotient, we use an alternative method with the equation rewritten $\langle\psi| H |\psi\rangle = E_{\text{var.}} \langle\psi|\psi\rangle$ alongside the normalization constraint $\langle\psi|\psi\rangle = 1$ enforced at the end. The energy $E_{\text{var.}}$ is the variational energy which is yet to be determined. For transparency, and to extract a Kondo temperature scale, it is best to write the energy as a starting point plus a shift, $E_{\text{var.}} = E^0_{\text{var.}} + \epsilon$. Generally the shift ϵ must be negative in order for the variational state (C.2) to be an improvement to the trivial state.

The starting point $E^0_{\text{var.}}$ is the energy of the metal after introduction of the impurity, but without hybridization. The metal alone, before the impurity, has energy $E_0 = \langle\psi_0| H_m |\psi_0\rangle = \sum'_{\ell,s} E_{\ell,s}$, the sum being over states below the chemical potential. When the impurity level is above the chemical potential, its introduction will not affect the energy (until hybridization is added). When the level is below the chemical potential, however, a single electron will travel down to fill the impurity (avoiding double-

occupation) and the energy is reduced by the difference, $E^0_{\rm var.} = E_0 + \varepsilon_0$, with relative energy $\varepsilon_0 = \varepsilon_{imp.} - \mu < 0$. Thus, we are looking for the parameters b_0 and $B_{\ell,s}$ and the shift ϵ by differentiating the equation

$$\langle\psi|\, H\, |\psi\rangle = (E_0 + \varepsilon_0 + \epsilon)\, \langle\psi|\psi\rangle \tag{C.3}$$

and enforcing normalization $\langle\psi|\psi\rangle = 1$. The above is the same as given at the beginning of Sec. 3.3, but is now fully motivated.

Before proceeding, we note the effect of a magnetic field since we will want the susceptibility. A magnetic field acting on the impurity will add $-\mu_0 \sum_{s,s'} \mathbf{h}\cdot f^\dagger_s \mathbf{s}_{s,s'} f_{s'}$ to H_{imp}, where μ_0 is the effective Bohr magneton and $\mathbf{s}$ is the vector of Pauli matrices. In practice, only the z component of the field will enter any relevant equations so we restrict to that direction. Writing it out explicitly, Eq. (C.3) with a magnetic field is

$$\begin{aligned} E_0\left(|b_0|^2 + {\sum_{\ell,s}}'|B_{\ell,s}|^2\right) \;+\; {\sum_{\ell,s}}'(\varepsilon_0 - \mu_0 h_z s - E_{\ell,s}) + \frac{1}{\sqrt{N_M}}{\sum_{\ell,s}}'\left(v_{\ell,s}B_{\ell,s}b_0^\star + v^\star_{\ell,s}B^\star_{\ell,s}b_0\right) \\ = \;(E_0 + \varepsilon_0 + \epsilon)\left(|b_0|^2 + {\sum_{\ell,s}}'|B_{\ell,s}|^2\right) \end{aligned} \tag{C.4}$$

where again we write the sum over occupied states ${\sum_{\ell,s}}'$. Recall the number of metal atoms (also the number of unit cells) N_M. Next, we differentiate with respect to $b_0^\star$ and $B^\star_{\ell,s}$, and we write the normalization explicitly, giving

$$(\varepsilon_0 + \epsilon)\, b_0 = \frac{1}{\sqrt{N_M}}{\sum_{\ell,s}}' v_{\ell,s}B_{\ell,s} \tag{C.5}$$

$$(\epsilon + \mu_0 h_z s + E_{\ell,s} - \mu)\, B_{\ell,s} = \frac{1}{\sqrt{N_M}} v^\star_{\ell,s} b_0 \tag{C.6}$$

$$|b_0|^2 + {\sum_{\ell,s}}'|B_{\ell,s}|^2 = 1\,. \tag{C.7}$$

This set of three equations can now be used to determine all three objects b_0, $B_{\ell,s}$, and the shift ϵ. The second line, Eq. (C.6), can be implemented in the first, Eq. (C.5), which gives (assuming $b_0 \neq 0$) the solution for the shift, Eq. (3.19). By putting Eq. (C.6) into Eq. (C.7), the Fermi sea parameter is obtained giving Eq. (3.20). Lastly, the singlet/triplet parameters are found using $B_{\ell,s}$ directly from Eq. (C.6).

C.2 Spin and Susceptibility

Here we explain the calculations behind Sec. 3.3.2. The total spin is the sum of impurity and TMD spin, $\mathbf{J} = \mathbf{S} + \boldsymbol{\sigma}$, with $\mathbf{S} = (1/2)\sum_{s,s'} f_s^\dagger \mathbf{s}_{s,s'} f_{s'}$ for the impurity. To get spin for the TMD, the operators must be properly projected from the plain basis states of Sec. 3.2.2. the localized (Wannier) states created by the operators $a^\dagger_{\alpha,\tau,s}(\mathbf{r})$, to the eigenstates $c^\dagger_{n,\mathbf{k},\tau,s}$. Normally this is a trivial step, but it is important in the case of spin-split bands. The starting point is the spin operator in the trivial basis,

$$\boldsymbol{\sigma} = \frac{1}{2}\sum_{\alpha,\mathbf{r},\tau,s} a^\dagger_{\alpha,\tau,s}(\mathbf{r})\mathbf{s}_{s,s'}a_{\alpha,\tau,s'}(\mathbf{r}) \; . \tag{C.8}$$

Then we project to the eigen-basis, i.e.

$$a_{\alpha,\tau,s}(\mathbf{r}) = \frac{1}{\sqrt{N_M}}\sum_{n,\mathbf{k}} U_{\alpha,n}(\mathbf{k},\tau,s)c_{n,\mathbf{k},\tau,s}\mathrm{e}^{i\mathbf{k}\cdot\mathbf{r}} \; . \tag{C.9}$$

The spin operator now involves products of the matrices[1] $U = M \cdot N$ for different spin indices, so we define

$$K_{n,n'}(k,\tau,s) = \sum_\alpha N^\dagger_{n,\alpha}(k,\tau,s)N_{\alpha,n'}(k,\tau,-s) \; . \tag{C.10}$$

[1] See Eq. (3.11) for a reminder of these matrices.

The spin being the same leads to an identity matrix, so the corresponding definition is not required. Then, the spin operator components are given by

$$\sigma_j = \frac{1}{2} \sum_{n,n',\mathbf{k},\tau,s,s'} \begin{cases} \delta_{n',n}\delta_{s',s}\, s\, c^\dagger_{n,\mathbf{k},\tau,s} c_{n,\mathbf{k},\tau,s} & , \quad j = z \\ \delta_{s',-s}(s_j)_{s,-s}\, K_{n,n'}(k,\tau,s) c^\dagger_{n,\mathbf{k},\tau,s} c_{n',\mathbf{k},\tau,-s} & , \quad j = x, y\ . \end{cases} \tag{C.11}$$

The form of Eq. (C.11) is crucial to the discussion of Sec. 3.3.2 but it is due to the fact that the valleys are treated independently, not really the involvement of the K matrix. The spin expectations of $|\psi_0\rangle$, $|\psi\rangle$, and other many-body states in this work are easily calculated using the above eigenspace operators[2], the transverse (x, y) directions giving zero by construction for states conserving particle number. The result for the z direction spin in the Kondo state (without photoexcitation) is given in Eq. (3.23), resulting in $J_z = 0$ after cancelling with the impurity spin. Without a magnetic field, we find that the spin of the impurity S_z and of the band σ_z are independently zero, showing the impurity itself is already nonmagnetic.

In the computation of $\langle J^2 \rangle$, or specifically the band part $\langle \sigma^2 \rangle$, it is helpful to use particle/hole operators with respect to some effective vacuum state, here the Fermi sea $|\psi_0\rangle$. In other words, we transform using

$$c_{n,\mathbf{k},\tau,s} \to \begin{cases} p_{n,\mathbf{k},\tau,s} & , \quad E_{n,k,\tau,s} > \mu \\ h^\dagger_{n,\mathbf{k},\tau,s} & , \quad E_{n,k,\tau,s} \leq \mu \end{cases} \tag{C.12}$$

and its hermitian conjugate. In the case of the photoexcited system, the above is also depenent on spin since the chemical potentials are shifted and the transformations are

[2]Calculations such as these with a second-quantized many-body state in Fock space are standard theoretical techniques; see Ref.s [79–81].

much more involved. Using the square of Eq. (C.11) and the above transformation for the more typical state $|\psi\rangle$, we get for the total spin

$$\begin{aligned}\langle J^2\rangle &= \frac{1}{2}{\sum_{\mathbf{k},\tau,s}}' \left[|B_{-,\mathbf{k},\tau,s}|^2 \left(1-|K_{-,+}(k,\tau,s)|^2+|K_{-,-}(k,\tau,s)|^2\right)\right. \\ &- \left. 2\, B_{-,\mathbf{k},\tau,s}B^{\star}_{-,\mathbf{k},\tau,-s}K_{-,-}(k,\tau,s)\right] - \frac{1}{2}{\sum_{\mathbf{k},\tau,s}}^{\text{un.}} \delta_{\tau,-s}|B_{-,\mathbf{k},\tau,s}|^2|K_{-,-}(k,\tau,s)|^2 \quad \text{(C.13)}\end{aligned}$$

where we have also subtracted the band contribution $\langle\psi_0|\,\boldsymbol{\sigma}^2\,|\psi_0\rangle$, and we denote the sum over unoccupied states in the valence band $\sum^{\text{un.}}$. This result is identical to Eq. (3.25), which appears after simplifying the K matrix elements and substituting the singlet/triplet parameters p_ℓ and t_ℓ.

To conclude this appendix, we discuss the calculation of the susceptibility. There are two approaches, which of course give the same result. First, one can use the spin expectation for the impurity,

$$\langle S_z\rangle = {\sum_{\mathbf{k},\tau,s}}' s|B_{-,\mathbf{k},\tau,s}|^2 = {\sum_{\mathbf{k},\tau}}' \left(|B_{-,\mathbf{k},\tau,\uparrow}|^2-|B_{-,\mathbf{k},\tau,\downarrow}|^2\right) \quad \text{(C.14)}$$

with the parameters at finite magnetic field as from Eq. (C.6). It is a simple matter to take the magnetization of the impurity as $m_z = \mu_0\langle S_z\rangle$ where again we use μ_0 for the effective Bohr magneton. The transverse x, y directions are always zero and as seen above those components of the magnetic field do not appear in the variational solutions, so the susceptibility tensor is zero except for a single element, easily obtained with

$$\chi^{imp.}_{zz}(h_z) = \frac{d}{dh_z}m_z = \mu_0^2\frac{d}{d(\mu_0 h_z)}\langle S_z\rangle \ . \quad \text{(C.15)}$$

Evaluating at zero field, this reduces to Eq. (3.27).

The other approach relies on the energy shift ϵ. The susceptibility here is found by writing Eq. (3.19) with the inclusion of a field, then differentiating both sides with respect

to h_z. From thermodynamics, we know the first derivative gives the magnetization and the second gives the susceptibility:

$$\chi_{zz}^{imp.}(h_z) = \frac{d}{dh_z} m_z = -\frac{d^2}{dh_z^2}\epsilon \, . \tag{C.16}$$

The derivatives are easily calculated by using implicit differentiation in Eq. (3.19), and at zero field we again obtain the same result, Eq. (3.27).

Appendix D

Details of NRG Projections & Convergence

Here we expand upon the construction of the linear chain originating from the Anderson Hamiltonian, Eq. (3.34), and we mention some details concerning general convergence of the procedure. The chain basis is central to the NRG method, and its construction includes the primary approximation of NRG. The chain pertains only to the bath (TMD) electrons, but the zeroth site starting point is motivated by the state hybridizing with the impurity. As described in Sec. 3.4.1, the chain is constructed in two main steps. First, energy space is discretized into logarithmic intervals approaching the chemical potential; this is where the approximation is made. Second, the discretized states are superposed to form states orthogonal to the zeroth site, the state coupled to the impurity; this process inevitably leads to departure from a diagonal basis so it is termed "tridiagonalization".

D.1 Logarithmic Discretization

In this section we fill in the steps between equations (3.34) and (3.37). There we noted that the positive and negative energies are discretized separately, with their own operators $a^\dagger$ and $b^\dagger$, respectively[39]. Specifically, we have

$$a^\dagger_{n,p,s} = \int_{-\ell_s}^{e_s} d\xi\, \psi^+_{n,p,s}(\xi) c^\dagger_{\xi,s} \tag{D.1}$$

$$b^\dagger_{n,p,s} = \int_{-\ell_s}^{e_s} d\xi\, \psi^-_{n,p,s}(\xi) c^\dagger_{\xi,s} \tag{D.2}$$

where the Fourier components $\psi^\pm_{n,p,s}(\xi)$ are broken down by logarithmic intervals labeled with $n = 0, 1, 2, ...$ The intervals are as given by (3.36), and the Fourer components are

$$\psi^+_{n,p,s}(\xi) = \left[\frac{R^n}{e_s\,(1-R^{-1})}\right]^{1/2} \mathrm{e}^{i\omega^+_{n,s}p\xi} \quad , \text{ for } \; e_s R^{-(n+1)} < \xi < e_s R^{-n}\,; \tag{D.3}$$

$$\psi^-_{n,p,s}(\xi) = \left[\frac{R^n}{\ell_s\,(1-R^{-1})}\right]^{1/2} \mathrm{e}^{-i\omega^-_{n,s}p\xi} \quad , \text{ for } \; -\ell_s R^{-n} < \xi < -\ell_s R^{-(n+1)} \tag{D.4}$$

with fundamental frequencies $\omega^+_{n,s} = 2\pi R^n/e_s(1-R^{-1})$, $\omega^-_{n,s} = 2\pi R^n/\ell_s(1-R^{-1})$, and integral harmonic index $p \in (-\infty, \infty)$. The components $\psi^\pm$ are zero when the energy ξ lies outside the respective n^{th} intervals on the r.h.s. above. We now have a properly orthonormalized complete set of states which can be related back,

$$c^\dagger_{\xi,s} = \sum_{n,p} \left[\left(\psi^+_{n,p,s}(\xi)\right)^\star a^\dagger_{n,p,s} + \left(\psi^-_{n,p,s}(\xi)\right)^\star b^\dagger_{n,p,s} \right] \tag{D.5}$$

leading to a form preceding Eq. (3.37), for the bath electrons only,

$$\begin{aligned} \int_{-\ell_s}^{e_s} d\xi\, \xi c^\dagger_{\xi,s} c_{\xi,s} &= \frac{1+R^{-1}}{2} \sum_{n,p} \left(e_s R^{-n} a^\dagger_{n,p,s} a_{n,p,s} - \ell_s R^{-n} b^\dagger_{n,p,s} b_{n,p,s} \right) \\ &+ \frac{1-R^{-1}}{2\pi i} \sum_{n,p'\neq p} \left[\frac{R^{-n}}{p'-p} \mathrm{e}^{2\pi i(p'-p)} \left(e_s a^\dagger_{n,p,s} a_{n,p',s} - \ell_s b^\dagger_{n,p,s} b_{n,p',s} \right) \right]. \end{aligned} \tag{D.6}$$

The bath Hamiltonian is diagonal in the original basis $c^\dagger_{\xi,s}$, so changing away from it will inevitably lead to off-diagonal terms like those in the final sum above. Notice, however, that the off-diagonal sum comes with a factor $\propto 1 - R^{-1}$ so it vanishes as the discretization factor R approaches unity (i.e. as continuity is restored). In our work, we have used $R = 3$ so the factor is in fact $\propto 2/3$. Nevertheless we follow others[39] and make the *crucial approximation* of using only harmonic index $p = 0$, killing the off-diagonal sum. The components (D.3) are now constants (of varying magnitude) in each energy interval; in other words the states created by $a^\dagger_{n,0,s}$ and $b^\dagger_{n,0,s}$ are simple (normalized) averages of the states $c^\dagger_{\xi,s}$ on the appropriate intervals of energy ξ. Thus the approximation of retaining only these states is equivalent to diregarding fluctuations across individual energy intervals, only allowing changes across interval boundaries. Since phase changes like the Kondo effect are known to exhibit changes across the entire energy space (and physical space) together, Wilson's approximation of taking only the constant $p = 0$ contribution is justified, and the extensive history and success of NRG provide further credence to it. Upon ignoring all states with $p \neq 0$, we obtain the expression in Eq. (3.37).

D.2 Tridiagonalization

We continue to develop the NRG chain, now proceeding from Eq. (3.37) to (3.40). Recall (or see Eq. (3.39)) that the zeroth site $d^\dagger_{0,s}$ is the starting point, and is defined as the state which couples to the impurity via H_V. We wish to create other states which are orthogonal to the zeroth site (and to each other) in such a way that nothing further than nearest-neighbor hoppings appear in the final chain Hamiltonian, the first line of Eq. (3.40). For

the purposes of this section we use H_c to denote the $p = 0$ bath Hamiltonian, the first sum of Eq. (D.6) above or the first line of Eq. (3.37), which will become the chain Hamiltonian.

Constructing the chain states $d^\dagger_{m,s}$ with $m > 0$ involves a Graham-Schmidt orthogonalization procedure starting from the zeroth site, specifically the Lanczos algorithm[34, 41, 66]. Dropping the spin label for now, we write very generally our goal. We seek a transformation, a set of $\{u_{m,n}, v_{m,n}\}$ with $m, n = 0, 1, 2, ...$ describing the relation $d^\dagger_m = \sum_n \left(u_{m,n} a^\dagger_n + v_{m,n} b^\dagger_n\right)$, such that the resultant states are assigned some energies ϵ_m and hoppings t_m leading to the tridiagonal form (3.40). We are given the starting point (using spin labels where appropriate) of

$$u_{0,n} = \left(\frac{e_s(1 - R^{-1})}{1 + e_0/D}\right)^{1/2} R^{-n/2} \tag{D.7}$$

$$v_{0,n} = \left(\frac{\ell_s}{e_s}\right)^{1/2} u_{0,n} \tag{D.8}$$

from the definition of the zeroth site, Eq. (3.39). To develop further sites, denote the zeroth state $|0\rangle = d^\dagger_0 |vac.\rangle$. The energy of this state may be easily found with $\epsilon_0 = \langle 0| H_c |0\rangle$. The next site is then given by

$$|1\rangle = \frac{1}{t_0} \left(H_c |0\rangle - |0\rangle \langle 0| H_c |0\rangle\right) \tag{D.9}$$

which is automatically orthogonal to $|0\rangle$ and whose normalization constant t_0 is actually the same as the hopping $\langle 1| H_c |0\rangle$. In this case the hopping (squared) is also the same as the variance in energy, $t_0^2 = \langle 0| H_c^2 |0\rangle - \langle 0| H_c |0\rangle^2$, so that we have the zeroth site energy and its hopping to site $m = 1$. For the energy of the new site, we get $\epsilon_1 = \langle 1| H_c |1\rangle = (\langle 0| H_c^3 |0\rangle - 2\epsilon_0 \langle 0| H_c^2 |0\rangle + \epsilon_0^3)/t_0^2$. One can see that, in constructing many sites, we will need arbitrary powers $\langle 0| H_c^P |0\rangle$, but every quantity can be fully given in terms of the starting

point values (D.7) and (D.8). Continuing, the next site $m = 2$ is given by

$$|2\rangle = \frac{1}{t_1}\left(H_c\,|1\rangle - |1\rangle\,\langle 1|\,H_c\,|1\rangle - |0\rangle\,\langle 0|\,H_c\,|1\rangle\right) \tag{D.10}$$

$$= \frac{1}{t_1}\left(H_c\,|1\rangle - |1\rangle\,\epsilon_1 - |0\rangle\,t_0\right) \tag{D.11}$$

which is orthogonal to both previous sites $m = 0, 1$. Importantly, one can check that the above state does not connect to the zeroth site: $\langle 2|\,H_c\,|0\rangle = 0$. This is the key point that keeps the Hamiltonian H_c tridiagonal instead of having arbitrarily off-diagonal pieces. One may now write ϵ_2 and t_1, but they will be messier and involve larger powers of H_c in the zeroth state. Instead we now move to the general site m,

$$|m+1\rangle = \frac{1}{t_m}\left(H_c\,|m\rangle - |m\rangle\,\epsilon_m - |m-1\rangle\,t_{m-1}\right). \tag{D.12}$$

With the above, and the definitions $\epsilon_m = \langle m|\,H_c\,|m\rangle$ and $t_{m-1} = \langle m-1|\,H_c\,|m\rangle$, we can write a set of recursion equations which determines the tridiagonal transformation:

$$t_m^2 = \left(\frac{1+R^{-1}}{2}\right)^2 \sum_{n=0}^{\infty}\left[|u_{m,n}|^2(e_sR^{-n})^2 + |v_{m,n}|^2(\ell_sR^{-n})^2\right] - \epsilon_m^2 - t_{m-1}^2 \tag{D.13}$$

$$\epsilon_m = \frac{1+R^{-1}}{2}\sum_{n=0}^{\infty}\left[|u_{m,n}|^2(e_sR^{-n}) - |v_{m,n}|^2(\ell_sR^{-n})\right] \tag{D.14}$$

$$u_{m+1,n} = \frac{1}{t_m}\left[\left(\frac{1+R^{-1}}{2}e_sR^{-n} - \epsilon_m\right)u_{m,n} - t_{m-1}u_{m-1,n}\right] \tag{D.15}$$

$$v_{m+1,n} = -\frac{1}{t_m}\left[\left(\frac{1+R^{-1}}{2}\ell_sR^{-n} + \epsilon_m\right)v_{m,n} + t_{m-1}v_{m-1,n}\right]. \tag{D.16}$$

The above equations are consistent with those of Section II C of Ref. [66]. They are valid for all sites, $m \geq 0$, as long as one takes $t_{-1} \to 0$. For the symmtric Anderson model, the site energies ϵ_m are zero and Wilson has constructed[38] an analytic solution for the hoppings t_m. When the chemical potential is placed asymmetrically in a band the

site energies are no longer zero, and the energies and hoppings must generally be determined numerically. For the sake of numerics, it can be useful to neglect the above form (which involves infinite sums) and instead use the equivalent relations for powers, i.e. for $\langle m| H_c^P |m+1\rangle$ and $\langle m+1| H_c^P |m+1\rangle$. The energies and hoppings are then obtained with $P = 1$. Either way, one can numerically calculate the tridiagonal chain parameters up to any arbitrary chain length by iterating a set of equations like (D.13)-(D.16). We always have at least one label other than site index, spin, so the procedure must be repeated for both spin up and down, at least when any spin dependence is involved. If there is more than one channel coupled to the impurity, that is if one effectively has multiple chains, then of course the procedure must be repeated for each of those as well.

D.3 Convergence

In this section we look at the convergence of the iterative diagonalization procedure. The main tools for establishing the fixed points and stability of the NRG procedure are the plots of energy spectra against the number of sites included, with even and odd sites separated. The lowest-lying energies are labeled with the corresponding subspaces so that they may be tracked easily. For our choice $R = 3$, we generally observe good convergence by $M \sim 30$. In order for the system to converge at all, it is necessary to use enough states that each iteration is accurately described, around 400-425 states for this work (as remarked in Sec. 3.4.2).

To begin, we look at the unexcited system with $\delta = 0$. Looking at the left part of Fig. D.1 it is clear that the states with equal but opposite spin J_z are degenerate, as

expected for the unexcited case. In fact, due to its simplicity this NRG procedure should appear like a rather conventional metal with an impurity level in the "mixed valence" regime, just below the chemical potential.

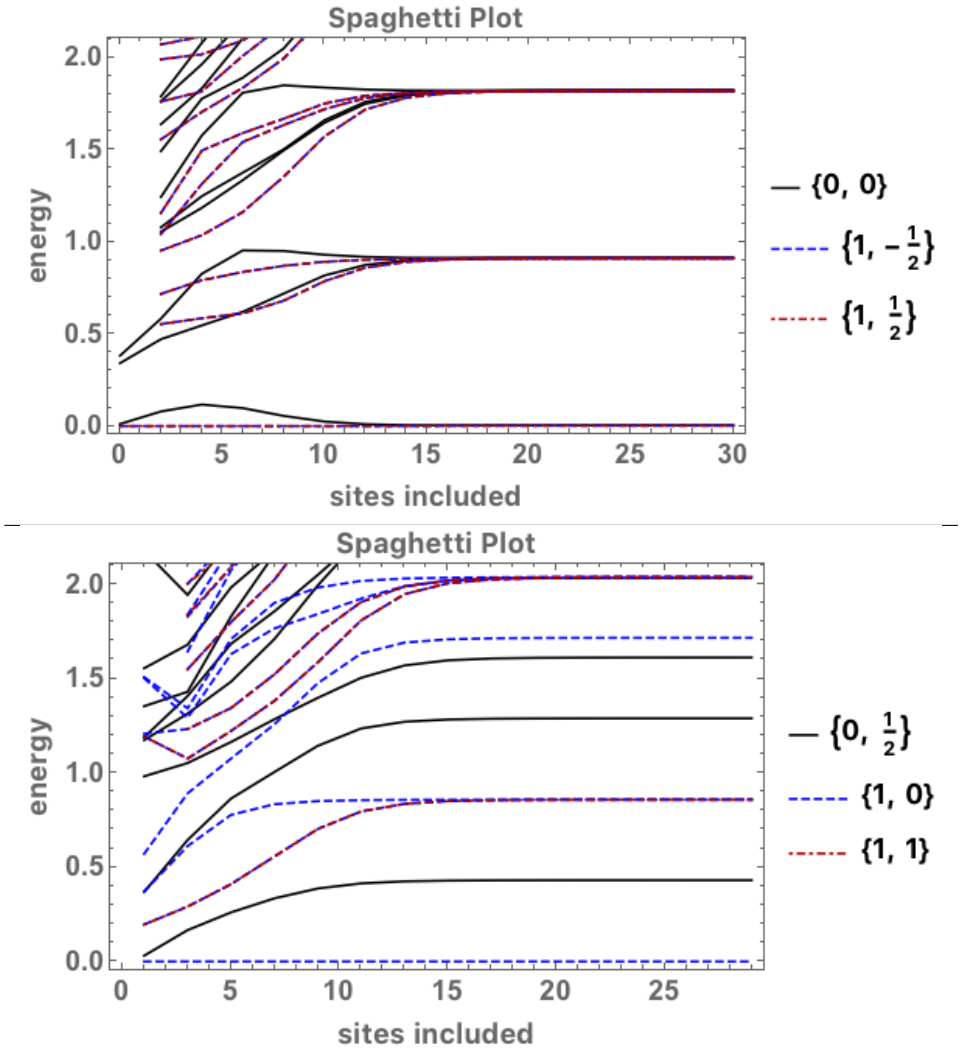


Figure D.1: Energy levels relative to the ground state for even (top) and odd (bottom) chain lengths, for the unexcited system $\delta = 0$. The spectrum is certainly stable after going up to site $M = 30$. The subspace labels appearing in legends are $\{Q, J_z\}$.

Next we consider the offset case $\delta = \lambda/5 > 0$. From Fig. D.2, the system clearly converges very quickly, even faster than the equilibrium case. The only real difference in

the structure of the energy levels is that the levels are split for different J_z, leading to a more complex structure overall. The levels stabilize very quickly, by $M = 10$, but they do not join together as in typical cases like the above Fig. D.1.

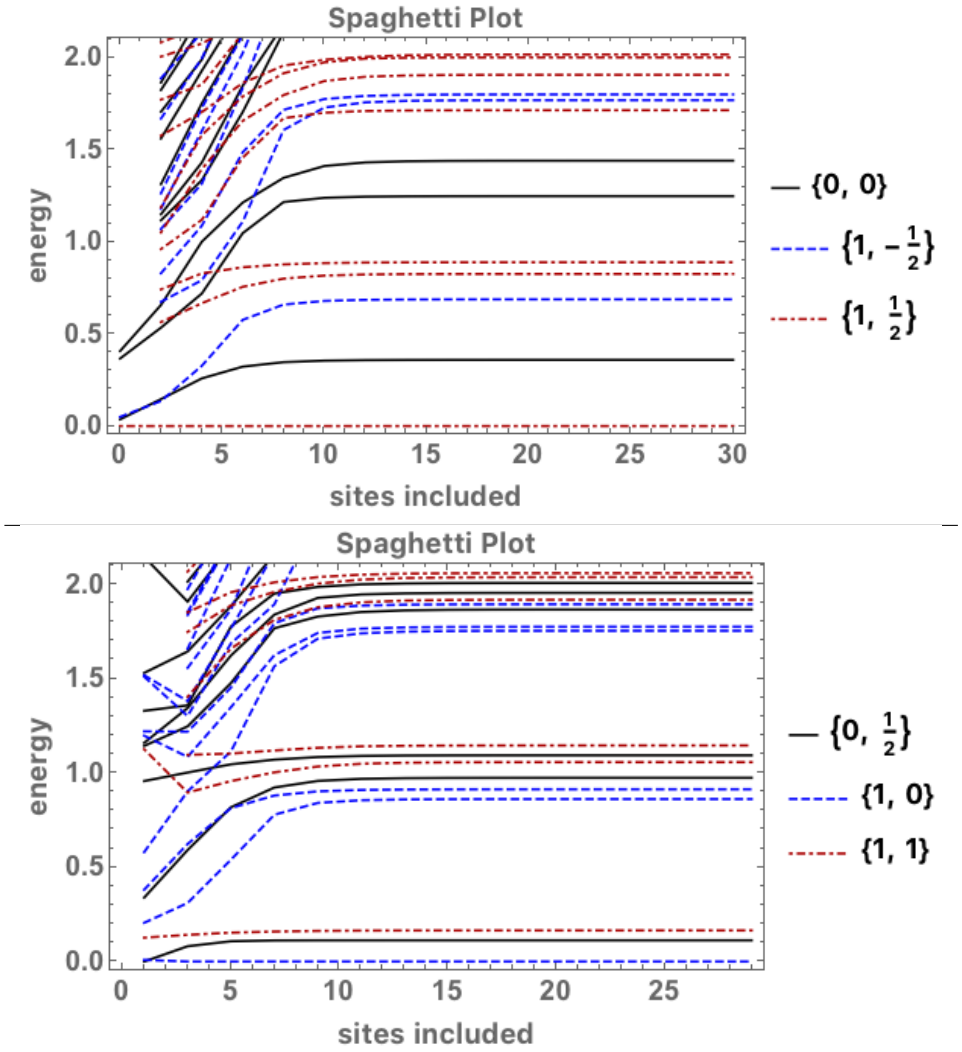


Figure D.2: Energy levels relative to the ground state for even (top) and odd (bottom) chain lengths, for the excited system $\delta > 0$. The spin values clearly split energy levels, giving this case much more structure. Interestingly, the system seems to stabilize more quickly, near site $M = 10$.

Bibliography

[1] M. Phillips and V. Aji, "Tunable line node semimetals", Physical Review B **90**, 115111 (2014), doi: https://dx.doi.org/10.1103/PhysRevB.90.115111.

[2] A. A. Burkov and L. Balents, "Weyl semimetal in a topological insulator multilayer", Physical Review Letters **107**, 127205 (2011).

[3] "The 2016 Nobel Prize in Physics - Press Release", (2016), URL http://www.nobelprize.org/nobel_prizes/physics/laureates/2016/press.html.

[4] N. D. Mermin, "The topological theory of defects in ordered media", Reviews of Modern Physics **51**(3), 591 (1979).

[5] D. J. Thouless, M. Kohmoto, M. P. Nightingale, and M. den Nijs, "Quantized Hall conductance in a two-dimensional periodic potential", Physical Review Letters **49**(6), 405 (1982).

[6] Q. Niu, D. J. Thouless, and Y.-S. Wu, "Quantized Hall conductance as a topological invariant", Physical Review B **31**(6), 3372 (1985).

[7] M. V. Berry, "Quantal phase factors accompanying adiabatic changes", Proceedings of the Royal Society of London, Series A **392**, 45–57 (1984).

[8] J. Zak, "Berry's phase for energy bands in solids", Physical Review Letters **62**(23), 2747 (1989).

[9] F. D. M. Haldane, "Model for a quantum Hall effect without Landau levels: Condensed-matter realization of the "parity anomaly"", Physical Review Letters **61**(18), 2015–2018 (1988).

[10] C. L. Kane and E. J. Mele, "Z_2 topological order and the quantum spin Hall effect", Physical Review Letters **95**(14), 146802 (2005).

[11] H. Zhang, C.-X. Liu, X.-L. Qi, X. Dai, Z. Fang, and S.-C. Zhang, "Topological insulators in Bi", Nature Physics **5**, 438–442 (2009).

[12] M. Konig, S. Wiedmann, C. Brune, A. Roth, H. Buhmann, L. W. Molenkamp, X.-L. Qi, and S.-C. Zhang, "Quantum spin Hall insulator state in HgTe quantum wells", Science **318**(5851), 766–770 (2007).

[13] J. C. Y. Teo, L. Fu, and C. L. Kane, "Surface states and topological invariants in three-dimensional topological insulators: Application to $Bi_{1-x}Sb_x$", Physical Review B **78**(4), 045426 (2008).

[14] X.-L. Qi and S.-C. Zhang, "Topological insulators and superconductors", Reviews of Modern Physics **83**, 1057–1110 (2011).

[15] L. Fu and C. L. Kane, "Superconducting proximity effect and Majorana Fermions at the surface of a topological insulator", Physical Review Letters **100**(9), 096407 (2008).

[16] C. Xu and J. E. Moore, "Stability of the quantum spin Hall effect: Effects of interactions, disorder, and Z_2 topology", Physical Review B **73**, 045322 (2006).

[17] L. Fu, C. L. Kane, and E. J. Mele, "Topological insulators in three dimensions", Physical Review Letters **98**(10), 106803 (2007).

[18] R. Roy, "Topological phases and the quantum spin Hall effect in three dimensions", Physical Review B **79**(19), 195322 (2009).

[19] J. E. Moore and L. Balents, "Topological invariants of time-reversal-invariant band structures", Physical Review B **75**(12), 121306 (2007).

[20] J. Sinova, D. Culcer, Q. Niu, N. A. Sinitsyn, T. Jungwirth, and A. H. MacDonald, "Universal intrinsic spin Hall effect", Physical Review Letters **92**(12), 126603 (2004).

[21] J. Sinova, S. O. Valenzuela, J. Wunderlich, C. H. Back, and T. Jungwirth, "Spin Hall effects", Reviews of Modern Physics **87**, 1213 (2015).

[22] W.-Y. Shan, H.-Z. Lu, and D. Xiao, "Spin Hall effect in spin-valley coupled monolayers of transition metal dichalcogenides", Physical Review B **88**, 125301 (2013).

[23] H. B. Nielsen and N. Ninomiya, "Absence of neutrinos on a lattice (I). proof by homotopy theory", Nuclear Physics B **185**, 20 (1981).

[24] H. B. Nielsen and N. Ninomiya, "Absence of neutrinos on a lattice (II). intuitive topological proof", Nuclear Physics B **193**, 173 (1981).

[25] A. A. Burkov, M. D. Hook, and L. Balents, "Topological Nodal Semimetals", Physical Review B **84**, 235126 (2011).

[26] X. Wan, A. M. Turner, A. Vishwanath, and S. Y. Savrasov, "Topological semimetal and Fermi-arc surface states in the electronic structure of pyrochlore iridates", Physical Review B **83**, 205101 (2011).

[27] D. Xiao, W. Yao, and Q. Niu, "Valley-contrasting physics in graphene: Magnetic moment and topological transport", Physical Review Letters **99**, 236809 (2007).

[28] G.-B. Liu, W.-Y. Shan, Y. Yao, W. Yao, and D. Xiao, "Three-band tight-binding model for monolayers of group-VIB transition metal dichalcogenides", Physical Review B **88**, 085433 (2013).

[29] D. Xiao, G.-B. Liu, W. Feng, X. Xu, and W. Yao, "Coupled spin and valley physics in monolayers of MoS_2 and other group-VI dichalcogenides", Physical Review Letters **108**, 1096802 (2012).

[30] G.-B. Liu, D. Xiao, Y. Yao, X. Xu, and W. Yao, "Electronic structures and theoretical modelling of two-dimensional group-vib transition metal dichalcogenides", Chemical Society Reviews **44**, 2643 (2015).

[31] W. Yao, D. Xiao, and Q. Niu, "Valley-dependent optoelectronics from inversion symmetry breaking", Physical Review B **77**, 235406 (2008).

[32] P. W. Anderson, "Localized magnetic states in metals", Physical Review **124**(1), 41 (1961).

[33] J. R. Schrieffer and P. A. Wolff, "Relation between the Anderson and Kondo Hamiltonians", Physical Review **149**(2), 491 (1966).

[34] A. C. Hewson, *The Kondo Problem to Heavy Fermions*, (Cambridge University Press, 1997).

[35] J. Kondo, "Resistance minimum in dilute magnetic alloys", Progress of Theoretical Physics **32**, 37 (1964).

[36] K. Yosida, "Bound state due to the s-d exchange interaction", Physical Review **147**(1), 223 (1966).

[37] C. M. Varma and Y. Yafet, "Magnetic susceptibility of mixed-valence rare-earth compounds", Physical Review B **13**(7), 2950 (1976).

[38] K. G. Wilson, "The renormalization group: Critical phenomena and the Kondo problem", Reviews of Modern Physics **47**(4), 773 (1975).

[39] H. R. Krishna-murthy, J. W. Wilkins, and K. G. Wilson, "Renormalization-group approach to the anderson model of dilute magnetic alloys. I. static properties for the symmetric case", Physical Review B **21**(3), 1003 (1980).

[40] H. R. Krishna-murthy, J. W. Wilkins, and K. G. Wilson, "Renormalization-group approach to the anderson model of dilute magnetic alloys. II. static properties for the asymmetric case", Physical Review B **21**(3), 1044 (1980).

[41] T. A. Costi, "Numerical renormalization group and multi-orbital Kondo physics", Modeling and Simulation **5** (2015).

[42] R. Bulla, T. A. Costi, and D. Vollhardt, "Finite-temperature numerical renormalization group study of the Mott transition", Physical Review B **64**, 045103 (2001).

[43] H. Weyl, "Elektron and gravitation. I", Zeitschrift for Physik A Hadrons and Nuclei **56**, 330–352 (1929).

[44] Z. Wang, Y. Sun, X.-Q. Chen, C. Franchini, G. Xu, H. Weng, X. Dai, and Z. Fang, "Dirac semimetal and topological phase transitions in A_3 Bi (A=Na, K, Rb)", Physical Review B **85**, 195320 (2012).

[45] Z. K. Liu, B. Zhou, Z. J. Wang, H. M. Weng, D. Prabhakaran, S.-K. Mo, Y. Zhang, Z. X. Shen, Z. Fang, X. Dai, Z. Hussain, and Y. L. Chen, "Discovery of a three-dimensional topological Dirac semimetal, Na_3Bi", Science **343**(6173), 864–867 (2014).

[46] Z. Wang, H. Weng, X. D. Q. Wu, and Z. Fand, "Three-dimensional Dirac semimetal and quantum transport in Cd_3As_2", Physical Review B **88**, 125427 (2013).

[47] S. Borisenko, Q. Gibson, D. Evtushinsky, V. Zabolotnyy, B. Beuchner, and R. Cava, "Experimental realization of a three-dimensional Dirac semimetal", Physical Review Letters **113**, 027603 (2014).

[48] M. Neupane, S. Xu, R. Sankar, N. Alidoust, G. Bian, C. Liu, I. Belopolski, T.-R. Chang, H.-T. Jeng, H. Lin, A. Bamsil, F. Chou, and M. Z. Hasan, "Observation of a three-dimensional topological Dirac semimetal phase in high-mobility Cd_3As_2", Nature Communications **5**(3786) (2014).

[49] N. W. Ashcroft and N. D. Mermin, *Solid State Physics*, (Brooks/Cole, 1976).

[50] X.-L. Qi, R. Li, J. Zang, and S.-C. Zhang, "Inducing a magnetic monopole with topological surface states", Science **323**(5918), 1184–1187 (2009).

[51] R. Li, J. Wang, X.-L. Qi, and S.-C. Zhang, "Dynamical axion field in topological magnetic insulators", Nature Physics **6**, 284 (2010).

[52] G. Rosenberg and M. Franz, "Witten effect in a crystalline topological insulator", Physical Review B **82**, 035105 (2010).

[53] W. Luo and X.-L. Qi, "Massive Dirac surface states in topological insulator/magnetic insulator heterostructures", Physical Review B **87**, 085431 (2013).

[54] P. Wei, F. Katmis, B. A. Assaf, H. Steinberg, PabloJarillo-Herrero, D. Heiman, and J. S. Moodera, "Exchange-coupling-induced symmetry breaking in topological insulators", Physical Review Letters **110**, 186807 (2013).

[55] A. G. Swartz, P. M. Odenthal, Y. Hao, R. S. Ruoff, and R. K. Kawakami, "Integration of the ferromagnetic insulator EuO onto graphene", ACS Nano **6**(11), 10063–10069 (2012).

[56] V. Carteaux, D. Brunet, G. Ouvrard, and G. Andre, "Crystallographic, magnetic and electronic structures of a new layered ferromagnetic compound $Cr_2Ge_2Te_6$", Journal of Physics: Condensed Matter **7**(1), 69 (1995).

[57] H. Ji, R. A. Stokes, L. D. Alegria, E. C. Blomberg, M. A. Tanatar, A. Reijnders, L. M. Schoop, T. Liang, R. Prozorov, K. S. Burch, N. P. Ong, J. R. Petta, and R. J. Cava, "A ferromagnetic insulating substrate for the epitaxial growth of topological insulators", Journal of Applied Physics **114**, 114907 (2013).

[58] C.-Z. Chang, J. Zhang, X. Feng, J. Shen, Z. Zhang, M. Guo, K. Li, Y. Ou, P. Wei, L.-L. Wang, Z.-Q. Ji, Y. Feng, S. Ji, X. Chen, J. Jia, X. Dai, Z. Fang, S.-C. Zhang, K. He, Y. Wang, L. Lu, X.-C. Ma, and Q.-K. Xue, "Experimental observation of the quantum anomolous Hall effect in a magnetic topological insulator", Science **340**(6129), 167–170 (2013).

[59] K. F. Mak, C. Lee, J. Hone, J. Shan, and T. F. Heinz, "Atomically thin MoS_2: a new direct-gap semiconductor", Physical Review Letters **105**, 136805 (2010).

[60] K. F. Mak, K. He, J. Shan, and T. F. Heinz, "Control of valley polarization in monolayer MoS_2 by optical helicity", Nature Nanotechnology **7**, 494 (2012).

[61] Z. Y. Zhu, Y. C. Cheng, and U. Schwingenschlögl, "Giant spin-orbit-induced spin splitting in two-dimensional transition-metal dichalcogenide semiconductors", Physical Review B **84**, 153402 (2011).

[62] D. Xiao, M.-C. Chang, and Q. Niu, "Berry phase effects on electronic properties", Reviews of Modern Physics **82**, 1959 (2010).

[63] M.-C. Chang and Q. Niu, "Berry phase, hyperorbits, and the Hofstadter spectrum: Semiclassical dynamics in magnetic Bloch bands", Physical Review B **53**(11), 7010 (1996).

[64] J. S. Ross, P. Klement, A. M. Jones, N. J. Ghimire, J. Yan, D. G. Mandrus, T. Taniguchi, K. Watanabe, K. Kitamura, W. Yao, D. H. Cobden, and X. Xu, "Electrically tunable excitonic light-emitting diodes based on monolayer WSe_2 p-n junctions", Nature Nanotechnology **9**, 268 (2014).

[65] K. F. Mak, K. L. McGill, J. Park, and P. L. McEuen, "The valley Hall effect in MoS_2 transistors", Science **344**(6191), 1489 (2014).

[66] R. Bulla, T. A. Costi, and T. Pruschke, "Numerical renormalization group method for quantum impurity systems", Reviews of Modern Physics **80**, 395 (2008).

[67] B. Uchoa, T. G. Rappoport, and A. H. C. Neto, "Kondo quantum criticality of magnetic adatoms in graphene", Physical Review Letters **106**, 016801 (2011).

[68] S.-P. Chao and V. Aji, "Kondo and charge fluctuation resistivity due to Anderson impurities in graphene", Physical Review B **83**, 165449 (2011).

[69] R. Zitko, "Quantum impurity on the surface of a topological insulator", Physical Review B **81**, 241414 (2010).

[70] V. Aji, C. M. Varma, and I. Vekhter, "Kondo effect in an antiferromagnetic metal: Renormalization group analysis and a variational calculation", Physical Review B **77**, 224426 (2008).

[71] L. Isaev, D. F. Agterberg, and I. Vekhter, "Kondo effect in the presence of spin-orbit coupling", Physical Review B **85**, 081107 (2012).

[72] T. Yanagisawa, "Kondo effect in the presence of spin-orbit coupling", Journal of the Physical Society of Japan **81**, 094713 (2012).

[73] T. A. Costi, "Kondo effect in a magnetic field and the magnetoresistivity of Kondo alloys", Physical Review Letters **85**(7), 1504 (2000).

[74] J. Malecki, "The two dimensional Kondo model with Rashba spin-orbit coupling", Journal of Statistical Physics **129**, 741 (2007).

[75] M. Zarea, S. E. Ulloa, and N. Sandler, "Enhancement of the Kondo effect through Rashba spin-orbit interactions", Physical Review Letters **108**, 046601 (2012).

[76] D. J. Griffiths, *Introduction to Quantum Mechanics*, (Prentice Hall, 2004), 2nd edition.

[77] A. C. A. Pinto, "Comment on the adiabatic condition", American Journal of Physics **68**, 955 (2000).

[78] J. J. Sakurai and J. Napolitano, *Modern Quantum Mechanics*, (Addison-Wesley, 2011), 2nd edition.

[79] G. D. Mahan, *Many-Particle Physics*, Physics of Solids and Liquids, (Kluwer Academic / Plenum Publishers, New York, 2000), 3rd edition.

[80] W. E. Parry, *The Many-Body Problem*, (Oxford Univeristy Press, 1973).

[81] C. Kittel, *Quantum Theory of Solids*, (John Wiley & Sons, 1963).